

RWTH AACHEN UNIVERSITY

# Interaction of Magnetic Skyrmions with Transition Metal Clusters

by  
I Gede Arjana

A thesis submitted in partial fulfillment for the  
degree of Master of science

in the  
Faculty of Mathematics and Natural Science  
Department of Physics

Prepared at :  
Forschungszentrum Jülich GmbH  
Peter Grünberg Institute 1

Supervised by :  
Prof. Dr. Samir Lounis  
Dr. Jonathan Chico  
Dr. Imara Lima Fernandes

December 31<sup>st</sup> 2018  
Germany

# Abstract

Magnetic skyrmions are non-collinear spin textures that are promise candidates as information carriers in future spintronic devices due to their topological protection and high mobility under small electric currents via spin-transfer torque. However, incorporating them as possible bits of information hinges on their interaction with defects since the static and dynamical properties are strongly affected. In this thesis, we investigate single magnetic skyrmion interacting with  $3d$  metal clusters and explore their magnetic and electronic properties using first-principles calculation. The latter is used in conjunction with atomistic spin dynamics to study the impact of the geometry, dimensionality and the chemical nature of the defects on the energy landscape. Depending on the location of the atoms with respect to each other as well as the type of stacking site, such defects can repel or attract single magnetic skyrmions in a PdFe bilayer deposited on Ir(111) surface. Among the studied systems, interestingly for the Cr dimer composing by nearest neighbors atoms shows an attractive behaviour, however, by separating them to a next nearest neighbors location the potential becomes repulsive, such effect can be relate to the competition of the exchange interaction among the atoms in the system. Thus, this study may give guidance of how such defects can be used to engineer tracks and nucleations areas, which are of importance for spintronic devices.

# Declaration of Authorship

I hereby declare that I am the sole author of this master thesis and that I have not used any sources other than those listed in the bibliography and identified as references. I further declare that I have not submitted this thesis at any other institution in order to obtain a degree.

---

Signature

---

Date

# Acknowledgements

First of all, I would like to thank my supervisor Prof. Dr. Samir Lounis who has given me a great opportunity for doing my Master's Thesis project in his group. I am so grateful for his endless support and constant inspiration throughout the preparation of this Master's Thesis.

I am also deeply thankful to Dr. Jonathan Chico and Dr. Imara Lima Fernades for their willingness to devote time on helping me from the very beginning to prepare this thesis. Thank you very much for your guidance and patience, and for always having time to answering any questions that I have. I do appreciate all the valuable advices and the knowledge that has been shared with me.

I am grateful to Prof. Dr. Stefan Blügel for his willingness to examine this thesis, and for giving me an opportunity to do my Master's Thesis in the Institute for Advanced Simulation: Quantum Theory of Materials (IAS-1).

Thank you also funsilabers for having me as a member in the funsilab group and all the people in the IAS-1. Special thanks to Ute who always help me with the administration procedures and issues.

I thank also LPDP for the funding support of my study in Germany.

I also would like to thank my mentor pak Windu Kesiman that always being there whenever I have something to discuss. To Prof. Dr. Wayan Suastra, Prof. Dr. Ketut Suma, and Prof. Dr. Wayan Santyasa for their untiring supports. To my best friend Titan, Mbok Iin, Iyan, Beny, Ivan, Sintya, Yogi, Boi for the help and unlimited support that they provide to me. To all member of second generations for the jokes that they always share with me. To Uda ardhy, edi, vinky, eka for always being there to listen all my complaints and problems that I have. To Pak Subawa and Bu warjani that has always been cheering me up.

Last but not least, I would like to thank my parents, my brothers Beli Putu, and Ocu, and my sisters mbok dek, mbok tut, and adek nik, as well as my cute nieces and nephews for always sending a prayer to me here and always supporting me during the hard times that I have experienced. Special thanks also to all people that have been always giving me a support during my study in Germany.

# Contents

<b>1</b>	<b>Introduction</b>	<b>1</b>
<b>2</b>	<b>A brief introduction to Skyrmions</b>	<b>4</b>
2.1	Introduction to magnetic skyrmions . . . . .	4
2.2	Formation and stability of skyrmions . . . . .	6
2.3	Skyrmions dynamics . . . . .	7
<b>3</b>	<b>The first principles based method</b>	<b>9</b>
3.1	Introduction . . . . .	9
3.2	Green functions . . . . .	12
3.2.1	Green functions in physics . . . . .	12
3.2.2	Dyson equation . . . . .	13
3.2.3	Lippmann-Schwinger equation . . . . .	14
3.3	KKR-Green function formalism . . . . .	15
3.3.1	Single-site scattering . . . . .	15
3.3.2	Multiple scattering theory . . . . .	18
3.3.3	Impurity calculations . . . . .	21
3.4	Self-consistency algorithm . . . . .	23
<b>4</b>	<b>Parametrization of the magnetic Hamiltonian</b>	<b>25</b>
4.1	Calculation of the exchange interaction parameters . . . . .	26
4.2	Calculation of Dzyaloshinskii-Moriya vectors . . . . .	29
4.3	Parametrization with induced magnetic atoms . . . . .	32
<b>5</b>	<b>Magnetization Dynamics</b>	<b>36</b>
5.1	Landau-Lifshitz-Gilbert equation . . . . .	36
5.2	Atomistic spin dynamics . . . . .	38
<b>6</b>	<b>Results</b>	<b>41</b>
6.1	Overview of the System . . . . .	41
6.2	Results and discussion . . . . .	42
6.2.1	Adatom . . . . .	43
6.2.2	Dimer . . . . .	49
6.2.3	Trimer . . . . .	59
6.2.4	Line cluster . . . . .	73
<b>7</b>	<b>Conclusions</b>	<b>77</b>

<b>A</b>	<b>Appendix</b>	<b>79</b>
A.1	LLG Equation . . . . .	79
A.2	t-matrix . . . . .	80
A.3	Exchange interaction parameters . . . . .	81

# List of Figures

1.1	Interaction between magnetic skyrmions in Pd/Fe on Ir(111) and magnetic clusters adsorbed on the surface . . . . .	3
2.1	Illustrations of two different skyrmion configurations . . . . .	5
2.2	Several different configuration of skyrmion structures according to their topological charge $m$ and helicity $\gamma$ . . . . .	5
3.1	Illustration of scatterer's potential in multiple scattering case . . . . .	19
3.2	Schematic representation of the impurity-embedding technique . . . . .	22
3.3	The diagram of self-consistency cycle used in the KKR method . . . . .	24
4.1	Schematic representation of the Dzyaloshinskii–Moriya interaction in multilayer stacks with broken inversion symmetry . . . . .	29
4.2	Moriya's rule to determine the direction of DM vectors . . . . .	30
5.1	Illustration of magnetization dynamics in LLG equation . . . . .	38
6.1	Schematic representation of the FCC and HCP stacking configuration for the system of Pd/Fe/Ir(111) . . . . .	42
6.2	Schematic representation of the adatom cluster . . . . .	43
6.3	Comparison of the local density of states (LDOS) of $3d$ single impurity adatoms . . . . .	44
6.4	The exchange interaction between the adatom (green square) with the Fe atoms in the substrate . . . . .	45
6.5	Variation on the Fe-Fe exchange interaction for adatom case . . . . .	46
6.6	Energy profile of skyrmion interacting with adatom . . . . .	47
6.7	Skyrmion profile for the interaction with adatom . . . . .	48
6.8	Variation of dimer cluster configuration based on the spatial distance between the impurities . . . . .	50
6.9	Energy profile of skyrmion interacting with Co dimer . . . . .	51
6.10	The variation of the Fe-Fe exchange interaction due to the presence of Co dimer . . . . .	52
6.11	The energy profile of skyrmion interacting with Fe dimer . . . . .	53
6.12	The variation of the Fe-Fe exchange interaction due to the presence of Fe dimer . . . . .	54
6.13	The energy profile of skyrmion interacting with Cr dimer . . . . .	55
6.14	The skyrmion profile for the interaction with Cr dimer-1. . . . .	57
6.15	The energy and skyrmion profile for the interaction with mixed Co-Cr dimer . . . . .	58
6.16	The schematic representation of the trimer cluster . . . . .	59

6.17	The comparison of total DOS of Co impurity in the adatom, dimer, and trimer configuration in the FCC and HCP stacking . . . . .	60
6.18	The energy profile for the interaction with defects in compact trimer-1 configuration . . . . .	61
6.19	The skyrmion profile for the interaction with defects in compact trimer-1 configuration . . . . .	62
6.20	The energy profile of skyrmion interacting with impurities in compact trimer-2 configuration . . . . .	65
6.21	The skyrmion profile for the interaction with defects in compact trimer-2 configuration . . . . .	66
6.22	The energy profile of skyrmion interacting with impurities in corner trimer configuration . . . . .	69
6.23	The skyrmion profile for the interaction with defects in corner trimer configuration . . . . .	70
6.24	The energy profile of skyrmion interacting with impurities in linear trimer configuration . . . . .	72
6.25	The skyrmion profile for the interaction with linear defects trimer . . . . .	74
6.26	Schematic representation for the line cluster configuration in FCC and HCp stacking . . . . .	75
6.27	The energy profile of skyrmion interacting with impurities in line configuration . . . . .	76

# List of Tables

6.1	Heisenberg parameters for the adatoms . . . . .	46
6.2	The Heisenberg parameters for the interaction with impurity dimer .	51
6.3	The Heisenberg parameters for the interaction with impurity in compact trimer-1 configuration . . . . .	61
6.4	The Heisenberg parameters for the interaction with impurity in compact trimer-2 configuration . . . . .	64
6.5	The Heisenberg parameters for the interaction with impurity in corner trimer configuration . . . . .	68
6.6	The Heisenberg parameters for the interaction with impurity in line trimer configuration . . . . .	73

# Chapter 1

## Introduction

Over many years information technology has increasingly become an indispensable part of human lives. The advances in this area have made the process of transferring and storing data much more efficient than was previously possible. However, this rapid advancement requires better and more efficient technologies. In order to develop more efficient devices, a large effort has been made to find new alternatives beyond conventional electronic appliances. One of the most investigated approaches is the area of *spintronics*, namely methods which use both the spin and charge of the electron to encode information.

The research on spintronics was spearheaded by the discovery of the Giant Magneto-Resistance (GMR) effect by Albert Fert [4], and Peter Grünberg [8] in the late 1980's, who were awarded the Nobel Prize in 2007. As previously mentioned, in comparison with electronics, spintronics has one key advantage, namely the capacity to use both the spin and charge of the electron to manipulate information. This is due to the fact that using the spin allows for devices with lower energy requirements [52]. Apart from having the reduced energy consumption, the capacity to use the spin of the electron also allows the improvement of both the speed of information transfer and storage capacity [98].

A device that encapsulates some of the efforts in the field of spintronics for higher energy efficiency and storage capacity is the hard disk drive (HDD). To overcome limitations present in previous incarnations such as low speed and durability in writing and storing data information, a new scheme has been proposed to replace the current HDD's [80], and these are the so-called racetrack memory (RM) devices. The basic working concept of such device is to move the magnetic configuration encoding the data instead of moving the device itself which could greatly help to reduce the energy consumption of HDD devices, as no movable parts would be needed. The first proof of concept of a racetrack memory device was proposed by Parkin [80], where he suggested that one could store information in magnetic domains (e.g., a domain "up/down" translates to a 1/0) which were then moved via spin polarized currents interacting with the magnetic domain walls (DWs) separating them. The phenomenon of spin-momentum transfer creates a torque over the moments in the domain wall, which can result in its motion [7]. However, despite its simplicity until now no functional racetrack device based on domain walls is commercially available. This is because the currents needed to operate these devices are large due to pinning, i.e., interaction of the domain wall with defects present in the material [37].

In reality, impurities can be found in nanowires or any other magnetic materials

and significantly affect the DW motion. As shown in several studies, the pinning interaction between domain walls and impurities [34, 1, 64] results in the need of large current densities to drive and dislodge these magnetic textures. Thus, to solve this problem, it has been proposed to use other non-trivial magnetic textures such as magnetic skyrmions in racetrack applications.

Skyrmions as particle-like topologically protected magnetic configurations [91] are very robust against fluctuations [77]. They can be stabilized due to the competition between the Heisenberg exchange and Dzyaloshinskii-Moriya interactions [75, 26]. This characteristic of magnetic skyrmions, make them promising candidates as information carriers in racetrack memory. In skyrmions based racetracks, the information is encoded in the magnetic textures themselves. In other words, the presence or absence of the skyrmion represents the bit 1 or 0, respectively [37]. It is in contrast with domain wall based racetracks, where the information is stored in the magnetic domains.

Compared to domain walls, skyrmions possess quite a few benefits. First, to manipulate skyrmions with spin polarized currents one requires lower current thresholds [101]. Additionally, it has been proposed that skyrmions are less affected by defects [48] due to their particle-like nature. The significant advantages of skyrmions over domain walls in racetrack memory applications, especially concerning the ability to avoid defects, make them propitious for possible applications. However, the skyrmion-defect interaction in real materials must still be addressed in a detailed manner before the skyrmion racetrack memory can be translated into a real competitive technology.

The skyrmion-defect interaction has already been the subject of some investigations from the theoretical standpoint [20, 22, 67]. From the experimental standpoint, a study by Hanneken et al. [32] investigated the interaction of skyrmions in Pd/Fe/Ir(111) with atomic-scale defects. In this work, it was found that skyrmions nucleated in Pd/Fe/Ir(111) interact with a Co trimer deposited on the surface but surprisingly not with a single Co adatom (see Figure 1.1). These different interactions showcase how the skyrmion-defect interaction depends not only on the chemical type of the impurities but also on their shapes and geometries. Atomic defects in Pd/Fe/Ir(111) have also been studied from first principles by Fernandes et al. [67] where the effect of single atomic 3d and 4d transition metal defects located either on top of (adatoms) or embedded in (inatoms) the Pd surface layer was investigated. The result of this study showed that depending on the chemical nature of the impurity, the energy profile of the skyrmion-defect interaction could change considerably. The attractive or repulsive behaviour was found to be dependent on the chemical nature of the defect and it is related to the degree of filling of bonding and anti-bonding electronic states.

Generally defects are seen as inhibitors for applications, however, by manipulating defects with either attractive or repulsive behaviour, it is possible to propose a new racetrack architecture incorporating them into its design. In this thesis, the interaction between a magnetic skyrmion and a variety of defects will be studied, via a combination of first principles methods and atomistic spin dynamics. The considered defects consist of 3d transition metal elements with varied shapes and dimensionality. The investigation will discuss how the different types and configurations of impurities such as a dimer, trimer, and line, can affect both the stability and dynamics of skyrmions. The system of interest that will be investigated is a PdFe

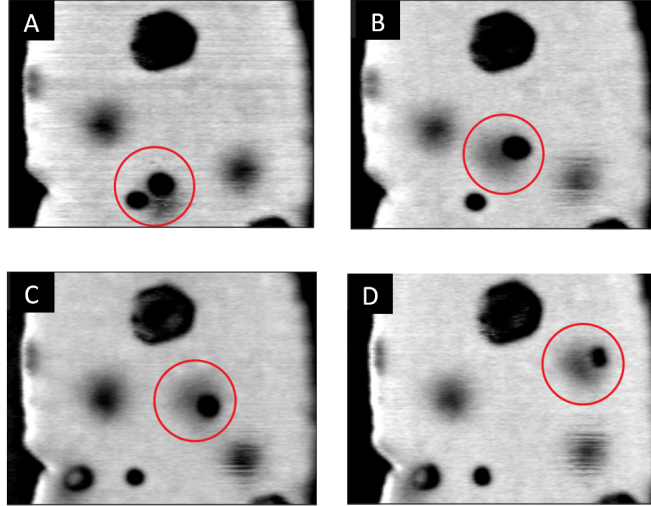


Figure 1.1: Interaction between magnetic skyrmions in Pd/Fe on Ir(111) and magnetic clusters adsorbed on the surface. The black shadow is the skyrmion whereas the black circle denotes the Co-trimer. The skyrmion interacting with cluster (Co-trimer) is shown by the red circle. (A)-(D) show a series of subsequent dI/dU maps in which the cluster is manipulated over the surface with an STM tip with the skyrmion being moved by it. (Figure adapted from Ref.[32])

bilayer deposited on Ir(111) substrate (Pd/Fe/Ir (111)). First principles methods will be used to obtain the electronic and magnetic properties of the system, such as the pairwise Heisenberg exchange interaction, the Dzyaloshinskii-Moriya (DM) interaction, and the magnetocrystalline anisotropy. These parameters will be then employed in atomistic spin dynamics simulations to investigate the skyrmions dynamics under the influence of defects.

This thesis is organized as follows: in Chapter 2 a brief introduction about magnetic skyrmions will be given. The discussion will cover some fundamental aspects of magnetic skyrmions, namely what they are and their key properties. In Chapter 3 the Green function based on first principles Korringa-Kohn-Rostocker (KKR) method will be introduced. In particular, the fundamentals of Green functions, multiple scattering formalism and the treatment of impurities via the Dyson equation will be discussed in details. The parametrization of the magnetic Hamiltonian from first principles will be presented in Chapter 4, focusing on the determination of Heisenberg exchange interactions and the Dzyaloshinskii-Moriya vectors, key parameters for the description of magnetic skyrmions. The discussion of atomistic spin dynamics will be given in Chapter 5. This part will explain in details the Landau-Lifshitz-Gilbert (LLG) equation as well as its extension to include the spin-transfer torque, the mechanism behind the skyrmions motion. Results and discussion of the investigated system for this thesis will be presented in Chapter 6. Lastly, in Chapter 7 some conclusions and outlook for this thesis will be presented.

# Chapter 2

## A brief introduction to Skyrmions

Magnetic skyrmions have been the subject of intense experimental and theoretical researches over the last decade as their topological properties make them ideal candidates for several spintronic devices [19, 80]. In this chapter a small introduction to the field of skyrmionic will be made, going from the basic description of the skyrmionic textures to the depiction of the properties that make them such scrutinized objects.

### 2.1 Introduction to magnetic skyrmions

The concept of a skyrmion was originally introduced by Tony Skyrme (1961) as a theoretical model to explain the stability of quasi-particles in field theory [91]. This model has been used in several fields of physics with many different applications such as in nuclear physics [91, 56], quantum Hall systems [94], and liquid crystals [12]. In magnetism, the skyrmions are described as topologically protected, particle-like spin textures. In most cases, their existences are induced by chiral interactions between atomic spins [39]. The magnetic configuration of skyrmions can be seen in Fig. 2.1a which presents the Néels-type skyrmion with the magnetization rotating in a radial plane from the down direction at its centre to the up direction at the boundary. There is also another type shown in Fig. 2.1b which is called as Bloch-type skyrmion where the spins rotate in the tangential plane, i.e., perpendicular to the radial direction when moving from the core to the periphery of the skyrmions [61].

As one can see from Fig.2.1, the skyrmion configuration is topologically unique. If one projects its spin texture in an unit sphere, the magnetization will wrap the whole surface and pointing in all possible directions. This topological nature of skyrmions is characterized by the topological charge (skyrmion number) [18]

$$m = \frac{1}{4\pi} \int (\hat{n} \cdot [\partial_x \hat{n} \times \partial_y \hat{n}]) dx dy, \quad (2.1.1)$$

which describes how many times that a spin vector with direction,  $\hat{n}$ , wraps the entire sphere. Based on the topological point of view, two structures are considered equivalent if a continuous map exists from one to another without passing an infinitely large energy barrier [33, 18]. For a single magnetic skyrmion, it has an integer topological charge. A physical manifestation of such topological quantization is that the skyrmion configurations are topologically protected from a continuous

deformation into the ferromagnetic state or other spin configurations with different topological nature. This protection is associated with an energy barrier considered as infinite from the point of view of topological classification [18].

The topological charge can also be used to classify the different types of magnetic excitations. The number of  $+1$  is used to describe skyrmions and  $-1$  is for anti-skyrmions which have an opposite chirality [77]. Apart from these two categories, there are some other classifications where the structure also depends on the helicity,  $\gamma$ , namely the direction of the Dzyaloshinskii-Moriya (DM) interaction which is determined by the symmetries of the crystal structure. In Fig. 2.2 several configurations of skyrmions with different topological charge and helicity are presented. The black colour in the figure means the spins are pointing either up or down with a zero in-plane component, whilst the arrows indicate the direction of the spins, and their colours represent the normal component to the plane. The top and bottom panels in Fig. 2.2 are separated based on the topological charge,  $\pm 1$ , with some subcategories according to several values of helicity.

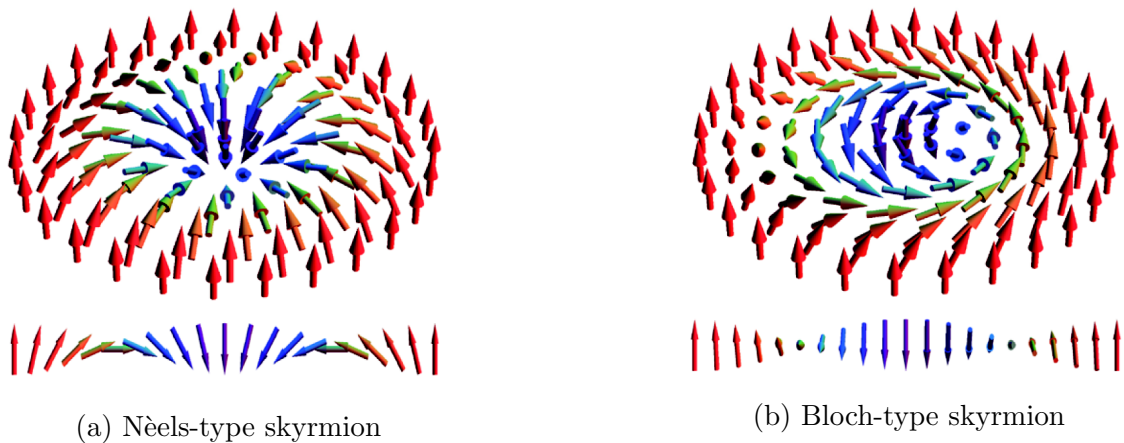


Figure 2.1: Illustrations of two different skyrmion configurations (a) Néel-type skyrmion (b) Bloch-type skyrmion. This picture is taken from [53]

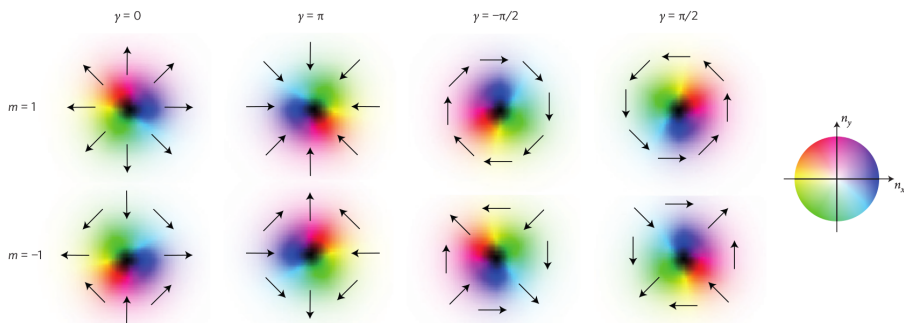


Figure 2.2: Several different configuration of skyrmion structures according to their topological charge  $m$  and helicity  $\gamma$ . The arrows indicate the direction of the spins, and their colours represent the normal component to the plane, that is, from up direction (red) to the down direction (blue). This picture is taken from Ref.[77]

The existence of magnetic skyrmions was studied theoretically by Bogdanov et al. [13] in ferromagnetic materials lacking inversion symmetry. This was then verified

by the first experimental study which observed the skyrmion lattice as a new type of magnetic order in the manganese silicide (MnSi) in 2009 [76]. This material is very well-known as chiral magnetic where below the critical Curie temperature at small (or zero) magnetic field, the magnetization in this material is in a helical state. By increasing the magnetic field, it then changes into the canonical state. Beside these two states, there was also an interesting feature in the phase diagram, namely the so-called A-phase which later was identified as skyrmion phase. After the first discovery of skyrmion in MnSi, skyrmion lattices were also found in many other crystals without inversion symmetry and with the strong spin-orbit coupling [100, 88].

The broken inversion symmetry in magnetic systems with spin orbit coupling generate the Dzyaloshinskii-Moriya (DM) interactions which are responsible for the chiral structure of skyrmions [26, 75]. In most cases, these chiral DM interactions competing with exchange interactions play an important role in determining the existence of skyrmions in a magnetic material. However, there are also several mechanisms with different interactions which can allow the creation of skyrmion. In the following section, a discussion about these mechanisms will be presented.

## 2.2 Formation and stability of skyrmions

The formation of a skyrmion in a magnetic system can take place due to several mechanisms in different systems [77]. Some of them that have been studied both experimentally and theoretically are the following: a) competition between magnetic dipole interaction and easy-axis anisotropy, b) competition between Dzyaloshinskii-Moriya (DM) interactions and Heisenberg exchange interactions, and c) four-spin exchange interactions. The type and strength of interactions in each procedure generate skyrmions with different size and characteristics. In this thesis, the formation of skyrmions in chiral magnets due to the DM interaction will be the focus of interest.

The first mechanism of the skyrmions creation is due to a competition between a long-ranged magnetic dipole interaction and a perpendicular easy-axis anisotropy in thin-layer magnetic systems [68, 41]. In the system, the anisotropy favours an out-of-plane magnetisation, whereas the long-range magnetic dipole interaction favours an in-plane direction. Their competitions result in a periodic stripe with spins rotating in the plane perpendicular to the thin film. An application of a magnetic field normal to the film turns the stripe into a periodic arrangement of magnetic bubbles or skyrmions which are of typically 100 nm to 1  $\mu\text{m}$  sizes [87].

The second procedure of the skyrmion formation is taking place due to the Dzyaloshinski-Moriya interaction emerging from the systems with broken inversion symmetry and strong spin-orbit (SOC). The broken inversion symmetry usually can be found in helical magnets materials such as B20 compounds including MnSi, FeGe, and  $\text{Fe}_x\text{Co}_{1-x}\text{Si}$  [84]. The presence of the DM interactions ( $D_{ij}$ ) competing with the Heisenberg exchange interactions ( $J_{ij}$ ) is responsible for the formation and stabilization of skyrmions[14, 47]. The exchange interactions favor a collinear ferromagnetic spin alignment, and on the other hand, the DM interactions favor a rotation of magnetization alignment with the turn angle of  $90^\circ$ . In the absence of an external magnetic field, this competition results in a helical spin-spiral state as the ground state of the system. However, when a suitable strength of magnetic field is applied into the spin-spiral state, it will turn into a skyrmion phase where the magnetic

moments of the skyrmion perimeter have direction parallel to the applied external magnetic field and the ones at the center are antiparallel to the field direction. The size of this skyrmion is determined by the ratio of the Dzyaloshinskii–Moriya interaction  $D_{ij}$ , to the exchange interaction  $J_{ij}$ , and in chiral-lattice ferromagnets, it is around 3–100 nm.

In the other mechanisms, a two dimensional square lattice of skyrmions on a hexagonal monolayer Fe on Ir(111) was also found due to a square symmetry of the system in combination with the Heisenberg exchange and DM interaction [44]. The short-range four-spin-interaction imposes a square symmetry on the configuration, whilst the DM interaction cut down the energy further by the formation of skyrmions with a unique rotational sense.

A stabilization of skyrmions in magnetic materials is great of importance for their application in future technology. Apart from this aspect, another elementary functionality which is needed to consider is their dynamics. To utilize skyrmions in practical electronics applications, for instance in racetrack memory devices as the information carriers [80], their motion will be a significant point in the process of transferring data information.

## 2.3 Skyrmions dynamics

One of the main reasons that make skyrmions very prospective in the applications of spintronics devices is due to the possibility to move and control them via an electrical current. It was found that the skyrmions can be driven by applying a spin polarized current via the spin transfer torque (STT) effect [92]. However, during their motions, the skyrmions do not move collinear to the current flow direction but acquire a transverse motion due to the appearance of a topological Magnus force [49]. This phenomenon is referred to skyrmion Hall effect [36, 95].

The deflection in the skyrmions motion can be a serious problem for the implementation of skyrmion-based nanotrack devices because it will lead to the annihilation of skyrmions at the edge of the track [104]. To overcome this issue Zhang, et al. [106] propose a sandwich structure composed of two skyrmions materials coupled antiferromagnetically and separated by a non-magnetic one, which can cancel out the Magnus forces in the magnetic layer and leads the skyrmions to move parallel to the applied currents.

Despite the skyrmion Hall effect phenomenon, skyrmions dynamics has some interesting properties that make them advantageous over the other magnetic textures. First, concerning the threshold current density to have the skyrmions mobile in the magnetic material. It has been shown that it needs a current density of  $10^6 \text{A/m}^2$  to move them in helimagnets, which is much lower than the required magnitude for magnetic domain walls [51]. This low current density is predicted to be able to reduce the Joule heating effect that happens due to the excessive use of electric currents.

Another interesting aspect of skyrmions motion is the way they interact with impurities presented in the medium. In several studies based on the phenomenological models, it has been shown that skyrmions have the flexibility to move around defects due to their particle-like behaviours [83, 37, 48]. According to work done by Fert et al. [37], a single skyrmion change its trajectory to go around an impurity which is presented by a magnetic region with a large anisotropy. The same behaviour was

also found in skyrmions lattice motion where there are point-like defects with large magnetocrystalline anisotropy, distributed randomly in lattice [48]. Due to their particle-like nature, each individual skyrmion can change its own path flexibly in such a manner as to avoid pinning centres and thus result in the deformation of the skyrmion lattice.

The defect avoidance ability owned by the skyrmions become an essential part to their implementations in the spintronics applications such as in a racetrack memory [80]. This peculiar behaviour might be the solution to the problem caused by impurities that was found in the domain wall based racetrack. Therefore, a deeper understanding of skyrmion-defects interaction is extremely needed.

A further discussion of skyrmions interacting with defects will be presented in this thesis. Unlike the previously mentioned studies where the analysis was done in a micromagnetic regime, i.e., use a large size of skyrmion and describe the defects as regions with large magnetic anisotropy, this thesis will discuss the interaction of a small skyrmion with realistic defects in atomic scale. The investigated defects are 3d metal transitions elements with varied type of geometries and dimensionalities such as single adatom, dimer, trimer, and line defects. Using these variations, the stability and dynamics of skyrmions will be studied through atomistic spin dynamics (ASD) with the parameters obtained from the first principles calculations. The following chapter starts the discussion by describing the concept of Korringa-Kohn-Rostoker (KKR) Green function method to calculate the parameters that will be employed in spin dynamics simulation. A detail explanation of physical concepts behind this method will be presented and along with the discussion of mathematical approaches that are used to perform the parameters calculation.

# Chapter 3

## The first principles based method

### 3.1 Introduction

In order to study the properties of materials, such as conductivity, or the interaction between magnetic textures and defects present on them, one inevitably must understand the electronic structure of such materials. The understanding of the electronic structure of a system can be achieved by looking at the time independent many body Schrödinger equation:

$$\mathcal{H} |\Psi(\mathbf{r}_1, \mathbf{r}_2, \dots, \mathbf{r}_N; \mathbf{R}_1, \mathbf{R}_2, \dots, \mathbf{R}_M)\rangle = E |\Psi(\mathbf{r}_1, \mathbf{r}_2, \dots, \mathbf{r}_N; \mathbf{R}_1, \mathbf{R}_2, \dots, \mathbf{R}_M)\rangle, \quad (3.1.1)$$

where  $|\Psi(\mathbf{r}_1, \mathbf{r}_2, \dots, \mathbf{r}_N; \mathbf{R}_1, \mathbf{R}_2, \dots, \mathbf{R}_M)\rangle$  is the many body electronic and ionic wavefunctions with an energy  $E$ , the  $\mathbf{r}_i$ 's indicate the electronic coordinates, while the  $\mathbf{R}_j$ 's indicate the ionic positions. The interaction between them is encoded in the Hamiltonian:

$$\mathcal{H}_{\text{tot}} = - \sum_i^M \frac{\nabla_{\mathbf{R}_i}^2}{M_i} - \sum_i^N \nabla_{\mathbf{r}_i} + \sum_{i \neq j} \frac{Z_i Z_j}{|\mathbf{R}_i - \mathbf{R}_j|} + \sum_{i \neq j} \frac{1}{|r_i - r_j|} - \sum_{i,j} \frac{2Z_i}{|r_i - R_j|}, \quad (3.1.2)$$

with  $M_i$  being the mass of the ions,  $Z_i$  being their atomic charge,  $\nabla_{\mathbf{R}_i}$  and  $\nabla_{\mathbf{r}_i}$  represent the real space momentum operator for the ions and the electrons, respectively. As can be seen, to obtain a direct solution of this many-body Schrödinger equation in real solids is impossible, as the number of the interacting particles is extremely large. Thus, some approximations are required to simplify the problem. One of the most used is the Born-Oppenheimer approximation, in which the ionic degrees of freedom are considered to be frozen with respect to the electronic system. This is possible because of the large mass difference between the ions and the electrons, with the ions being much more massive, and therefore slower than the electrons, thus they can be considered to be always at rest with respect to them later.

Such approximation allows to eliminate the ionic degrees of freedom from the many-body wavefunctions,  $|\Psi(\mathbf{r}_1, \mathbf{r}_2, \dots, \mathbf{r}_N; \mathbf{R}_1, \mathbf{R}_2, \dots, \mathbf{R}_N)\rangle \rightarrow |\Psi(\mathbf{r}_1, \mathbf{r}_2, \dots, \mathbf{r}_N)\rangle$ , as well as resulting in a simplification of the Hamiltonian, as one can now write the effect of the ions as an external potential,  $V_{\text{ext}}$ , resulting in a Hamiltonian describing the electrons:

$$\mathcal{H} = \sum_i [-\nabla_{\vec{r}_i}^2 + V_{\text{ext}}(\vec{r}_i)] + \sum_{i \neq j} \frac{1}{|\vec{r}_i - \vec{r}_j|}. \quad (3.1.3)$$

This approximation has significantly reduced the complexity of the problem, however, for a real material the problem is still impossible to be solved analytically, thus another approach is needed to determine the electronic properties of the system.

In 1964 Hohenberg and Kohn [45] proposed a different approach known as Density Functional Theory (DFT) to deal with this many-body problem. The basic principle behind this approach is to obtain all the ground state properties of a system by using the electronic density,  $n(\mathbf{r})$ , instead of the many-body wavefunctions. According to the Hohenberg-Kohn theorems, for a system of interacting particles in an external potential,  $V_{\text{ext}}(\mathbf{r})$ , the density is uniquely defined, and that the energy of the system can be written as a functional of the density,  $E[n(\mathbf{r})]$ , that when minimized is equal to the ground state energy of the system.

These theorems pave a way to solve the many-body interacting problem, as now it is not necessary to know the full many-body wavefunctions, all that one needs to determine is the electronic density to fully characterize the ground properties of the system. However, the determination of the interacting density is still, in many cases, and intractable problem.

An approach to circumvent such difficulties was proposed by Kohn and Sham [57]. In this method, instead of trying to solve the full-interacting many-body problem, an auxiliary **non-interacting single particle** system with the same density than the real one is proposed. Thanks to the Hohenberg-Kohn theorems, it is known that if the density of these two systems are identical, then they will have the same groundstate energy. The properties of the auxiliary system are determined by the Kohn-Sham equations:

$$[-\nabla^2 + V_{\text{eff}}(\vec{r})] \varphi_i(\vec{r}) = \epsilon_i \varphi_i(\vec{r}), \quad (3.1.4)$$

where  $\epsilon_i$  and  $\varphi_i$  are the Kohn-Sham eigenvalues and eigenfunctions, respectively. The effective potential  $V_{\text{eff}}(\vec{r})$  is expressed as:

$$V_{\text{eff}}(\vec{r}) = V_{\text{ext}}(\vec{r}) + 2 \int d^3\vec{r}' \frac{n(\vec{r}')}{|\vec{r} - \vec{r}'|} + V_{\text{xc}}(\vec{r}), \quad (3.1.5)$$

with  $V_{\text{ext}}(\vec{r})$  being the potential generated by the nuclei, the second term is the Coulomb electron-electron interaction, and  $V_{\text{xc}}(\vec{r})$  represents the **exchange-correlation potential** which includes all the many-body effects. The electronic density  $n(\vec{r})$  is then calculated by:

$$n(\vec{r}) = \sum_i |\varphi_i(\vec{r})|^2. \quad (3.1.6)$$

It is important to note that in principle DFT is an exact theory, however, there is a problem when going to a practical implementation, namely the exchange correlation potential. Until now the  $V_{\text{xc}}(\vec{r})$  in Eq. 3.1.5 is still an unknown quantity, therefore approximations are needed to describe this term. One of the most common approximations used for the exchange-correlation potential is the local density approximation (LDA) [59]. It assumes that the exchange correlation energy per electron,  $E_{\text{xc}}(\vec{r})$ , of a homogeneous electron gas depends only on the charge density

$n(\vec{r})$  at each point in space. Surprisingly, this approximation does not only work for systems with a uniform density but also for cases where the electron density is inhomogeneous [43, 50]. An extension of LDA was introduced by von Barth and Hedin [97] in which they include spin polarized densities to be able to describe magnetic systems. This approach is known as the local spin density approximation (LSDA), since the exchange correlation potential is not only dependent on the electronic density, if not also on the magnetization density. Thus, a spin dependent exchange-correlation potential is introduced in the Kohn-Sham equation by replacing the electron density  $n(\vec{r})$  with the generalized density matrix  $\rho(\vec{r})$ :

$$n(\vec{r}) \rightarrow \rho(\vec{r}) = \frac{n(\vec{r})}{2} \mathbb{1} + \frac{m(\vec{r})}{2} \vec{\sigma}, \quad (3.1.7)$$

where  $\mathbb{1}$  is the 2 x 2 unit matrix,  $m(\vec{r})$  is the magnetization density and  $\vec{\sigma}$  are the Pauli matrices. Hence, one must now recast the Kohn-Sham equations as functionals of the electronic and the magnetization density, which implies that the energy functional must now be minimized with respect to these two quantities. One can then express the spin-dependent Kohn-Sham Hamiltonian as follows:

$$\mathcal{H} = \left[ -\nabla^2 \delta_{\alpha\beta} + V_0^{\alpha\beta}(\vec{r}) + \vec{B}_{\text{eff}}(\vec{r}) \cdot \vec{\sigma} \right], \quad (3.1.8)$$

with  $\alpha$  and  $\beta$  being the spin projections,  $V_0^{\alpha\beta}(\vec{r})$  being the non-magnetic part of the potential, and the  $\vec{B}_{\text{eff}}(\vec{r}) \cdot \vec{\sigma}$  is the magnetic potential.

In practice the Kohn-Sham equations are solved in an iterative fashion, where an initial guess of the potential is given, and then the single particle Schrödinger equation is solved in each iteration cycle, until a certain convergence criteria, usually the change in the charge and spin density, is achieved [107]. As long as the usual band structure calculation algorithms are used, the numerical costs are proportional to the third power of the system size. Hence, for systems with a large number of atoms, an extensive amount of computational resources is needed [23]. To overcome these difficulties new schemes and methods should be developed in order to achieve more efficient calculations.

Over the past decades, several different approaches to solve the Kohn-Sham equations have been proposed, many of them are based on plane waves, which are used as a basis for the Kohn-Sham eigenfunctions [99, 85]. These methods are quite powerful and have allowed researchers to determine the electronic and magnetic properties of many materials, some of which are of key interest for the study of magnetic skyrmions, such as in the case of Pd/Fe/Ir(111) by Dupé et al. [24]. However, for the present investigations, these methods have key weaknesses, such as the need of large supercells to treat impurities, making them not the best option to treat the desired systems. Instead one needs to look at another class of numerical methods, based not on the wavefunction if not instead on a different mathematical object, the Green function. The Green function is a powerful object, as it contains **all** the information that the wavefunctions have, whilst having several advantages, such as its capacity to be easily modified to include perturbations [10].

The concept of Green functions is used in several DFT approaches, in this thesis the method of choice is the so-called Korringa-Kohn-Rostoker (KKR) method. Originally this scheme was proposed by Korringa [60] as a wavefunction based method,

where the single-particle problem is recasted making use of scattering theory. Later, this approach was reformulated by Korringa and Rostoker [58] as a Green function based method. As previously mentioned, Green functions based schemes are very attractive for the study of the interaction between magnetic skyrmions and defects. Thanks to their properties one can completely avoid the use of large super-cells to calculate systems with impurities, greatly reducing the computational effort needed to tackle this kind of problems. Thus, to be able to understand the basics behind the Green function based KKR method, it is of interest to first understand the basic properties of these mathematical objects.

## 3.2 Green functions

### 3.2.1 Green functions in physics

A Green function is a powerful mathematical tool to determine the solutions of a differential equation. This method was originally invented in mathematics to solve non-homogeneous boundary value problems. In physics, especially in solid state, the Green function is usually used as an alternative way to solve the single particle Kohn-Sham equation. It is defined as resolvent of the single-particle Hamiltonian used in the inhomogeneous Schrödinger equation:

$$(\epsilon - \mathcal{H}) G(r, r', E) = \delta(r - r'), \quad (3.2.1)$$

where  $\epsilon = E + i\eta$ , with  $E$  being the energy and  $\eta$ , an infinitesimal positive real number associated with the energy dependent Green function,  $G(r, r', E)$ . It is important to notice that the Green function shown in Eq. 3.2.1 is completely abstract object, however, for practical purposes one can express it making use of a certain basis,  $|\varphi_i\rangle$ , via the spectral representation or Lehmann representation:

$$G^\pm(\vec{r}, \vec{r}', E) = \sum_i \frac{\varphi_i(\vec{r})\varphi_i^*(\vec{r}')}{E - \epsilon_i \pm i\eta}, \quad (3.2.2)$$

where  $+(-)$  sign refers to the retarded(advanced) Green function.

The relation between Green functions and wavefunctions shown in Eq.3.2.2 leads to the capacity to extract the information encoded in the wavefunctions via Green functions. For instance, one can calculate the electronic density,  $n(\vec{r}; E)$ , by connecting it directly to the imaginary part of of retarded Green functions  $G^+(\vec{r}, \vec{r}', E)$ . By applying the Dirac identity

$$\lim_{\eta \rightarrow 0^+} \frac{1}{x + i\eta} = \mathcal{P} \left( \frac{1}{x} \right) - i\pi\delta x, \quad (3.2.3)$$

where  $\mathcal{P}$  is the Cauchy principal part of integral, one can write the expression for electronic density as:

$$n(\vec{r}) = -\frac{1}{\pi} \text{Im} G(r, r; E). \quad (3.2.4)$$

Thus, one can determine the charge density,  $\rho(r)$ , by integrating the electronic density over the energy:

$$\rho(r) = -\frac{1}{\pi} \text{Im} \int_{-\infty}^{E_F} G(r, r; E) dE. \quad (3.2.5)$$

It is important to notice that the Green function is an object in the complex plane, hence, it is possible to integrate over the complex energy  $\epsilon$  using the contour integration technique. This approach has the advantage of reducing the numerical difficulties present in the integration along the real axis [10].

Here, one can also express the density of states within a volume  $\mathcal{V}$  in terms of Green functions as [73]:

$$\begin{aligned} n_{\mathcal{V}}(E) &= \sum_i \delta(E - \epsilon_i) \int_{\mathcal{V}} d\vec{r} |\varphi_i(\vec{r})|^2 \\ &= -\frac{1}{\pi} \text{Im} \int G(\vec{r}, \vec{r}; E) d\vec{r} \\ n_{\mathcal{V}}(E) &= -\frac{1}{\pi} \text{Im} \text{Tr} \tilde{G}(E). \end{aligned} \quad (3.2.6)$$

One can notice that in Eq. 3.2.6 the density of states can be obtained by taking the trace of the imaginary part of the Green function, *irrespective* of the chosen basis. The Green functions provide more information than just the density of states and the charge density. One can obtain the expectation value for any operator  $\tilde{A}$  by calculating:

$$\langle \tilde{A} \rangle = -\frac{1}{\pi} \int \text{Tr} \left[ \tilde{A} G(\vec{r}, \vec{r}; E) \right] f_T(E) dE, \quad (3.2.7)$$

The derivations of the observable quantities presented in this section show the effectiveness of the Green functions in calculating the ground state properties of a system. Even more, Green functions are uniquely suited to treat the effect of impurities in solids, as it will be made apparent in the upcoming sections.

### 3.2.2 Dyson equation

The Green functions method do not only enable us to determine the ground state properties of electronic systems without knowledge of the wavefunctions, but also have a key advantage of dealing with perturbations by making use of the Dyson equation [30]. The latter allows one to relate the Green function of a reference system  $\tilde{G}_0$ , whose Hamiltonian operator is given by  $\tilde{H}_0$ , and the Green function  $\tilde{G}_1$  of a system with a perturbation  $\Delta\tilde{V}$  and Hamiltonian  $\tilde{H} = \tilde{H}_0 + \Delta\tilde{V}$ , which can be defined as:

$$\tilde{G}_0^{-1} = E\tilde{\mathbb{1}} - \tilde{H}_0, \quad \tilde{G}_1^{-1} = E\tilde{\mathbb{1}} - \tilde{H}_0 - \Delta\tilde{V}. \quad (3.2.8)$$

Thus, the Green function  $\tilde{G}_1$  can be expressed as function of  $\tilde{G}_0$ ,

$$\tilde{G}_1^{-1} = \tilde{G}_0^{-1} - \Delta\tilde{V}. \quad (3.2.9)$$

By multiplying each term of Eq. 3.2.9 on the left-hand side by  $\tilde{G}_0$  and on the right-hand side by  $\tilde{G}_1$  leads to

$$\begin{aligned}\tilde{G}_0\tilde{G}_1^{-1}\tilde{G}_1 &= \tilde{G}_0[\tilde{G}_0^{-1} - \Delta\tilde{V}]\tilde{G}_1 \\ \tilde{G}_1 &= \tilde{G}_0 + \tilde{G}_0\Delta\tilde{V}\tilde{G}_1.\end{aligned}\tag{3.2.10}$$

The previous expression is known as **Dyson Equation** and it is of great importance for the systems studied in this thesis as it allows one to relate the Green function of a pristine system with the one with an impurity present. One can expand Eq. 3.2.10 by substituting the left-hand side  $\tilde{G}_1$  into its counterpart at the right-hand side:

$$\begin{aligned}\tilde{G}_1 &= \tilde{G}_0 + \tilde{G}_0\Delta\tilde{V}\tilde{G}_0 + \tilde{G}_0\Delta\tilde{V}\tilde{G}_0\Delta\tilde{V}\tilde{G}_0 + \dots \\ &= \tilde{G}_0 + \tilde{G}_0(\Delta\tilde{V} + \Delta\tilde{V}\tilde{G}_0\Delta\tilde{V} + \dots)\tilde{G}_0.\end{aligned}\tag{3.2.11}$$

### 3.2.3 Lippmann-Schwinger equation

Apart from the Dyson equation, there is also another feature of Green function which is widely used to calculate the electronic structure, namely the Lippmann-Schwinger equation. If one can use the Dyson equation to connect the Green functions of the unperturbed and perturbed systems, here the Lippmann-Schwinger equation can be used to connect the wavefunctions of those two systems. Considering the wavefunctions of an unperturbed system  $|\psi\rangle$  and a perturbed system  $|\phi\rangle$ , which are the solutions of the Hamiltonian  $\mathcal{H}_0$  and  $\mathcal{H}$ , respectively, the Schrödinger equations for both Hamiltonians can be written as:

$$[E - \tilde{H}_0]|\phi\rangle = 0\tag{3.2.12}$$

$$[E - \tilde{H}_0]|\psi\rangle = \Delta\tilde{V}|\psi\rangle.\tag{3.2.13}$$

Then, the eigenfunction of the unperturbed system,  $|\psi\rangle$ , can be expanded in terms of the solution of homogeneous equation,  $|\phi\rangle$ :

$$|\psi\rangle = |\phi\rangle + |\psi_\alpha\rangle,\tag{3.2.14}$$

where  $|\psi_\alpha\rangle$  is a particular inhomogeneous solution of the inhomogeneous differential equation. By employing the Eq. 3.2.12 -Eq. 3.2.14 and the definition of  $\tilde{G}_0(E)$  (see Eq. 3.2.8), the so-called Lippmann-Schwinger equation can be written as:

$$|\psi\rangle = |\phi\rangle + \tilde{G}_0\Delta\tilde{V}|\psi\rangle.\tag{3.2.15}$$

For numerical purposes, one can generalize the Dyson equation and the Lippmann-Schwinger equation in real space representation as [102]:

$$G_1(\vec{r}, \vec{r}', E) = G_0(\vec{r}, \vec{r}', E) + \int d\vec{r}'' G_0(\vec{r}, \vec{r}'', E)V(\vec{r}'')G_1(\vec{r}'', \vec{r}', E)\tag{3.2.16}$$

$$\psi(\vec{r}, E) = \psi_0(\vec{r}, E) + \int d\vec{r}'' G_0(\vec{r}, \vec{r}'', E)V(\vec{r}'')\psi_0(\vec{r}'', E),\tag{3.2.17}$$

where  $\vec{r}$ ,  $\vec{r}'$  and  $\vec{r}''$  define the vector positions in real space.

The features of Green function formalism described in this section are very useful once implemented in the KKR method to study of the electronic structure of materials locally perturbed by defects. By means of a Dyson equation, one can directly connect the Green function of an impurity to the crystal Green function of the host system which makes KKR calculations much more efficient and attractive. In order to see the implementation of these Green function features in the electronic structure calculations with the KKR-GF method, both single-site and multiple-site scattering with Green function formalism are discussed in the following section.

### 3.3 KKR-Green function formalism

The KKR-Green function method is an alternative way to solve the Kohn-Sham equation, which uses multiple scattering theory [60, 58]. In its implementations, each atom in solids is treated as a scatterer. There are two steps involved in this method: first, solving the single scattering problem to obtain the scattering properties of each atom. The second step is to solve the multiple scattering of all atoms by applying the condition that the sum of outgoing and incident waves of each atom (scattering center) are equal [73]. In the multiple scattering method, the scattering events from any of the atoms in the system are represented by scattering matrix elements  $\mathbf{t}$ , and the propagation of scattered particle from one scattering event to another is shown by a Green function  $G$  [31]. For an ensemble of  $N$  scatterers, the total scattering matrix is given by  $\mathbf{T}$  matrix [72].

Unlike other band structure methods that are based on the electronic wave functions and energy eigenvalues calculations for a crystal, the KKR-Green function method is calculating a single particle Green's function. As previously discussed in the Green function section, the charge density and other observable quantities of the system can be extracted from it. Another advantage of Green function methods is the ability to treat systems with impurity elegantly without the need to construct supercells. For these reasons, the KKR is the method of choice in this thesis to study the interaction between skyrmions with the defect atoms. In the following section, the description of the single-site scattering process will be discussed. Then, some formulations of Green function will be presented for free space and for the case with a finite range of potential, which will be useful in the further discussion on multiple sites scattering.

#### 3.3.1 Single-site scattering

In the following, a scattering by a single central potential will be discussed assuming a spherically symmetric scattering center at the origin [5]:

$$V(\vec{r}) = \begin{cases} V(r), & \text{for } r < r_{max} \\ 0, & \text{otherwise.} \end{cases} \quad (3.3.1)$$

First, the free electron problem, i.e.,  $V(\vec{r}) = 0$  will be analyzed to obtain the expansion of the Green function for an electron in free space. This result will be then used to obtain the Green function for single-site scattering with a finite-range potential.

## Potential-free

The Hamiltonian for a free-electron is given by  $\mathcal{H}_0 = -\nabla^2$  and the eigenfunctions are the plane waves  $\psi_{\vec{k}}(r) = e^{i\vec{k}\cdot\vec{r}}$ . The corresponding Green function is given by:

$$G_0(\vec{r}, \vec{r}') = -\frac{1}{4\pi} \frac{e^{ik|\vec{r}-\vec{r}'|}}{|\vec{r}-\vec{r}'|}, \quad (3.3.2)$$

where  $k = \sqrt{E}$ . In spherical harmonics expansion, these wavefunctions and Green functions are given by the following expressions:

$$\psi_k(r) = e^{i\vec{k}\cdot\vec{r}} = \sum_L 4\pi i^\ell j_\ell(kr) Y_L^*(\vec{k}) Y_L(\vec{r}), \quad (3.3.3)$$

$$G_0(\vec{r}, \vec{r}') = \sum_L Y_L(\hat{r}) g_\ell(r, r') Y_L(\hat{r}'), \quad (3.3.4)$$

where  $\hat{r} = \vec{r}/|\vec{r}|$ ,  $L$  represents the combined index for both the angular ( $\ell$ ) and magnetic ( $m$ ) quantum number,  $j_\ell(kr)$  is the spherical Bessel function, and  $Y_L(\vec{r})$  denotes the real spherical harmonics. The term  $g_\ell(r, r')$  is the expansion coefficient given by [5]:

$$g_\ell(r, r') = -ik j_\ell(kr_<) h_\ell(kr_>). \quad (3.3.5)$$

Here  $r < (>)$  denote the smaller (bigger) of the radius of  $r$  and  $r'$ .  $h_\ell = j_\ell - in_\ell$  is the spherical Hankel function with  $n_\ell$  as the spherical Neumann function that is also known as spherical Bessel functions of second kind. The Bessel functions are finite in the limit  $r \rightarrow 0$ , while  $h_\ell(r)$  and  $n_\ell(r)$  diverge for  $r \rightarrow 0$ .

## Spherical finite range potential

In the following, the scattering process due to a single-site central potential with a finite range is discussed. The Schrödinger equation for a single-site scattering with a potential  $V(\vec{r})$  is given in following form:

$$[E - \mathcal{H}_0 - V(r)]\psi(r) = 0. \quad (3.3.6)$$

When the potential is spherical, one can use a separation of coordinates to describe the wave function  $\psi(r) = \sum_L Y_L(\hat{r}) R_\ell(r, E)$ , with radial scattering wavefunctions  $R_\ell(\vec{r}, E)$ , to satisfy the radial Schrödinger equation:

$$\left[ -\frac{1}{r} \frac{\partial}{\partial r^2} r + \frac{\ell(\ell+1)}{r^2} + V(r) - E \right] R_\ell(\vec{r}, E) = 0. \quad (3.3.7)$$

At the region where  $V_r = 0$  ( $r > r_{\max}$ ), the radial wave function is given by two linearly independent solutions in terms of Bessel and Neumann functions:

$$R_\ell(r; E) = P_\ell j_\ell(kr) + Q_\ell n_\ell(kr), \quad (3.3.8)$$

where  $P_\ell$  and  $Q_\ell$  are constants. By using the asymptotic behaviors of these two functions and redefining the constants  $P_\ell$  and  $Q_\ell$  in terms of a new variable  $\delta_\ell$ , one can get:

$$R_\ell(r; E) = \frac{1}{kr} \left[ \sin \left( kr - \frac{\ell\pi}{2} + \delta_\ell(E) \right) \right]. \quad (3.3.9)$$

Here,  $\delta_\ell$  is the phase shift of the wave function due to the scattering by a single potential. At the region where  $V(r)$  is finite, the regular solution of the radial Schrödinger equation,  $R_\ell(r; E)$ , is given by two parts i.e., the potential-free solution which is the incoming scattering-free wave,  $j_\ell(kr)$ , and the resulting wave function which is scattered at the potential. By employing the Lippmann-Schwinger equation (Eq. 3.2.15) and the Green function of the free-electron (see Eq. 3.3.5), the regular solution can be expressed as [5]:

$$R_\ell(r; E) = j_\ell(kr) - ih_\ell^{(1)}(kr) \int_0^{r_{max}} r'^2 dr' j_\ell(kr') V(r') R_\ell(r'; E). \quad (3.3.10)$$

The integral on Eq. 3.3.10 is the single site scattering  $t$ -matrix in angular-momentum representation which gives the scattering strength of an incoming wave due to influence of the potential. In terms of the phase-shift the  $t$ -matrix can be expressed as:

$$t_\ell(E) = -\frac{1}{k} e^{i\delta_\ell(E)} \sin \delta_\ell(E). \quad (3.3.11)$$

Apart from the regular solution given in Eq. 3.3.10, there is also the irregular solution,  $H_\ell(r, E)$ , of the radial Schrödinger equation corresponds to Hankel function  $h_\ell(\sqrt{E}r)$  which diverges at the origin. Making use of the Lippmann-Schwinger equation (Eq. 3.2.15), one can express the irregular solution in terms of free electron Green functions as follows:

$$H_\ell(r; E) = h_\ell(\sqrt{E}r) + \int_0^{r_{max}} r'^2 dr' g_\ell(r, r'; E) V(r') H_\ell(r'; E). \quad (3.3.12)$$

Substituting Eq. 3.3.5 into Eq. 3.3.12, for the limit  $r > r_{max}$ , the Hankel function can be simplified as [5]:

$$H_\ell(r; E) = h_\ell(\sqrt{E}r). \quad (3.3.13)$$

The angular-dependent solutions of the Schrödinger equation are spherical harmonics, which allows to construct the full solutions of the single potential scattering problem as [46]:

$$\begin{aligned}
R_L(\vec{r}; E) &= \sum_L R_\ell(r; E) Y_L(\hat{r}) \\
H_L(\vec{r}; E) &= \sum_L H_\ell(r; E) Y_L(\hat{r}),
\end{aligned} \tag{3.3.14}$$

where  $R_L(\vec{r}; E)$  and  $H_L(\vec{r}; E)$  are the regular and irregular full solutions of the Schrödinger equation. Thus, the Green function of the single scattering problem can now be expressed as the product of these two solutions [86]:

$$\begin{aligned}
G_P(r, r'; E) &= -i\sqrt{E} \sum_L R_L(\vec{r}; E) H_L(\vec{r}; E) \\
&= -i\sqrt{E} \sum_L R_\ell(\sqrt{E}r_<) H_\ell(\sqrt{E}r_>) Y_L(\vec{r}) Y_L(\vec{r}').
\end{aligned} \tag{3.3.15}$$

### 3.3.2 Multiple scattering theory

In the previous section, the scattering process due to the single site potential was discussed. In this section, the discussion will be extended to the study of the scattering process in solids, where the scattering events are taking place due to a set of scatters. For the sake of simplicity, in the following discussion the muffin-tin (MT) approximation is used to describe each scattering potential, in which the potential is assumed to be spherically symmetric inside the muffin-tin radius  $R_{MT}$  and constant outside it. Within this thesis, however, the calculations are done using the full potential treatment to take into account the non-spherical symmetry of atoms due to their neighbouring scatterers. The calculation method also takes into account the treatment of non-collinear magnetism, of the spin-orbit interaction. The details explanation about the full potential treatment can be seen in Ref. [5].

The potential at each scattering site,  $m$ , is considered as a perturbation,  $\Delta V_m$ , to the unperturbed Hamiltonian, with the total of perturbation is given as  $\Delta V_{\text{tot}} = \sum_m \Delta V_m$ . For the case in which these multiple perturbing potentials act simultaneously, one then can define the total scattering matrix  $\mathbf{T}$  that contains all the scattering events in the lattices as:

$$\mathbf{T} = \sum_m \mathbf{t}^m + \sum_m \sum_{n \neq m} \mathbf{t}^m \mathbf{G}_0 \mathbf{t}^n + \dots, \tag{3.3.16}$$

where  $\mathbf{t}_m$  and  $\mathbf{t}_n$  are the scattering matrix elements ( $t$ ) of atoms at site  $m$  and  $n$ ,  $\mathbf{G}_0$  is the free-particle Green function. The first term in Eq. 3.3.16 can be interpreted as a single scattering process taking place in one particular site  $m$ . The second term deals with the scattering events between two lattice sites with a propagation between them and following terms describe multiple scattering events [103]. The  $\mathbf{T}$  matrix can also be presented in terms of the scattering path operator  $\boldsymbol{\tau}$  which describes all possible scattering events that can occur for an electron travelling from one site  $m$  to a site  $n$ :

$$\mathbf{T} = \sum_{mn} \boldsymbol{\tau}^{mn}. \tag{3.3.17}$$

In terms of single site scattering matrix  $\mathbf{t}$  and free space Green function  $G_0$ , the scattering path operator is given by

$$\boldsymbol{\tau}^{mn} = \mathbf{t}^m \delta_{mn} + \mathbf{t}^m \sum_{k \neq n} G_0^{\text{mk}} \boldsymbol{\tau}^{\text{kn}}. \quad (3.3.18)$$

As in the single scattering case one can also derive the free space Green function,  $G'_0$ , and the crystal Green function,  $G'_P$ , for the case of multiple scatterers. Due to the periodicity inherent of a crystal, the space now is divided into cells around each atom (see figure 3.1). The lattice cell is centered at the position  $\vec{R}_n$ . A point within the cell is denoted by the relative vector  $\vec{r}_n$  and its vector position from the origin denoted by vector  $\vec{x}$ , as shown in Fig. 3.1. Then, the free space Green can be written in the cell-centred representation as:

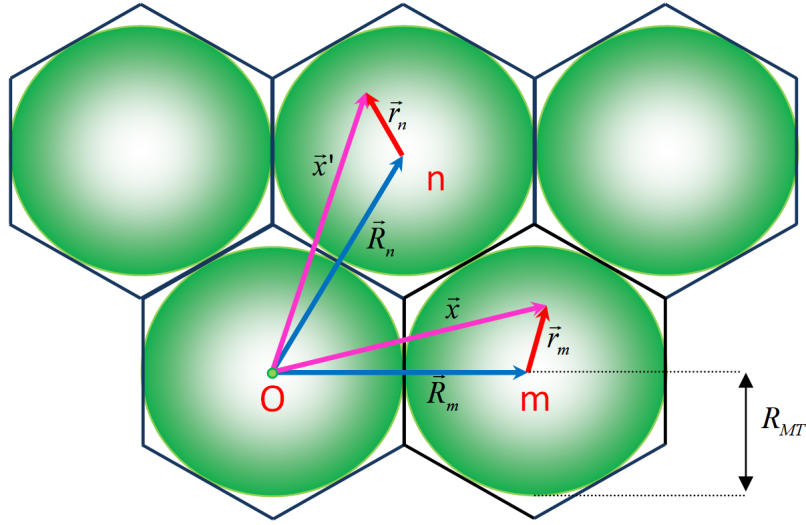


Figure 3.1: Illustration of two scatterer sites  $m$  and  $n$ . The globally defined vectors  $\vec{x}$  and  $\vec{x}'$  are given by  $\vec{R}_m + \vec{r}_m$  and  $\vec{R}_n + \vec{r}_n$  respectively.  $R_{MT}$  indicates the Muffin-Tin radius.  $R_m$  and  $R_n$  are a global vector pointing to the center of cell  $m$  and  $n$  respectively, whereas the vectors  $r_m$  and  $r_n$  are locally defined inside the cell.

$$G'_0(\vec{R}_m + \vec{r}_m, \vec{R}_n + \vec{r}_n, E) = -i\sqrt{E} \sum_L j_L(\vec{r}_m) h_L(\vec{r}_n + \vec{R}_n - \vec{R}_m, E). \quad (3.3.19)$$

Using the expansion of the Hankel Function [105]:

$$h_L(\vec{r}_n + \vec{R}_n - \vec{R}_m, E) = \frac{i}{\sqrt{E}} \sum_{L'} g_{LL'}^{mn} j_{L'}(\vec{r}_n, E), \quad (3.3.20)$$

one can rewrite the free space Green function as:

$$G'_0(\vec{R}_m + \vec{r}_m, \vec{R}_n + \vec{r}_n, E) = \sum_{LL'} j_L(\vec{r}_m, E) g_{LL'}^{mn} j_{L'}(\vec{r}_n, E), \quad (3.3.21)$$

where  $g_{LL'}$  is called “structure constant” which depends only on the lattice structure and it is given by:

$$g_{LL'}^{mn} = -(1 - \delta_{mn})4\pi i\sqrt{E} \sum_{L''} i^{l-l'-l''} C_{LL'L''} h_{L''}(\vec{R}_m - \vec{R}_n; E), \quad (3.3.22)$$

with  $C_{LL'L''} = \int d\Omega Y_L(\hat{r}) Y_{L'}(\hat{r}) Y_{L''}(\hat{r})$  being the Gaunt coefficients. As  $m$  and  $n$  refer to two different scattering sites, it implies that  $g_{LL'}^{mn} = 0$ , for  $m = n$ . Henceforth, the general expression for the free space Green function can be written as:

$$G'_0(\vec{R}_m + \vec{r}_m, \vec{R}_n + \vec{r}_n, E) = \delta_{mn} G_0(\vec{r}_m, \vec{r}_n; E) + \sum_{LL'} j_L(\vec{r}_m; E) g_{LL'}^{mn} j_{L'}(\vec{r}_n; E), \quad (3.3.23)$$

where the potential-free Green function within one site (i.e.  $m = n$ ),  $G_0(\vec{r}_m, \vec{r}_n; E)$ , was also included. As one can see from Eq. 3.3.23, there is a clear separation between the single-site properties described by  $G_0(\vec{r}_m, \vec{r}_n; E)$  and the multiple scattering properties as described by the structure constant matrix  $g_{LL'}^{mn}$ . This separation is one of the main features of the KRR Green function method [79].

Using a similar procedure (Eq. 3.3.23), the Green function  $G'_P$  of a host crystal with at a finite potential  $V(\vec{r})$  can be derived as:

$$G'_P(\vec{R}_m + \vec{r}_m, \vec{R}_n + \vec{r}_n, E) = \delta_{mn} G_P(\vec{r}_m, \vec{r}_n; E) + \sum_{LL'} R_L^m(\vec{r}_m; E) G_{LL'}^{mn} \bar{R}_{L'}^n(\vec{r}_n; E). \quad (3.3.24)$$

Here, the first term is the single-site crystal Green function at site  $m$  with a finite central potential (see Eq. 3.3.15). The second term is the multiple scattering term which includes the structural Green functions  $G_{LL'}^{mn}$  that can be determined by the following structural (algebraic) Dyson equation [25, 6]:

$$G_{LL'}^{mn}(E) = g_{LL'}^{mn}(E) + \sum_p \sum_{L''L'''} g_{LL''}^{mp}(E) t_{L''L'''}^p G_{L''L'''}^{pn}(E). \quad (3.3.25)$$

Expanding the sum on the right-hand side of Eq.3.3.25, one can obtain:

$$\begin{aligned} G_{LL'}^{mn}(E) &= g_{LL'}^{mn}(E) + \sum_p \sum_{L''L'''} g_{LL''}^{mp}(E) t_{L''L'''}^p G_{L''L'''}^{pn}(E) \\ &+ \sum_{pq} \sum_{L''L'''} g_{LL''}^{mp}(E) t_{L''L'''}^p g_{L''L'''}^{pq}(E) t_{L''L'''}^q g_{L''L'''}^{qn}(E) + \dots \end{aligned} \quad (3.3.26)$$

where  $g_{LL'}^{mn}$  is the structural Green function for the free-electron case given by Eq. 3.3.22. The  $t$ -matrix terms are identified as a scattering matrix transforming an incoming spherical wave into a scattered wave at a finite potential  $V_m$  around a cell  $m$ .

In practice, the calculation of Green functions is first performed in  $\vec{k}$ -space for a periodic system. The structural Green functions  $G_{LL'}^{mn}(E)$  is solved by matrix inversion after a cutoff at  $\ell = \ell_{max}$  for which the  $t$ -matrix becomes negligible [73, 93].

By introducing the Fourier transform of the structure constants in reciprocal space,  $G_{LL'}^{mn}(\vec{k}, E)$

$$G_{LL'}^{\mu\mu'}(\vec{k}, E) = \sum_n G_{LL'}^{m\mu, n\mu'} e^{-i\vec{k}(\vec{R}_m - \vec{R}_n)}, \quad (3.3.27)$$

the Dyson equation for the structural Green function in  $\vec{k}$ -space can be set up as:

$$G_{LL'}^{\mu\mu'}(\vec{k}, E) = g_{LL'}^{\mu\mu'}(\vec{k}, E) + \sum_{\mu} \sum_{L''L'''} g_{LL''}^{\mu\mu''}(\vec{k}, E) t_{L''L'''}^{\mu} G_{L''L'''}^{\mu''\mu'}(\vec{k}, E). \quad (3.3.28)$$

From Eq. 3.3.28, the  $k$ -dependent structural Green functions can be obtained by matrix inversion. Afterwards, the resulting structural Green function in  $\vec{k}$ -space can be back-transformed by an inverse Fourier transformation [5, 46]:

$$G_{LL'}^{mn}(E) = \frac{1}{\Omega_{BZ}} \int_{BZ} d\vec{k} e^{i\vec{k}(\vec{R}_m - \vec{R}_n)} G_{LL'}^{\mu\mu'}(\vec{k}, E), \quad (3.3.29)$$

where  $\Omega_{BZ}$  denotes the volume of the first Brillouin zone where the integral is performed. In reciprocal space representation, one can also find the bandstructure  $E(\vec{k})$  of the crystal by the KKR secular equation which is given by:

$$\sum_{L'\mu'} \left( \delta_{LL'} \delta_{\mu\mu'} - \sum_{L''} G_{LL''}^{\mu\mu''}(\vec{k}, E) \Delta t_{L''L'}^{\mu''} \right) c_{\vec{k}L'}^{\mu'} = 0, \quad (3.3.30)$$

where  $\mu$  is one of a finite number of basis atoms at  $\mathcal{X}_{\mu'}$  and  $\Delta t_{L''L'}^{\mu''}$  is the difference of the  $t$ -matrix between the reference system and the free space. The coefficients  $c_{\vec{k}L'}^{\mu'}$  are the eigenvectors of the total incoming wave at the scatterer atom at  $\mathcal{X}_{\mu'}$ .

The structural Dyson equation is an essential concept in the KKR-Green function impurity method since it allows one to calculate the electronic structure of a crystal in the presence of an impurity. It makes this method more efficient than the other wavefunctions-based DFT approaches, for instance the plane wave methods, as the calculation of the electronic structure does not require the construction of supercells. The method uses a Green function approach in real space to embed an impurity region into a solid [5]. In the following discussion, the impurity calculation using the KKR-Green function impurity method will be explained in more detail.

### 3.3.3 Impurity calculations

The fact that real materials are not perfect crystals is critical to their future application in materials engineering and technology. The presence of impurities impact the physical properties of materials. Therefore, it is necessary to study how such defects affects the electronic structure and properties of solids. Usually, the methods used to describe the electronic structure of solids with impurities are based on band-structures methods which rely on the translational invariance of potential. This condition leads to a requirement of extremely large cells which can cost a high numerical effort.

Another alternative that can be used without requiring the construction of supercells is by using the KKR impurity method. This approach employs the Green function formulation in real space to embed an impurity region into a solid and does not rely on a supercell [5]. The procedure is given in two steps, the Green function of the host is calculated firstly via the KKR band structure method in  $\vec{k}$ -space. Then, impurity atoms are embedded into the crystal structure in real space using the Dyson equation (see Figure 3.2). In  $k$ -space representation (Eq.3.3.27), the structural host

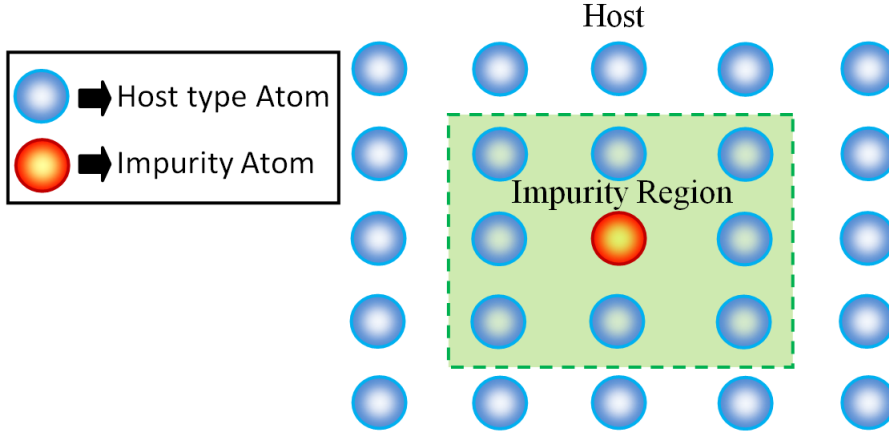


Figure 3.2: Illustration of an impurity embedded in the clean host system. The blue spheres represent the host atoms whilst the red one is the impurity atom. The green square represents the impurity region

Green function  $G_{host,LL'}^{mn}(E)$  is calculated by using of the translational invariance to convert the complexity of two discrete lattice indices to a continuous variable  $\vec{k}$  which is defined inside the Brillouin zone (see Eq. 3.3.28). This allows one to write the Dyson equation for the structural Green function for the host system as:

$$G_{host,LL'}^{\mu\mu'}(\vec{k}, E) = g_{LL'}^{\mu\mu'}(\vec{k}, E) + \sum_{\mu''} \sum_{L''L'''} g_{LL''}^{\mu\mu''}(\vec{k}, E) \mathbf{t}_{L''L'''}^p G_{L''L'''}^{\mu''\mu'}(\vec{k}, E). \quad (3.3.31)$$

By employing a matrix inversion and use the inverse Fourier transformation as given in Eq. 3.3.29, one can determine the  $G_{host,LL'}^{mn}(E)$  in real space representation. Once the structural Green function of the host system is known, one can use the obtained result to calculate the impurity Green function  $G_{imp,LL'}^{mn}(E)$ . This can be done by embedding an impurity subsystem into a host reference system via the Dyson equation [5]. As the perturbation caused by the substitutional impurity is typically restricted to few neighbouring atomic shells, there is only a finite region of space which is practically influenced [28]. Outside, the induced perturbation in the potential is small and can be neglected, meaning that the potential equals the host potential [5]. Therefore, this embedding technique allows one to substitute the host potentials in the impurity region by potentials  $V_{imp}$ , in order to obtain the structural Green function [93] as shown below:

$$G_{\text{imp},LL'}^{mn} = G_{\text{host},LL'}^{mn} + \sum_p \sum_{L''L'''} G_{LL''}^{mp} \Delta t_{L''L'''}^p G_{\text{imp},LL'}^{pn}, \quad \Delta t_\ell^p = t_{\text{imp},\ell}^p - t_{\text{host},\ell}^p, \quad (3.3.32)$$

where  $\Delta t_\ell^p$  denotes the  $t$ -matrix difference between the  $t$ -matrix of the impurity potential  $V_{\text{imp}}(\vec{r})$  and the host potential  $\tilde{V}_{\text{host}}(\vec{r})$ .

Thus, in matrix equation with a combined index  $(L, m)$ , one can rewrite Eq. 3.3.32 as:

$$\mathbf{G}_{\text{imp}} = \mathbf{G}_{\text{host}} + \mathbf{G}_{\text{host}} \Delta \mathbf{t} \mathbf{G}_{\text{imp}} \quad (3.3.33)$$

Therefore, the Green function  $\mathbf{G}_{\text{imp}}$  can be determined numerically via a matrix inversion

$$\mathbf{G}_{\text{imp}} = (1 - \mathbf{G}_{\text{host}} \Delta \mathbf{t})^{-1} \mathbf{G}_{\text{host}}. \quad (3.3.34)$$

### 3.4 Self-consistency algorithm

In the following, the algorithm to calculate the potential self-consistently using the KKR Green function method is briefly presented. The basic and central quantity to be calculated in this procedure is the electronic density. One should notice that the procedure presented here does not include the spin orbit coupling. The steps followed are ([93])

1. Taking an initial guess of an input potential  $V_{\text{imp}}(\vec{r})$  (see the top green line box in Figure 3.3).
2. Calculate the wavefunctions  $R_L(\vec{r})$ ,  $H_L(\vec{r})$  and also the  $t$ -matrix elements,  $t_{LL'}(E)$ .
3. Calculate the  $t$ -matrix elements of the reference system  $t_{LL'}^0(E)$ , and calculate  $\Delta t_{LL'}(E) = t_{LL'}(E) - t_{LL'}^0(E)$  (look at the first red line box in Figure 3.3).
4. Calculate the structural Green function  $G_{LL'}^{0,mn}(E)$  of the reference system.
5. Evaluate the structural Green function of the real system  $G_{LL'}^{mn}(E)$  by solving the structural Dyson Equation (Eq.3.3.25).
6. Calculate the Green function using the structural Green function  $G_{LL'}^{mn}(E)$ ,  $R_L(\vec{r})$ , and  $H_L(\vec{r})$ . After that, integrate the Green function by using a complex-energy contour and take the imaginary part to find the valence electron density.  $\rho^\nu(r) = -\frac{1}{\pi} \text{Im} \int_{E_{\text{bot}}}^{E_F} dZ G(r, r'; Z)$ .
7. Calculate the core-electron wavefunctions and core-electron density  $\rho^c$ ; here, the multiple-scattering formalism is not needed, because the core wavefunctions are assumed to be highly localized at the atomic sites. Obtain the total density  $\rho(r) = \rho^c(r) + \rho^\nu(r)$ .

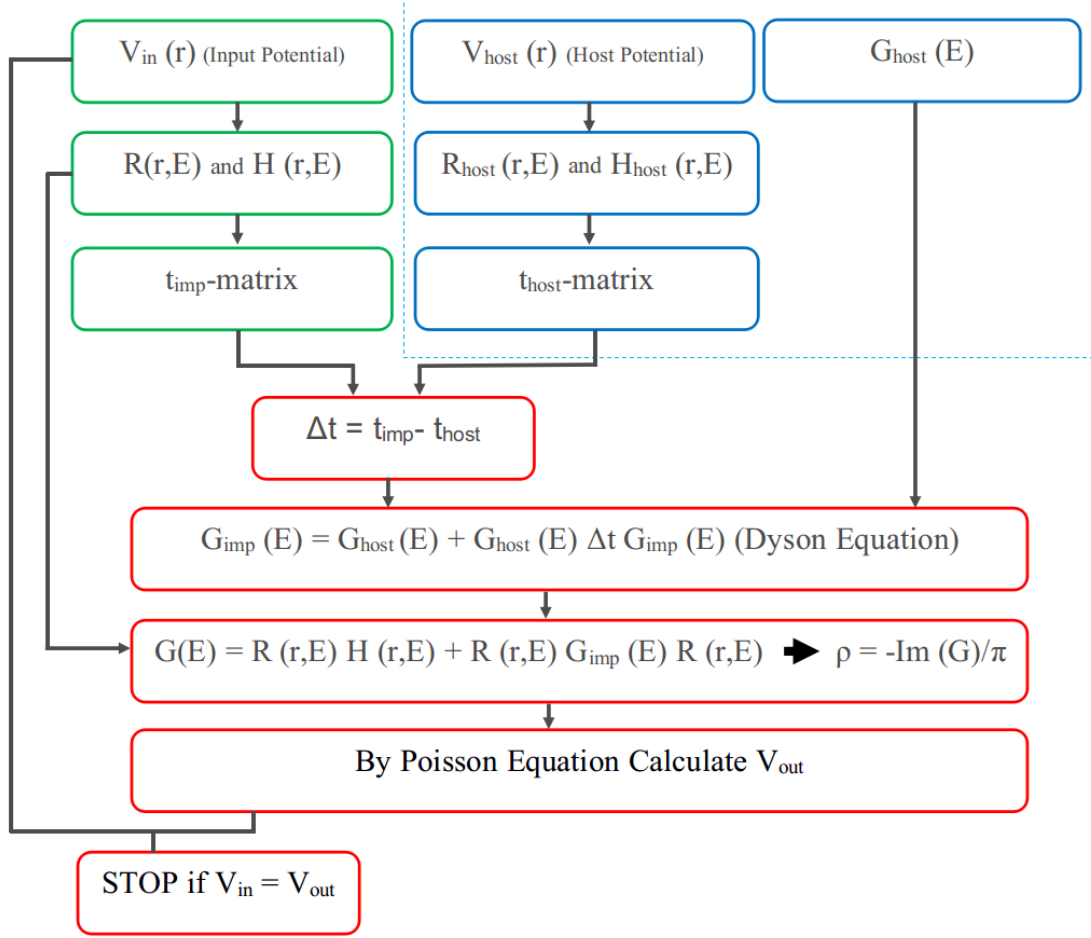


Figure 3.3: The diagram of self-consistency cycle used in the KKR method for impurity calculations

8. Calculate the output potential  $V_{\text{out}}(\vec{r})$  by solving the Poisson equation which is given by  $\nabla^2 V = -\frac{\rho}{\epsilon_0}$  and adding the exchange-correlation potential. If  $V_{\text{inp}}(\vec{r}) = V_{\text{out}}(\vec{r})$  to a reasonable accuracy, exit the cycle. Otherwise:
9. Properly mix  $V_{\text{out}}(\vec{r})$  with  $V(\vec{r})$  to obtain a new input potential, and return to the initial step.

# Chapter 4

## Parametrization of the magnetic Hamiltonian

The description of many properties of magnetic materials, such as their behavior at finite temperatures and large-scale magnetic textures, are in many cases impossible to treat directly via first-principles methods. To overcome such difficulties, effective models are often used to depict the interactions between magnetic moments in real materials. One of the most successful methods is to make use of the Heisenberg Hamiltonian with parameters obtained from first-principles calculations [96, 27].

The original Heisenberg Hamiltonian describes the interaction between a magnetic moment,  $\vec{m}$ , of an atom with its nearest neighbors. In this model the magnetic moments,  $\hat{m}_i$ , are three-dimensional unit vectors with a fixed length. The interactions among them are described by the following expression:

$$\mathcal{H}_{\text{Heis}} = - \sum_{\langle ij \rangle} J_{ij} \hat{m}_i \cdot \hat{m}_j, \quad (4.0.1)$$

where  $\hat{m}_i$  is the direction of the magnetic moment at  $i$ -th site and the  $J_{ij}$ 's are the Heisenberg exchange couplings which describe the interaction between the  $i$ -th and  $j$ -th magnetic moments. When  $J_{ij} > 0$ , the magnetic moments prefer a parallel orientation, that is a *ferromagnetic* alignment, whilst if  $J_{ij} < 0$  an anti-parallel alignment minimizes the energy, i.e an *anti-ferromagnetic* state.

Such Heisenberg Hamiltonian, including only the pairwise exchange interaction between nearest neighbor magnetic moments, is sometimes used to describe the properties of certain magnetic systems. However, it is limited, as it cannot be used to describe more complex magnetic configurations, for instance, a non-trivial magnetic structure such as skyrmions. As they are often present in materials with large spin orbit coupling, the effects that can also be included in the Heisenberg Hamiltonian by adding extra terms such as the Dzyaloshinskii-Moriya interaction [26, 75] and the magnetocrystalline anisotropy energy (MAE). This extended Heisenberg Hamiltonian is given by:

$$\mathcal{H}_{\text{Heis}} = - \sum_{i \neq j} J_{ij} \hat{m}_i \cdot \hat{m}_j - \sum_{i \neq j} \vec{D}_{ij} \cdot (\hat{m}_i \times \hat{m}_j) + \sum_i K_i (\hat{e}^k \cdot \vec{m}_i)^2 - \sum_i \vec{m}_i \cdot \vec{B}_{\text{ext}}. \quad (4.0.2)$$

The first term in Eq. 4.0.2 is the previously discussed isotropic Heisenberg exchange interactions. Notice that it is now a long-range interaction taking into account several coordination shells. The second term is the anti-symmetric Dzyaloshinskyii-Moriya (DM) interaction with  $\vec{D}_{ij}$  being the Dzyaloshinskii-Moriya vector between the  $i$ -th and the  $j$ -th atoms. As can be seen, this term favors non-collinear magnetic structures with its contribution being minimal when the spins are perpendicular to one another. This term is also *chiral*, since as one can see its energy depends on the cross product between the magnetic moments [11], thus a certain rotational sense of the magnetic moments is preferred.

The term  $\sum_i K_i (\hat{e}^k \cdot \vec{m}_i)^2$  is the uniaxial magnetocrystalline anisotropy energy with  $K_i$  being the uniaxial anisotropy constant [16] for the  $i$ -th atom. This describes the tendency that magnetic moments have in certain materials to prefer a given orientation with respect to the lattice, which is a direct result from the spin orbit coupling.

The last term in Eq. 4.0.2 is the Zeeman term which is the interaction with an external magnetic field  $\vec{B}_{\text{ext}}$ .

Until now, a description of how one can use the Heisenberg Hamiltonian to describe different magnetic configurations has been presented. However, the link between this model and real materials is still missing. Thus, in this chapter, a description of the method used to parametrize the Heisenberg Hamiltonian from first principles methods will be presented, with special emphasis on the parameters needed to describe materials where magnetic skyrmions are present.

## 4.1 Calculation of the exchange interaction parameters

The Heisenberg exchange interactions are usually the dominant terms in a magnetic material [55]. Hence, being one of the main responsible for the ground state of the system. As previously mentioned, depending on its sign the magnetic moments prefers different alignments, ferromagnetic (anti-ferromagnetic), i.e. parallel(antiparallel) for positive(negative) sign of the exchange coupling. One of the methods used to calculate the pairwise Heisenberg exchange interaction is the so-called Liechtenstein-Katsnelson-Antropov-Gubanov formalism (LKAG) [66, 65]. This method is based on Andersen's Force theorem which allows the calculation of the exchange parameter by considering a small deviation of the magnetization from a reference state [3].

One can start by looking at the isotropic exchange interaction term [66, 55]:

$$\mathcal{H}_{\text{xc}} = - \sum_{i \neq j} J_{ij} \hat{m}_i \cdot \hat{m}_j. \quad (4.1.1)$$

Considering the ferromagnetic configuration as the ground state, one can evaluate the variation of the exchange energy shown in Eq. 4.1.1 due to the infinitesimal rotation of the local moment at site  $i$  by the angle  $\theta$  as following:

$$\begin{aligned}\delta E &= -2 \sum_n J_{in} [\cos \theta - 1] \\ &\approx \sum_n J_{in} \theta^2.\end{aligned}\tag{4.1.2}$$

It is also useful to consider the rotation of two atoms ( $i$  and  $j$ ) by an angle ( $\pm\theta/2$ ) with the variation of exchange energy  $\delta E_{ij}$  given by:

$$\delta E_{ij} = -2 \sum_{n \neq i, n \neq j} J_{in} \left[ \cos \left( \frac{\theta}{2} \right) - 1 \right] - 2 \sum_{m \neq i, m \neq j} J_{jm} \left[ \cos \left( \frac{\theta}{2} \right) - 1 \right] - 2J_{ij} [\cos \theta - 1],\tag{4.1.3}$$

with  $n$  and  $m$  refer to background atoms, namely all the atoms around atoms  $i$  and  $j$ . To obtain the pairwise exchange interaction constant,  $J_{ij}$ , between two magnetic moments at site  $i$  and  $j$ , one also needs to subtract the variation of the interaction energy of each atom ( $i$  and  $j$ ) with the environment. This can be obtained by rotating only one of the two atoms with the same angle as assumed when calculating  $\delta E_{ij}$  (see Eq. 4.1.3). By doing this procedure one get the change of energy related to the  $J_{ij}$  parameters as follows (detail derivation can be seen in Appendix A.3):

$$\delta E'_{ij} \approx \frac{1}{2} J_{ij} \theta^2.$$

Thus, it has been shown that up to second order perturbation one can relate the change of magnetic energy due to a two-site rotation to the magnitude of the exchange couplings. Hence, if one assumes that the Heisenberg Hamiltonian represents the magnetic energy of a real magnetic material, then by calculating such kind of energy differences in the context of density functional theory, it is in principle possible to calculate these parameters, which is precisely the approach proposed by Liechtenstein et al. [66, 65].

In the LKAG formalism, a small perturbation from the ground state is considered and therefore, Andersen's "local force theorem" [3] can be used. It states that the total change in the energy due to small perturbations can also be related to the sum of the variations of single-particle energy while keeping the ground state potential fixed. Thus one can write:

$$\delta E = - \int_{-\infty}^{\epsilon_F} \delta N(\epsilon) d\epsilon.\tag{4.1.4}$$

In Eq. 4.1.4  $\delta N(\epsilon)$  is the variation of the integrated density of states. In multiple scattering theory, the variation of  $N$  can be expressed as a function of the scattering path operator as [69]:

$$\Delta N(\epsilon) = \frac{1}{\pi} \text{Im Tr ln } \tilde{\tau}(\epsilon),\tag{4.1.5}$$

where  $\tilde{\tau}$  denotes the scattering path operator in the ground state, then in the presence of a local perturbation it becomes:

$$\tilde{\tau}' = \tilde{\tau}[1 + \delta\mathbf{t}^{-1}\tilde{\tau}]^{-1}, \quad (4.1.6)$$

with  $\delta\mathbf{t}^{-1}$  being the change of the inverse single site scattering matrix,  $\mathbf{t}$ . By substituting Eq. 4.1.5 and Eq. 4.1.6 into Eq. 4.1.4, one can rewrite the expression for the energy variation as follows:

$$\delta E = \frac{1}{\pi} \int_{-\infty}^{\epsilon_F} d\epsilon \operatorname{Im} \operatorname{Tr} \ln (1 + \delta\mathbf{t}^{-1}\tilde{\tau}). \quad (4.1.7)$$

The variation of the inverse  $\mathbf{t}^{-1}$  matrix in Eq.4.1.7 can be expressed as:

$$\delta\mathbf{t}_i^{-1} = \frac{1}{2} (\mathbf{t}_{i\uparrow} - \mathbf{t}_{i\downarrow}) (\delta\vec{e}_i \cdot \vec{\sigma}), \quad (4.1.8)$$

where  $\mathbf{t}_{i\uparrow(\downarrow)}$  is the single site scattering matrix for spin up(down) at site  $i$ ,  $\vec{\sigma}$  is the vector of Pauli matrices and with  $\delta\vec{e}_i$  being the variation of the orientation of the magnetic moment. For simplicity, one can choose the reference configuration to be the ferromagnetic state, with the magnetic moments along the z-direction (0,0,1). Thus, in the single-site rotation the orientation of a single spin, deviated by an angle  $\theta$ , can be written as  $\hat{e}_i = (\sin \theta, 0, \cos \theta)$ . By comparing Eq. 4.1.2 and Eq. 4.1.7, one can then write the effective exchange interaction parameter, related to the single site rotation by keeping the terms up to order  $\delta\theta^2$  as:

$$J_0 = -\frac{1}{4\pi} \int_{-\infty}^{\epsilon_F} d\epsilon \operatorname{Tr}_L [\Delta(\tilde{\tau}_\uparrow - \tilde{\tau}_\downarrow) + \Delta\tilde{\tau}_\uparrow\Delta\tilde{\tau}_\downarrow]. \quad (4.1.9)$$

In Eq. 4.1.9  $J_0$  represents the exchange parameter of the single site rotation with  $\Delta = \mathbf{t}_\uparrow^{-1} - \mathbf{t}_\downarrow^{-1}$ , and  $\tilde{\tau}_{\uparrow(\downarrow)}$  is defined as scattering path operator (see Eq. 3.3.18) for spin up(down). The  $\operatorname{Tr}_L$  is the trace over the orbital variables of scattering matrices [65].

In a similar way, one can also find the exchange interaction parameter for the pair interactions by rotating two magnetic moments on the sites  $i$  and  $j$  with a small deviation  $\pm\frac{\theta}{2}$ , allowing one to write:

$$J_{ij} = \frac{1}{4\pi} \int_{-\infty}^{\epsilon_F} d\epsilon \operatorname{Tr}_L [(\mathbf{t}_{i\uparrow}^{-1} - \mathbf{t}_{i\downarrow}^{-1})\tilde{\tau}_\uparrow^{ij} (\mathbf{t}_{j\uparrow}^{-1} - \mathbf{t}_{j\downarrow}^{-1}) \tilde{\tau}_\downarrow^{ji}]. \quad (4.1.10)$$

In 4.1.9  $J_0$  gives the expression for the effective exchange interaction parameter of the spin moment at site 0 with the spin polarized background and is determined by the pairwise exchange interactions. On the other hand, Eq. 4.1.10 showcases the pair exchange interactions parameter between spin moments at sites  $i$  and  $j$  [65]. The first term defines the scattering of the incoming electronic state at the  $i$ -th site due to the effective potential, as described by the single-site scattering matrix. The resulting wave function propagates from the  $i$ -th site to the  $j$ -th site as represented by  $\tilde{\tau}^{ij}$ . The scattering process is then taking place at site  $j$  and is shown by the scattering matrix with indices  $j$ . The last term,  $\tilde{\tau}^{ji}$ , shows the propagation of the scattered wave function from site  $j$  back to site  $i$ . Thus, the exchange interaction between these two sites can be determined irrespective of the distance between them.

## 4.2 Calculation of Dzyaloshinskii-Moriya vectors

As mentioned in the previous section, the exchange interaction parameter can be used to describe the magnetic configuration of a system exhibiting collinear or in some cases, due to exchange frustration, a non-collinear order. However, to describe a system with chiral magnetic ordering, one needs to consider another interaction in the Hamiltonian. A term that can be used to explain this kind of magnetic configurations was first proposed by Dzyaloshinskii [26], and later expanded by Moriya [75]:

$$\mathcal{H}_{\text{DMI}} = - \sum_{i \neq j} \vec{D}_{ij} \cdot (\hat{m}_i \times \hat{m}_j), \quad (4.2.1)$$

where the  $\vec{D}_{ij}$ 's are the Dzyaloshinskii-Moriya vector and  $\hat{m}$  is the unit vector of the magnetic moment.

The DM interaction is relativistic in origin, that is it requires the presence of spin orbit coupling (SOC), but it also needs a system with broken inversion symmetry [75] to be present. One type of systems that is known to exhibit strong DMI are magnetic layers deposited on heavy metal substrates [74]. The breaking of inversion symmetry at the magnet/heavy metal interface in combination with the large SOC due to the underlayer gives rise to DMI [21]. It was shown by Fert and Levy [38], that the DMI on this type of system lays in a plane perpendicular to the bonding vector between the magnetic atoms, as shown in figure 4.1.

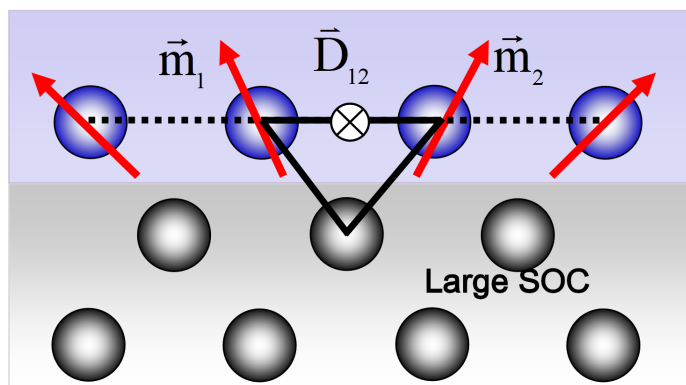


Figure 4.1: Schematic representation of the Dzyaloshinskii–Moriya interaction in multilayer stacks with broken inversion symmetry. The chiral coupling between two spins  $\vec{m}_1$  and  $\vec{m}_2$  is mediated by a heavy atom with large spin orbit coupling (grey atoms) in the non-magnetic layer. The resulting DMI ( $\vec{D}_{12}$ ) vector is perpendicular to the bond between two spins.

The direction of the DM vectors strongly depends on the symmetry of the underlying lattice. Moriya [75] proposed a set of rules that allow one to determine (for some cases) the orientation of the  $\vec{D}_{ij}$  vector between the  $i$ -th and  $j$ -th atoms. To illustrate them it is useful to consider that the  $i$ -th spin is located at the point  $A$ , and the  $j$ -th spin is at a point  $B$ , with the middle point,  $C$ , between these spins (see Figure 4.2).

- a) If a center of inversion is located at  $C$ :  $D = 0$ .

- b) When a mirror plane perpendicular through  $C$ ,  $D$  is  $\parallel$  to the mirror plane or  $D \perp AB$ .
- c) Where there is mirror plane including point  $A$  and  $B$ , then  $D$  is  $\perp$  to the mirror plane.
- d) When a two-fold rotation axis perpendicular to  $AB$  passes through  $C$ ,  $D$  is  $\perp$  to the two-fold axis.
- e) When there is an  $n$ -fold axis ( $n \geq 2$ ) along  $AB$ ,  $D$  is  $\parallel$  to  $AB$ .

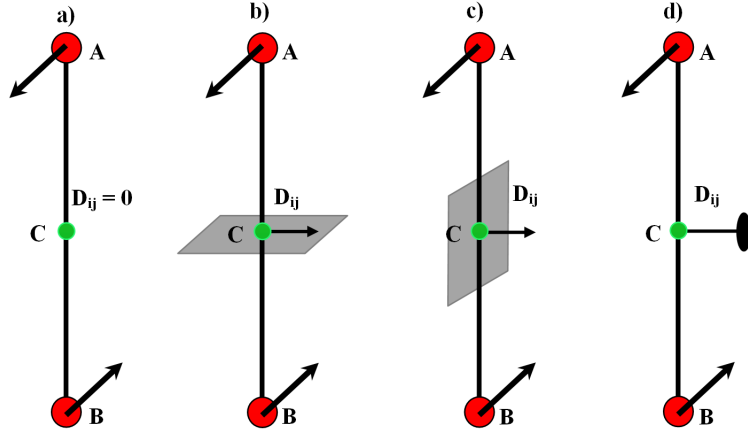


Figure 4.2: Schematic representation of the Dzyaloshinskii- Moriya vector for two spins located at site  $A$  and  $B$ . Different directions of the vector  $D_{ij}$  shown in a) with the center of inversion at middle point, b) with a mirror plane perpendicular through the point  $C$ , c) with a mirror parallel with the connecting line of two spins, and d) with rotation axis through the middle point  $C$ .

The calculation of the DM interaction parameters from first principles is of great importance to describe the magnetic properties of certain materials [96, 27]. Hence, it is imperative to develop a method to calculate such contributions. One approach which is of special interest for the study of skyrmion-defect interactions is the generalized LKAG formalism, which was first proposed by Udvardi et al. [96], and with an alternative approach proposed by Ebert and Mankovski [27]. Here, the effective spin Hamiltonian can be written in the most general form as:

$$\mathcal{H}_{\text{Heis}} = \sum_i K_i (\hat{m}^k \cdot \vec{m}_i)^2 + \sum_{ij} \vec{m}_i \tilde{\mathcal{J}}_{ij} \vec{m}_j, \quad (4.2.2)$$

where  $\vec{m}_i$  and  $\vec{m}_j$  define the direction of the atomic magnetic moment at site  $i$  and  $j$ , respectively. The term  $\sum_i K_i (\hat{m}^k \cdot \vec{m}_i)^2$  is the magnetocrystalline anisotropy energy with  $K$  as the uniaxial anisotropy constant. The  $\tilde{\mathcal{J}}_{ij}$  in Eq. 4.2.2 represents the exchange tensor in the form of  $3 \times 3$  matrix and it can be decomposed into three parts:

$$\mathcal{J}_{ij} = J_{ij} \mathbb{1} + \mathcal{J}_{ij}^S + \mathcal{J}_{ij}^A. \quad (4.2.3)$$

The first and second terms are the isotropic and the symmetric anisotropic exchange interaction, respectively which are defined in the following manner:

$$J_{ij} = \frac{1}{3} \text{Tr}\{\mathcal{J}_{ij}\}, \quad (4.2.4)$$

$$\mathcal{J}_{ij}^S = \frac{1}{2} (\mathcal{J}_{ij} + \mathcal{J}_{ij}^T) - J_{ij}\mathbb{1}, \quad (4.2.5)$$

where  $T$  in  $\tilde{\mathcal{J}}_{ij}^T$  refers to the transposed matrix. The third part of exchange tensor represents the anti-symmetric part of the exchange tensor which is related to the Dzyaloshinskii-Moriya interaction. The components of the vector  $D_{ij}$  are defined as:

$$\begin{aligned} D_{ij}^x &= \frac{1}{2} (J_{ij}^{yz} - J_{ij}^{zy}) \\ D_{ij}^y &= \frac{1}{2} (J_{ij}^{xz} - J_{ij}^{zx}) \\ D_{ij}^z &= \frac{1}{2} (J_{ij}^{xy} - J_{ij}^{yx}). \end{aligned} \quad (4.2.6)$$

In order to calculate the elements of the exchange coupling tensor,  $\mathcal{J}_{ij}$ , we can start to find the change in the energy with respect to an infinitesimal rotation of two magnetic moments. In terms of the change in the t-matrix and Green function, it is given by (see details in Ref. [5]):

$$\delta E_{ij} = -\frac{1}{\pi} \text{Im} \int dE \text{Tr} \delta \mathbf{t}_i \mathbf{G}_{ij} \delta \mathbf{t}_j \mathbf{G}_{ji}. \quad (4.2.7)$$

The difference between t-matrices resulting from a potential  $\mathbf{V}$  and a potential  $\mathbf{V} + \delta \mathbf{V}$  can be in first order calculated by:

$$\delta \mathbf{t}_i = \int dr \bar{\mathbf{R}}(\vec{r}) \delta \mathbf{V}_i \mathbf{R}(\vec{r}), \quad (4.2.8)$$

where  $\mathbf{R}(\vec{r})$  represents the wave functions resulting from a potential  $\mathbf{V}$  that can be decomposed into a scalar potential field  $\mathbf{V}(\vec{r})$  and a term acting like magnetic field  $\mathbf{B}(\vec{r})$ :

$$\mathbf{V}_i(r) = \mathbb{1} \cdot \mathbf{V}(r) + \vec{\sigma} \cdot \hat{e}_i^{(0)} \mathbf{B}_i(r), \quad (4.2.9)$$

where  $\vec{\sigma}$  is a vector containing the Pauli matrices. If the vector is rotated such that the resulting magnetic field is pointing along the unit vector  $\hat{e}_i$ , then the change in the potential can be calculated as follows:

$$\delta \mathbf{V}_i(r) = (\vec{e}_i \cdot \vec{\sigma}) \mathbf{B}_i(r). \quad (4.2.10)$$

By substituting Eq. 4.2.10 into Eq. 4.2.8, one can obtain:

$$\begin{aligned} \delta \mathbf{t}_i &= \int dr \bar{\mathbf{R}}(\vec{r}) (\vec{e}_i \cdot \vec{\sigma}) \mathbf{B}_i(r) \mathbf{R}(\vec{r}) \\ &= \vec{e}_i \cdot \int dr \bar{\mathbf{R}}(\vec{r}) \vec{\sigma} \mathbf{B}_i(r) \mathbf{R}(\vec{r}) \\ &= \vec{e}_i \cdot \begin{pmatrix} \delta \mathbf{t}_i^x \\ \delta \mathbf{t}_i^y \\ \delta \mathbf{t}_i^z \end{pmatrix}, \end{aligned} \quad (4.2.11)$$

with:

$$\mathbf{t}_i^\alpha = \int dr \bar{\mathbf{R}}(\vec{r}) \vec{\sigma}^\alpha \mathbf{B}_i(r) \mathbf{R}(\vec{r}), \quad (4.2.12)$$

where  $\alpha = (x, y, z)$  is the spin direction. By plug in the expression of  $\delta \mathbf{t}$  in Eq. 4.2.11 for index  $i$  and its transpose for index  $j$  to the Eq. 4.1.3, leads to:

$$\begin{aligned} \delta E_{ij} &= (\delta e_i^x, \delta e_i^y, \delta e_i^z) \begin{pmatrix} J_{ij}^{xx} & J_{ij}^{xy} & J_{ij}^{xz} \\ J_{ij}^{yx} & J_{ij}^{yy} & J_{ij}^{yz} \\ J_{ij}^{zx} & J_{ij}^{zy} & J_{ij}^{zz} \end{pmatrix} \begin{pmatrix} \delta e_i^x \\ \delta e_i^y \\ \delta e_i^z \end{pmatrix} \\ &= (\delta e_i^x, \delta e_i^y, \delta e_i^z) \mathcal{J}_{ij} \begin{pmatrix} \delta e_i^x \\ \delta e_i^y \\ \delta e_i^z \end{pmatrix} \end{aligned} \quad (4.2.13)$$

where the  $3 \times 3$  matrix  $\mathcal{J}_{ij}$  is defined as:

$$\{\mathcal{J}_{ij}\}_{\alpha,\beta} = -\frac{1}{\pi} \text{Im} \int dE \text{Tr} \delta t_{=i}^\alpha \underline{\underline{G}}_{ij} \delta t_{=j}^\beta \underline{\underline{G}}_{ji}, \quad (4.2.14)$$

Using equation 4.2.13 one can describe the energy change due to a small variation of the initial magnetization directions  $\hat{e}_i^{(0)}$  and  $\hat{e}_j^{(0)}$ . For instance, if one assumes that  $\hat{e}_i^{(0)} = \hat{e}_j^{(0)} = \hat{z}$ , then one can only determine the xy-subblock of the matrix element of  $\mathcal{J}_{ij}$  as follow:

$$\mathcal{J}_{ij}^{x,y} = \begin{pmatrix} J_{ij}^{xx} & J_{ij}^{xy} \\ J_{ij}^{yx} & J_{ij}^{yy} \\ J_{ij}^{zx} & J_{ij}^{zy} \end{pmatrix}. \quad (4.2.15)$$

Thus, only the z-component of the Dzyaloshinskii-Moriya vector can be determined as given by the expression in Eq. 4.2.6.

### 4.3 Parametrization with induced magnetic atoms

On previous sections, the exchange coupling constants and DM vectors among magnetic atoms have been calculated. However, as the system of interest for this work, Pd/Fe/Ir(111), contains nonmagnetic Pd atoms which exhibit induced magnetic moments when in proximity to magnetic materials, one also needs to take into account their effect in the magnetic interactions. Therefore, this section will deliver a discussion about how the interactions of magnetic Fe atoms with nonmagnetic Pd atoms can be included in the Hamiltonian (see Eq. 4.0.2). A further discussion over the interaction with magnetized Pd atoms will also be given when the presence of impurity atoms on top of the Pd layer is taken into consideration.

#### Renormalization of interactions in the clean limit

For simplicity we will start by studying a clean system in which no impurities are present. By following Ref. [81], the full Heisenberg Hamiltonian including the Fe atoms and the Pd layer can be written as follows:

$$\mathcal{H} = \sum_{ij}^{Fe+Pd} \vec{M}_i \tilde{\mathcal{J}}_{ij} \vec{M}_j. \quad (4.3.1)$$

Here the tensorial exchange coupling,  $\tilde{\mathcal{J}}_{ij}$ , includes the Heisenberg exchange and DM terms, where the indices  $i$  and  $j$  run over the Fe and Pd atoms. One can decompose the sums in the Hamiltonian of Eq. 4.3.1 to include the interaction of the induced moment Pd atoms as follows:

$$\begin{aligned} \mathcal{H} = & \sum_{ij} \vec{M}_i \tilde{\mathcal{J}}_{ij}^{M-M} \vec{M}_j + \sum_{i\alpha} \vec{M}_i \tilde{\mathcal{J}}_{i\alpha}^{M-m} \vec{m}_\alpha \\ & + \sum_{j\beta} \vec{m}_\beta \tilde{\mathcal{J}}_{\beta j}^{m-M} \vec{M}_j + \sum_{\alpha\beta} \vec{m}_\alpha \tilde{\mathcal{J}}_{\alpha\beta}^{m-m} \vec{m}_\beta, \end{aligned} \quad (4.3.2)$$

where the summations over the indices  $i$  and  $j$  run over the Fe atoms whose magnetization are denoted by  $M_i$  and  $M_j$ , whilst the indices  $\alpha, \beta$  run over the Pd atoms where the corresponding magnetization vectors are given by  $\vec{m}_\alpha$  and  $\vec{m}_\beta$ . Here, one can assume that the induced magnetic moments on Pd atoms are governed only by the magnetic moments of the Fe atoms which are nearest neighbours of the Pd atoms. As expressed by:

$$\vec{m}_\alpha = \chi_\alpha \sum_{M_i \in \langle M, \alpha \rangle} \vec{M}_i, \quad (4.3.3)$$

with  $\chi_\alpha$  being the susceptibility. The sum in Eq. 4.3.3 includes only the nearest neighbour Fe atoms. The susceptibility can be then extracted by the following equation when assuming a collinear state

$$\chi_\alpha = \frac{|\vec{m}_\alpha|}{\sum_{M_i \in \langle M, \alpha \rangle} |\vec{M}_i|}. \quad (4.3.4)$$

For a detailed derivation of Eq.4.3.4 one can see the Appendix in Ref. [81].

By substituting the expression for  $\vec{m}_\alpha$  of Eq. 4.3.3 into Eq. 4.3.2, and neglecting the small contribution from the last terms one gets:

$$\mathcal{H} = \sum_{ij} \vec{M}_i \tilde{\mathcal{J}}_{ij}^{M-M} \vec{M}_j + \sum_{i\alpha} \sum_{M_j \in \langle M, \alpha \rangle} \vec{M}_i \tilde{\mathcal{J}}_{i\alpha}^{M-m} \chi_\alpha \vec{M}_j + \sum_{\beta j} \sum_{M_i \in \langle M, \beta \rangle} \tilde{\mathcal{J}}_{\beta j}^{m-M} \chi_\beta \vec{M}_j. \quad (4.3.5)$$

If there are  $N$  nearest neighbour Fe atoms that surround the Pd atom and one assumes that they have the same magnetic moment  $M$ , then the susceptibility in Eq. 4.3.4 can be rewritten as follows:

$$\chi_\alpha = \frac{|\vec{m}_\alpha|}{NM}. \quad (4.3.6)$$

As a final step one can also rearrange the Eq. 4.3.5 in terms of unit vectors of magnetization  $\hat{M}$ , by redefining the expression of  $\tilde{\mathcal{J}}_{ij}$  as follows:

$$\tilde{\mathcal{J}}_{ij} = \frac{\mathcal{J}_{ij}}{\left| \vec{M}_i \right| \left| \vec{M}_j \right|} \quad (4.3.7)$$

with  $\mathcal{J}_{ij}$  is the usual exchange tensor given by:

$$\mathcal{J}_{ij} = \begin{bmatrix} J & D_{ij}^z & -D_{ij}^y \\ -D_{ij}^z & J & D_{ij}^x \\ D_{ij}^y & -D_{ij}^x & J \end{bmatrix}.$$

By plugging the expression of  $\tilde{\mathcal{J}}_{ij}$  in Eq.4.3.7 and the Eq. 4.3.6 into Eq.4.3.5, the final expression for Hamiltonian that includes the interaction with magnetized atoms in a defect-free system is given by:

$$\begin{aligned} \mathcal{H} = & \sum_{ij} \hat{M}_i \mathcal{J}_{ij}^{M-M} \hat{M}_j + \sum_{i\alpha} \sum_{M_j \in \langle M, \alpha \rangle} \hat{M}_i \frac{\mathcal{J}_{i\alpha}^{M-m}}{N} \hat{M}_j \\ & + \sum_{\beta j} \sum_{M_i \in \langle M, \beta \rangle} \hat{M}_i \frac{\mathcal{J}_{\beta j}^{M-m}}{N} \hat{M}_j. \end{aligned} \quad (4.3.8)$$

### Renormalization in the precesence of impurities

Now that one possesses a generalized Heisenberg Hamiltonian (Eq. 4.3.8) which includes the interaction between magnetic and nonmagnetic atoms in or systems such as Pd/Fe/Ir(111) in the clean limit, the influence of defects must now be explored. The decomposition of the full Heisenberg Hamiltonian including Fe, Pd, and the impurity atoms can be written as:

$$\begin{aligned} \mathcal{H} = & \sum_{ij}^{Fe+Pd+Imp} \vec{M}_i \tilde{\mathcal{J}}_{ij} \vec{M}_j \\ = & \sum_{ij} \vec{M}_i \tilde{\mathcal{J}}_{ij}^{M-M} \vec{M}_j + \sum_{i\alpha} \vec{M}_i \tilde{\mathcal{J}}_{i\alpha}^{M-m} \vec{m}_\alpha + \sum_{j\beta} \vec{m}_\beta \tilde{\mathcal{J}}_{\beta j}^{m-M} \vec{M}_j \\ & + \sum_{\alpha\beta} \vec{m}_\alpha \tilde{\mathcal{J}}_{\alpha\beta}^{m-m} \vec{m}_\beta + \sum_{M_i \in \langle M, imp \rangle} \vec{M}_i \tilde{\mathcal{J}}_{i imp}^{M-imp} \vec{M}_{imp} + \sum_{M_j \in \langle M, imp \rangle} \vec{M}_{imp} \tilde{\mathcal{J}}_{i imp}^{imp-M} \vec{M}_j \\ & + \sum_{M_\alpha \in \langle M, imp \rangle} \vec{m}_\alpha \tilde{\mathcal{J}}_{\alpha imp}^{M-imp} \vec{M}_{imp} + \sum_{M_\beta \in \langle M, imp \rangle} \vec{M}_{imp} \tilde{\mathcal{J}}_{imp \beta}^{imp-m} \vec{m}_\beta, \end{aligned} \quad (4.3.9)$$

where the summation with indices  $i$  and  $j$  runs over the Fe atoms, the indices  $\alpha, \beta$  run over the Pd atoms and the summations with the impurity are performed only for the nearest neighbours. As in the case of defect-free system, the Pd magnetic moments are governed by their nearest neighbour Fe atoms. However, in the presence of defects, the magnetic moment of the Pd atoms which are close to the impurities are also affected by it. Therefore, the magnetization of the Pd atoms,  $\vec{m}_\alpha$ , is coupled

with the magnetization of the Fe atoms,  $\vec{M}_i$ , via the susceptibility presented in the following way:

$$\vec{m}_\alpha = \mathcal{X}_\alpha \sum_i \vec{M}_i = \mathcal{X}_{Fe} \sum_{M_i \in \langle M, \alpha \rangle} \vec{M}_i^{Fe} + \mathcal{X}_{imp} \vec{M}_{imp} \delta_{imp, \alpha}, \quad (4.3.10)$$

where  $\vec{M}_{imp}$  and  $\mathcal{X}_{imp}$  are the magnetization and susceptibility of the impurity atoms, and the summation is performed over the nearest neighbors. Using the collinear magnetic state the susceptibility of the Fe atoms can be written as follows:

$$\mathcal{X}_{Fe} = \frac{|\vec{m}_\alpha^0|}{\sum_{M_i \in \langle M, \alpha \rangle} |\vec{M}_i^0|} = \frac{|\vec{m}_\alpha^0|}{N |\vec{M}^0|} = \frac{m_\alpha^0}{NM^0}, \quad (4.3.11)$$

where  $N$  is the number of nearest neighbour Fe atoms to the Pd atom,  $m_\alpha^0$  and  $M^0$  are the magnetic moments for the Pd and Fe atoms in the clean system, respectively. On the other hand, from Eq. 4.3.10 the susceptibility of the impurity atoms can be written as:

$$\mathcal{X}_{imp} = \frac{|\vec{m}_\alpha - \mathcal{X}_{Fe} \sum_{i \in NN_\alpha} \vec{M}_i|}{|\vec{M}_{imp}|} = \frac{|\vec{m}'|}{|\vec{M}|_{imp}} = \frac{m'}{M_{imp}} \quad (4.3.12)$$

By substituting the expression for  $\mathcal{X}_{Fe}$ ,  $\mathcal{X}_{imp}$  into Eq. 4.3.9 and using Eq. 4.3.7, one can get the expression for a Hamiltonian which includes the interaction between magnetic and nonmagnetic atoms in the system in the presence of an impurity as:

$$\begin{aligned} \mathcal{H} = & \sum_{ij} \hat{M}_i^{Fe} \mathcal{J}_{ij}^{M-M} \hat{M}_j^{Fe} + \sum_i \hat{M}_i^{Fe} \mathcal{J}_{i imp}^{M-imp} \hat{M}_{imp} + \sum_j \hat{M}_{imp} \mathcal{J}_{imp j}^{imp-M} \hat{M}_j^{Fe} \\ & + \sum_i \sum_{\substack{M_\alpha \in \langle M, i \rangle \\ M_j \in \langle M, \alpha \rangle}} \hat{M}_i^{Fe} \frac{m_\alpha^0}{m_\alpha} \frac{\mathcal{J}_{i\alpha}^{M-m}}{N} \frac{M_j^{Fe}}{M^0} \hat{M}_j^{Fe} + \sum_j \sum_{\substack{M_\beta \in \langle M, j \rangle \\ M_i \in \langle M, \beta \rangle}} \hat{M}_i^{Fe} \frac{m_\beta^0}{m_\beta} \frac{\mathcal{J}_{i\beta}^{m-M}}{N} \frac{M_j^{Fe}}{M^0} \hat{M}_j^{Fe} \\ & + \sum_i \sum_{M_\alpha \in \langle M, i \rangle} \hat{M}_i^{Fe} \frac{m'}{m_\alpha} \mathcal{J}_{i\alpha}^{m-M} \hat{M}_{imp} \delta_{imp, NN_\alpha} + \sum_j \sum_{M_\beta \in \langle M, j \rangle} \hat{M}_{imp} \frac{m'}{m_\beta} \mathcal{J}_{i\beta}^{M-m} \hat{M}_j \delta_{imp, NN_\beta} \\ & + \sum_{\substack{M_\alpha \in \langle M, imp \rangle \\ M_i \in \langle M, \alpha \rangle}} \hat{M}_i^{Fe} \frac{m_\beta^0}{m_\alpha} \frac{M_i^{Fe}}{M^0} \frac{\mathcal{J}_{\alpha imp}^{m-imp}}{N} \hat{M}_{imp} + \sum_{\substack{M_\beta \in \langle M, imp \rangle \\ M_j \in \langle M, \beta \rangle}} \hat{M}_{imp} \frac{m_\beta^0}{m_\beta} \frac{M_j^{Fe}}{M^0} \frac{\mathcal{J}_{imp \beta}^{imp-m}}{N} \hat{M}_j^{Fe}. \end{aligned} \quad (4.3.13)$$

# Chapter 5

## Magnetization Dynamics

In the previous chapter, the methodology to extract from first principles the interactions used to model magnetic skyrmions was introduced. By making use of the obtained parameters, one can determine the static and dynamical properties of these magnetic textures and their interactions with defects. The description of the dynamics and stability will be explored via the Landau-Lifshitz-Gilbert (LLG) equation [42]. In this chapter, the phenomenological LLG equation will be introduced. Afterwards, its expansion into the atomistic regime will be discussed.

### 5.1 Landau-Lifshitz-Gilbert equation

To be able to describe the dynamics of the magnetization in a magnetic material, it is necessary to find the equation of motion of the magnetic moments that compose it. To derive this expression, one can start by considering the classical picture, that is a magnetic material with magnetization,  $\vec{M}$ , under the influence of an external magnetic field,  $\vec{B}_{\text{ext}}$ .

If one places the magnetization out of equilibrium and rotates it away from the direction of the field, it will experience a torque,  $\vec{\tau} = \vec{M} \times \vec{B}_{\text{ext}}$ , which forces it to precess around the direction of  $\vec{B}_{\text{ext}}$ . Thus, one can write the time evolution of the angular momentum,  $\vec{L}$ , of the system:

$$\frac{\partial \vec{L}}{\partial t} = \vec{M} \times \vec{B}_{\text{ext}}. \quad (5.1.1)$$

It is possible to relate the angular momentum with the magnetization via the relation,  $\vec{M} = -\gamma \vec{L}$ :

$$\frac{\partial \vec{M}}{\partial t} = -\gamma \vec{M} \times \vec{B}_{\text{ext}}, \quad (5.1.2)$$

where  $\gamma$  is the gyromagnetic ratio. One can also write the expression in Eq. 5.1.2 in the terms of an effective field,  $\vec{B}_{\text{eff}}$ , that takes into account not only the external field but also the effect of interactions in the material which can affect the dynamics of the system. In terms of  $\vec{B}_{\text{eff}}$  the equation of motion can be rewritten as follows:

$$\frac{\partial \vec{M}}{\partial t} = -\gamma \vec{M} \times \vec{B}_{\text{eff}}. \quad (5.1.3)$$

Eq. 5.1.3 shows the precession of the magnetization at constant energy. The magnetic moment precess indefinitely around the direction of the magnetic field without ever aligning itself with it, as schematically shown in figure 5.1a. This is an incomplete picture as one can not neglect the dissipative factors present in real materials. These dissipation processes affect the magnetization dynamics, such that the system will relax and reach the equilibrium point with the minimum energy, that is the magnetization aligns with the magnetic field, as shown in figure 5.1b. Thus, to describe such effects, Landau and Lifshitz [63] proposed a phenomenological damping term, which is added to the precession term:

$$\frac{\partial \vec{M}}{\partial t} = -\gamma \vec{M} \times \vec{B}_{\text{eff}} - \frac{\lambda}{M_s} \vec{M} \times \left[ \vec{M} \times \vec{B}_{\text{eff}} \right], \quad (5.1.4)$$

where  $M_s$  is the saturation magnetization of the system and  $\lambda$  is a phenomenological damping parameter which is defined positive. In Eq. 5.1.4 one sees an additional term, which is dubbed the damping term,  $\vec{M} \times \left[ \vec{M} \times \vec{B}_{\text{eff}} \right]$ , that is perpendicular to the direction of the precession of the magnetization. It tends to align the magnetization towards the direction of the effective field.

In the low damping limit, the Landau-Lifshitz equation can be used to describe the time evolution of the magnetization in an accurate manner. However, it fails to describe materials with large damping values. In the limit of infinite damping, i.e.  $\lambda \rightarrow \infty$ , the Landau-Lifshitz equation predicts  $\frac{\partial \vec{M}}{\partial t} \rightarrow \infty$  [54, 71]. This is un-physical, as it would imply an infinitely fast motion of the magnetization. Such concerns led Gilbert [42] to propose an alternative damping term, obtained by considering a dissipative term in the magnetic Lagrangian which results in the equation of motion of the magnetization given by:

$$\frac{\partial \vec{M}}{\partial t} = -\gamma \vec{M} \times \vec{B}_{\text{eff}} + \frac{\alpha}{M_s} \vec{M} \times \frac{\partial \vec{M}}{\partial t}, \quad (5.1.5)$$

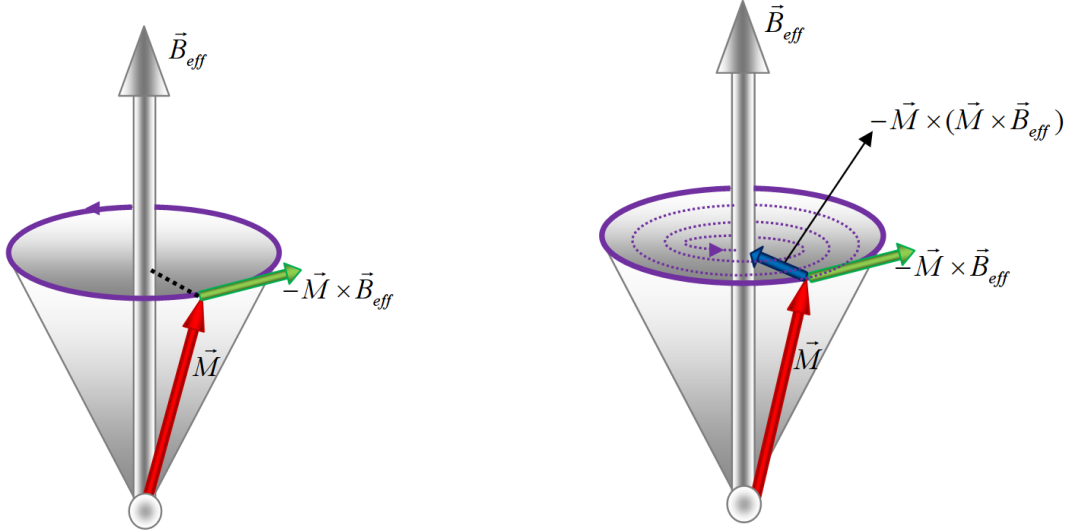
with  $\alpha$  being the damping parameter, named after Gilbert. This expression is called the Landau-Lifshitz-Gilbert (LLG) equation.

It can be shown that in case of isotropic damping both Eq. 5.1.4 and Eq. 5.1.5 are equivalent if one renormalizes the gyromagnetic ratio,  $\gamma$ , and the phenomenological damping,  $\lambda$  (see A.1). Thus, one can rewrite the expression of LLG equation in the representation of Landau-Lifshitz equation as:

$$\frac{\partial \vec{M}}{\partial t} = -\gamma_L \vec{M} \times \vec{B}_{\text{eff}} - \gamma_L \frac{\alpha}{M_s} \vec{M} \times \left( \vec{M} \times \vec{B}_{\text{eff}} \right), \quad (5.1.6)$$

with  $\gamma_L = \frac{\gamma}{(1+\alpha^2)}$ . If one considers the high damping limit, i.e.  $\alpha \rightarrow \infty$ , it can be seen that  $\frac{\partial \vec{M}}{\partial t} = 0$ . One can see here that the Gilbert damping has the same properties as the damping terms in classical mechanics, in which the magnetization motion slows down by increasing damping parameter.

Usually, the dynamics of magnetic systems is described in the micromagnetic limit where the magnetization is considered to be a continuous vector field. This approach is very successful to describe the dynamics of large magnetic textures. However, to explain the magnetization dynamics in the atomic limit, another approach is needed to properly describe the time evolution of these systems [2].



(a) Larmor Precession

(b) A damping factor is included in the motion

Figure 5.1: The motion of magnetic moment in a presence of magnetic field (a) show the precession of a magnetic moment (red) around an effective magnetic field (grey) (b) show precession (green) with damping vector (blue) of the magnetization motion

## 5.2 Atomistic spin dynamics

As mentioned in the previous section, if one wishes to describe the dynamics of ultra-narrow magnetic textures one must go towards an atomistic treatment of the magnetic material. Thus, it is of great importance to ascertain if the LLG equation is valid at these length scales. The seminal work in this aspect was performed by Antopov et al. [2], in which starting from the local spin density approximation (LSDA) Hamiltonian, an atomistic formulation of the LLG equation was found. Following this work, one can obtain the LLG equation by starting from the time dependent Kohn-Sham equations:

$$\left( -\nabla^2 + V_0(\vec{r}, t) + \left( \vec{\sigma} \cdot \vec{B}_{\text{eff}}(\vec{r}, t) \right) \right) \varphi_i(\vec{r}, t) = \epsilon_i \varphi_i(\vec{r}, t), \quad (5.2.1)$$

where the term  $\nabla^2$  describes the single-particle kinetic energy associated with the Kohn-Sham eigenstates,  $\varphi_i$ , which correspond to the energy  $\epsilon_i$ . With  $V_0(\vec{r}, t)$  being the scalar potential which describes the effective single particle system and  $\vec{\sigma} \cdot \vec{B}_{\text{eff}}(\vec{r}, t)$  is the magnetic contribution to the potential.

The equation of motion of a single atomic magnetic moment was then derived from the time evolution of the spin density,  $\vec{S}(\vec{r}, t) = \varphi^\dagger(\vec{r}, t) \hat{S} \varphi(\vec{r}, t)$ , where  $\hat{S}$  is the spin operator (for a detailed derivation see Ref. [33, 2]) and it is given by:

$$\frac{\partial \vec{S}(\vec{r}, t)}{\partial t} = -\nabla \cdot \vec{Q}_{\text{KS}}(\vec{r}, t) - \gamma \vec{S}(\vec{r}, t) \times \vec{B}_{\text{eff}}, \quad (5.2.2)$$

where  $\vec{Q}_{\text{KS}}$  represents the spin current density and it is defined as:

$$\vec{Q}_{\text{KS}} = \frac{1}{2i} \left[ \left( \hat{S} \nabla \varphi^\dagger(\vec{r}, t) \right) \varphi(\vec{r}, t) - \varphi^\dagger(\vec{r}, t) \hat{S} \varphi(\vec{r}, t) \right]. \quad (5.2.3)$$

Solving the time-dependent KS equation is a very complex and expensive endeavor. Hence, to overcome these difficulties, certain approximations must be employed, chief among them being *the adiabatic approximation*. Under it, one can separate the fast variables (electronic degrees of freedom) from the slow variables (motion of the local magnetic moments). This is akin to the Born-Oppenheimer approximation, which is a type of adiabatic approximation, used to separate the electronic and ionic degrees of freedom in electronic structure calculations. Such considerations are possible, due to the different energy range of these two variables, whilst the transverse excitations of the magnetic moments are in the order of meV, the characteristic energies of the electronic processes are in the order of eV. This approximation then allows us to transform the time-dependent Kohn-Sham equation into its time-independent counterpart for a fixed direction of the magnetization. The charge density,  $n(\vec{r})$ , is then represented as a potential for the effective magnetic field that will perform a torque on the magnetization [2]. One can then subdivide the sample into spheres and by integrating the spin density of the magnetic atom on site  $i$  over this sphere, one can obtain the atomic magnetic moment. Based on this approximation one can replace  $\vec{S}(\vec{r}, t) \rightarrow m_i(t)$  [33]. Employing these approximations and neglecting the spin current term,  $\vec{Q}_{\text{KS}}$ , one can rewrite the expression in Eq. 5.2.2 as follows:

$$\frac{d\vec{m}_i}{dt} = -\gamma \vec{m}_i \times \vec{B}_{\text{eff}}^i(t). \quad (5.2.4)$$

This equation of motion (Eq. 5.2.4) has the same form as the precession term in the LLG but now relating the time evolution of an atomic magnetic moment, to the effective field stemming from the electronic interactions on a given atom.

The inclusion of the damping term from first principles is also possible when starting from a single electron picture. Therefore, the dissipative processes inherent to the dynamics of magnetic systems can be taken into account in the atomistic equation of motion by including the Gilbert damping parameter. Thus, the equation of motion can be written in the following way [90, 33]:

$$\frac{d\vec{m}_i}{dt} = -\frac{\gamma}{(1 + \alpha_i^2)} \left( \vec{m}_i \times \vec{B}_{\text{eff}}^i + \frac{\alpha_i}{m_i} \vec{m}_i \times \left[ \vec{m}_i \times \vec{B}_{\text{eff}}^i \right] \right), \quad (5.2.5)$$

where  $\alpha_i$  is the Gilbert damping,  $\vec{m}_i$  is the atomic magnetic moment on site  $i$  and  $\vec{B}_{\text{eff}}^i$  is the effective field acting on the magnetic moment.

As seen in Eq. 5.2.5, knowing the effective field is determinant to describe the magnetization dynamics. In principle, the determination of this field would require the calculation of the exchange-correlation field from the electronic structure for a given direction of the magnetic moment, that is for every time  $t$  of the dynamics. However, this is prohibitively expensive, thus another approach is required. One approach to obtain this magnetic field, is by mapping this field to an effective Heisenberg Hamiltonian parametrized from first principles calculations, by making use of

the relation  $\vec{B}_{\text{eff}}^i = \frac{\partial \mathcal{H}_{\text{Heis}}}{\partial \vec{m}_i}$ , with  $\mathcal{H}_{\text{Heis}}$  being the extended Heisenberg Hamiltonian as defined in chapter 4 (Eq. 4.0.2).

The use of the equation of motion in an atomistic level also allows the proper introduction of thermal effects in the magnetization dynamics [40]. The consideration to include this temperature effects in the equation of motion is really important as at a finite value it can cause thermodynamic fluctuations of the spin moments [33, 35]. By taking into account this thermal fluctuations effect one can have a better observations to describe the magnetization dynamics of the spin moments. In the Langevin dynamics approach, the temperature effects on the magnetization are modelled by introducing a fluctuation terms in the LLG equation [17, 62]. The effective field is then redefined such that  $\vec{B}_{\text{eff}}^i = \vec{B}_{\text{Heis}}^i + \vec{b}(T)$ , where  $\vec{B}_{\text{Heis}}^i$  is the effective field arising from Heisenberg Hamiltonian and  $\vec{b}(T)$  is the stochastic field. Thus allowing one to write:

$$\frac{d\vec{m}_i}{dt} = -\frac{\gamma}{(1 + \alpha^2)} \left( \vec{m}_i \times \left( \vec{B}_{\text{eff}}^i + \vec{b}(T) \right) + \frac{\alpha_i}{m_i} \vec{m}_i \times \left[ \vec{m}_i \times \left( \vec{B}_{\text{eff}}^i + \vec{b}(T) \right) \right] \right). \quad (5.2.6)$$

The equation of motion in Eq. 5.2.6 shows the magnetization dynamics due to the interaction between the magnetic moment with the stochastic field is both included in the precession and the damping term. The stochastic fields are modelled using Gaussian white noise and satisfy the following criteria:

$$\langle b(t) \rangle = 0, \quad (5.2.7)$$

$$\langle b_i(t) b_j(t') \rangle = 2D \delta_{ij} \delta(t - t'), \quad (5.2.8)$$

$$D = \frac{\alpha}{1 + \alpha^2} \frac{k_B T}{\mu_B m}, \quad (5.2.9)$$

where  $\langle \dots \rangle$  denotes the time average. The first consideration (Eq. 5.2.7) shows that the time average of the stochastic field is zero, whilst Eq. 5.2.8 shows that the field at site  $i$  is uncorrelated in time (denoted by  $\delta(t - t')$ ) and in space (denoted by  $\delta_{ij}$ ). Lastly, it can be found that the strength of the stochastic field,  $D$ , is related to the temperature,  $T$ , and can be obtained from the Fokker-Planck equation in conjunction with the fluctuation-dissipation theorem [90, 33].

In this thesis, atomistic spin dynamics will be used to analyze the skyrmion-defects interaction. As this method simulates every atom as a single magnetic moment, the atomic scale variations of the magnetization due to the local interactions can be described more accurately [35, 90]. Therefore, small non-trivial magnetic structures like skyrmions interacting with some impurities can be treated efficiently using this approach. The parameters that will be used in the atomistic spin dynamics simulations such as spin moments, exchange interactions, DM vectors and magnetic anisotropy constant are calculated from DFT calculations.

# Chapter 6

## Results

### 6.1 Overview of the System

The main focus of this thesis is to study the skyrmion-defect interaction for realistic systems. Attempts to study the effect of impurities over the dynamics and the stability of skyrmions are usually done via effective models, where several approximations to the type of interactions and the skyrmion profile must be performed. It is only recently that material specific studies have been performed [67]. As in the work by Lima Fernandes et al., the system chosen to study these interactions is the FCC Pd/Fe/Ir(111). Due to the strong spin-orbit coupling of the heavy metal substrate, Ir(111), and the broken inversion symmetry at the interface, this system exhibits a large interfacial Dzyaloshinskii-Moriya interaction (DMI) [75, 38]. This large DMI in combination with the exchange frustration, results in a material which can host nanosized magnetic Néel skyrmions [24, 82, 67, 89]. Even more, some pioneering work on the interaction between defects and skyrmions has been done both experimentally [32] and theoretically [67] in this material. Hence, making it an ideal playground to study more complex types of impurities and their effect on skyrmions.

Here a further discussion concerning the interaction between a magnetic skyrmion and defects will be addressed from first principles calculations combined with atomistic spin dynamics simulations. Due to the small size of the studied skyrmions, an atomistic study is necessary to determine the impact of various defects on their stability and dynamical behaviors. The investigated defects consist of  $3d$  transition metal elements (Cr, Fe, and Co). The effect of the dimensionality and geometry of the defects will also be studied, by considering several cluster configurations such as adatom, dimer, trimer, and line defects. Also, the effect of the position of the defects will be studied by placing the defects on top of the Pd layer in FCC and HCP stacking sites. These configurations can be schematically seen in Fig. 6.1, where in the HCP stacking the impurities will be directly underneath the Fe atom, whereas in the FCC stacking they are aligned with the Ir atoms.

The skyrmion-defect interaction was investigated via atomistic spin dynamics (see Chapter 5) making use of the parameters obtained from the first-principles calculations. In this approach an impurity cluster is embedded in a host system, where the parameters of the impurity area are given by the parameters of a first-principles impurity calculation (Chapter 3), whilst the parameters of the host system correspond to those of the clean system. The total energy of the system is first cal-

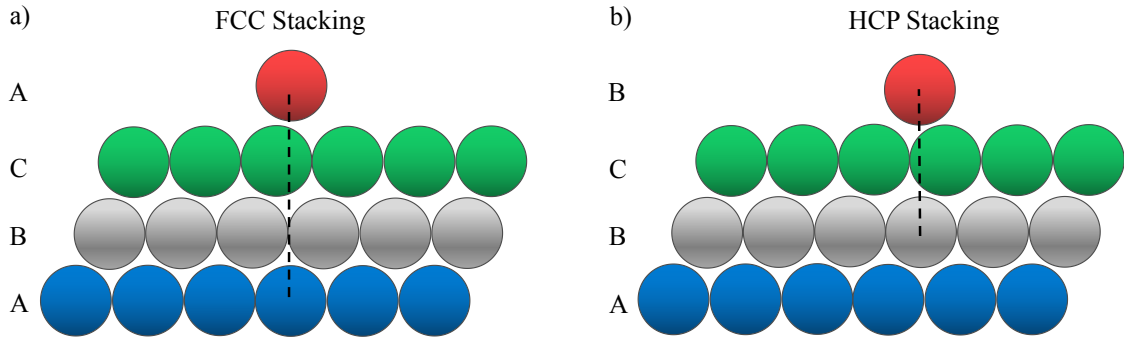


Figure 6.1: Schematic representation of the (a) FCC and (b) HCP stacking configuration for system fcc Pd/Fe/Ir(111) with an impurity adatom (red sphere) deposited on the top on Pd layer. The green, grey, and blue spheres represent the Pd, Fe, and Ir layer, respectively.

culated for a reference point located faraway from the impurity region. At this point a magnetic skyrmion is stated at the clean system with a ferromagnetic background. Another set of calculations are performed where the skyrmion core is imposed at each of the Fe atoms present in the impurity region, thus allowing us to track the energy of the system when a skyrmions is considered at each of those positions. By taking the difference between the energies inside the cluster and the reference point, one is then able to find the **energy profile** of the skyrmion-defect interaction. A negative and positive energy difference on the energy profile indicate an attractive and repulsive skyrmion-defect interaction, respectively.

In the following section, we begin the discussion by analyzing the impact of the present defects on the magnetic properties of the system. It is then followed by investigating the effects these changes have on the interaction between the impurities with a single magnetic skyrmion. For simplicity we begin by looking at the adatom case that has been already studied [67].

## 6.2 Results and discussion

To better understand the effect of defects in the magnetic properties of Pd/Fe/Ir(111), it is convenient to encapsulate some of its key properties. One of the most relevant parameters is the isotropic exchange interaction, which has a magnitude of 19.8 meV among the nearest neighbor Fe atoms, which is in good agreement with previously obtained results in Ref. [24, 67, 89]. The given exchange coupling here is the effective renormalization value which was calculated by taking into consideration the interaction with the induced magnetic moment of the non-magnetic Pd atoms in the system as discussed in chapter 4. This renormalization scheme is also used to calculate the effective DMI vector, however, its value change only a little from the initial values. We also use the same renormalization procedure to calculate the effective value of the exchange coupling for the case with the presence of defect atoms in all the studied system configurations.

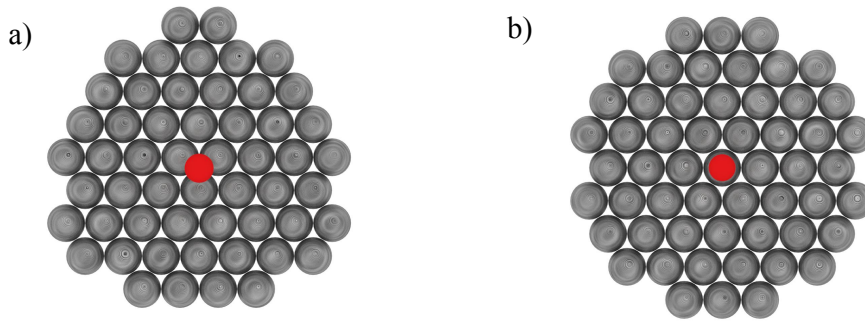


Figure 6.2: Schematic representation of the two studied configurations in the adatom system namely a) FCC and b) HCP. Fe atoms are represented by the grey spheres, and the red one indicates the impurity adatom.

### 6.2.1 Adatom

The real space clusters used in the calculations for the FCC and HCP stacking configurations are presented in figure 6.2. The top view only showcases the impurity and the layer of Fe atoms which are denoted by the red and grey spheres, respectively. Due to its different position in each configuration, the adatom has different nearest neighbor atoms in the Fe substrate. Both configurations have different coordination numbers with 3 Fe atoms as the first nearest neighbor atoms of the impurity for the FCC stacking, while in the HCP stacking there is one Fe atom sitting directly below the impurity adatom and surrounded by 6 Fe atoms as the next nearest neighbor atoms.

Firstly, one can look at the magnitude of the magnetic moments of the studied impurities. In the FCC stacking, among the studied elements the Cr adatom has the largest magnetic moment,  $3.73 \mu_B$ , followed by Fe,  $3.38 \mu_B$ , and lastly by Co,  $2.15 \mu_B$ . These results are in good agreement with the obtained results in Ref. [67]. On the other hand, in the HCP stacking all the elements have smaller magnetic moments than in the FCC stacking, with Cr having a moment of  $3.68 \mu_B$ ,  $3.36 \mu_B$  for Fe, and  $2.13 \mu_B$  for Co. The obtained spin moments of each elements impurity in both stackings also have a good agreement with their atomic spin moment values namely  $5.0 \mu_B$ ,  $4.0 \mu_B$ , and  $3.0 \mu_B$  for the Cr, Fe, and Co adatom, respectively [9].

For the present impurities, we found for both stackings a ferromagnetic ground state for the Co and Fe adatoms with respect to the Fe layer while Cr adatom couples anti-ferromagnetically to the Fe-substrate. These results agree with previous findings that have studied the energetics of  $3d$  adatoms with different systems such as Fe(001) [78] and Ni(001) [70]. The magnetic coupling between the defects and the Fe-layer can be analyzed by looking at the local density of state (LDOS) for each impurity (see Fig. 6.3). As all impurities are magnetic and exhibit sizable moments, we can see a large splitting of their local density of state for up and down spins. In the FCC stacking shown on the top panel of Fig. 6.3, we see that the majority-spin LDOS of Fe and Co impurities are essentially filled. As expected from the ground state behavior, both Co and Fe adatoms shows a similar spin state configuration with the peak of the majority spin state lying below the Fermi energy while the minority peak lies at the Fermi level. On the other hand, since the Cr adatom

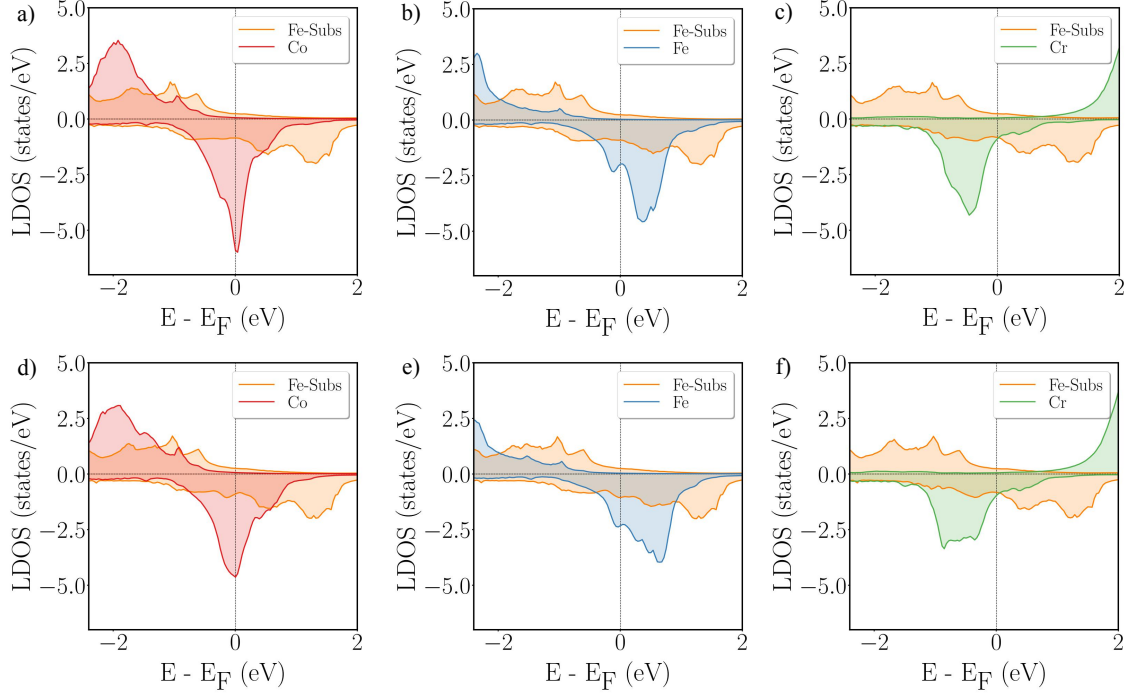


Figure 6.3: Comparison of the local density of states (LDOS) of  $3d$  adatoms with the one of the closest Fe atoms in (a-c) FCC and (d-f) HCP stacking. Positive and negative DOS-values correspond to up and down-states, respectively. The atomic-like peak on the minority spin state for each impurity elements shows the low hybridization occurring between them and the Fe atoms in the substrate due to a far location of the impurities.

couples anti-ferromagnetically to the substrate a different trend is shown. As can be seen in figure 6.3(c) the Cr minority-spin state is unoccupied (green line) and weakly hybridizes with majority-spin band of Fe (orange line) while the Cr majority-spin is almost fully occupied and lies below the Fermi level. As the Fe-substrate is far away from the adatom position, their hybridization is weak leading to the adatoms peaks being atomic like. In the HCP stacking, we can see the same trend as in the FCC stacking. However, since the adatom is located on the top of the Fe atom, the coordination number of impurity in the HCP stacking is lower than in the FCC stacking. Thus, there is a broadening on their majority and minority spin states which leads to a lower spin moment for the adatoms.

As the adatom is located far from the Fe layer, the impact on the magnetic properties of Fe-substrate atoms is also quite localized. In general for both FCC and HCP stackings, the spin moment of the Fe atoms close to the defect are decreased up to 4% from the original value in the clean system. This local effect between the defect and the Fe layer can also be seen on their exchange interactions displayed in Fig. 6.4. As can be seen, in the HCP stacking the defect-substrate exchange coupling for all impurity elements is smaller than in the FCC stacking. The impurity-substrate interaction for the Co and Cr adatoms in the FCC stacking being considerably decreases when moving from the nearest neighbour to the next-nearest neighbour. For the Co adatom in the FCC stacking, the same ferromagnetic coupling is shown for its interaction with the first and second nearest-neighbor atoms on the Fe-substrate,

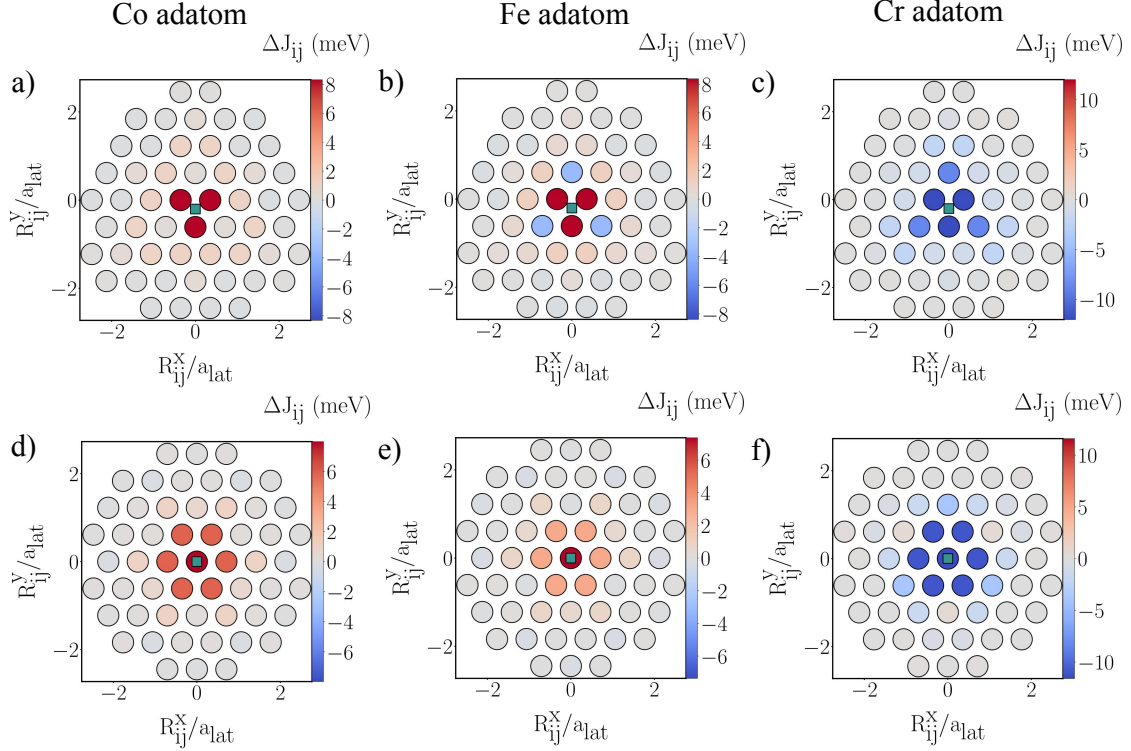


Figure 6.4: The exchange interaction between the adatom (green square) with the Fe atoms in the substrate. The positive (red) and negative (blue) indicate the ferromagnetic (FM) and antiferromagnetic (AFM) coupling. The figures at the top and bottom panel present the interaction in the FCC and HCP stacking, respectively. Figure (a, d) showcases the interaction with Co, (b, e) with Fe, and (c, f) with Cr. The exchange interaction in each figure is presented with different scale on the colorbar.

whilst the Cr shows the same antiferromagnetic coupling with its first and second nearest-neighbor Fe atoms. However, unlike the Co and Cr adatoms, the Fe impurity shows an oscillatory interaction behaviour for its interaction with the nearest neighboring atoms in the substrate. One can also see in table 6.1 the average of the exchange interaction among one Fe atom close to the impurity and its first-nearest neighbors,  $\langle J_{\text{Fe-Fe}} \rangle_{\text{1NN}}$ , average of the modulus of the DM vector,  $\langle |D_{\text{Fe-Fe}}| \rangle_{\text{1NN}}$ , and the magnetic anisotropy energy ( $K_{\text{imp}}$ ) of the  $3d$  adatoms. The obtained values of the MAE for the impurities are in general in the same order of magnitude than the one obtained for the clean system,  $K_{\text{subs}} = -0.6$  meV, where the negative sign indicates a preferred out-of plane orientation of the magnetic moment.

In order to calculate the total energy difference, we first determined the most stable magnetic configuration for the impurity when interacting with the ferromagnetic Fe substrate. For the ground state solution, we found a ferromagnetic alignment with the Fe substrate for the Co and Fe adatoms and an antiferromagnetic coupling for the Cr defect. By using this initial magnetic configuration, we calculated the total energy with an applied external magnetic field  $H = 10$  T at  $T = 0$  K when the skyrmion is imposed at the reference point and inside the impurity cluster. In this case we choose the value of  $H = 10$  T to stabilize a single skyrmion state in our systems since it is in the previously predicted range where single skyrmions are

Table 6.1: Exchange interaction among the adatom and the first-nearest neighbors Fe atoms ( $J_{\text{Imp-Fe}}$ ), average value of exchange interaction for the Fe substrate ( $\langle J_{\text{Fe-Fe}} \rangle_{1\text{NN}}$ ), modulus of the DM vectors between the central Fe atom and its first-nearest neighbor atoms ( $\langle |D_{\text{Fe-Fe}}| \rangle_{1\text{NN}}$ ) and the magnetic anisotropy energy of the adatom ( $K^{\text{imp}}$ ). All the quantities presented are in unit of meV.

Stacking	Element	$\langle J_{\text{Imp-Fe}} \rangle_{1\text{NN}}$	$\langle J_{\text{Fe-Fe}} \rangle_{1\text{NN}}$	$\langle  D_{\text{Fe-Fe}}  \rangle_{1\text{NN}}$	$K^{\text{imp}}$
FCC	Cr	-12.0	16.1	1.19	0.9
	Fe	8.4	15.6	1.27	0.7
	Co	8.3	16.6	1.27	-0.4
HCP	Cr	-11.6	15.3	1.20	-0.1
	Fe	7.3	13.9	1.32	1.2
	Co	7.9	15.3	1.33	0.9

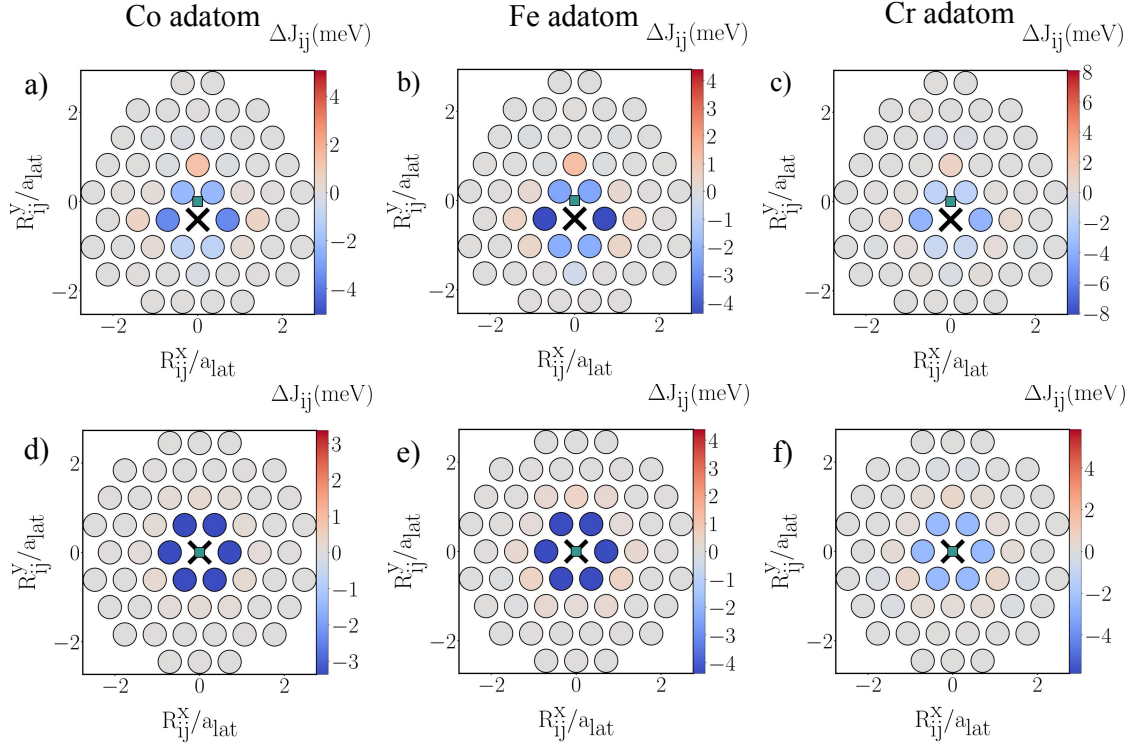


Figure 6.5: The variation of exchange interaction,  $\Delta J_{ij}$ , between one Fe atom in the substrate (cross sign) with its first nearest neighbor atoms induced by the present of adatom (green square).  $\Delta J_{ij}$  is calculated by subtracting the exchange interaction with the present of impurity with the one from clean system,  $\Delta J_{ij} = J_{ij}^{\text{imp}} - J_{ij}^{\text{clean}}$ . The figures at the top and bottom panel present the interaction in the FCC and HCP stacking, respectively. Each figure showcases the interaction with different element namely with (a, d) Co, (b, e) Fe, and (c, f) Cr.

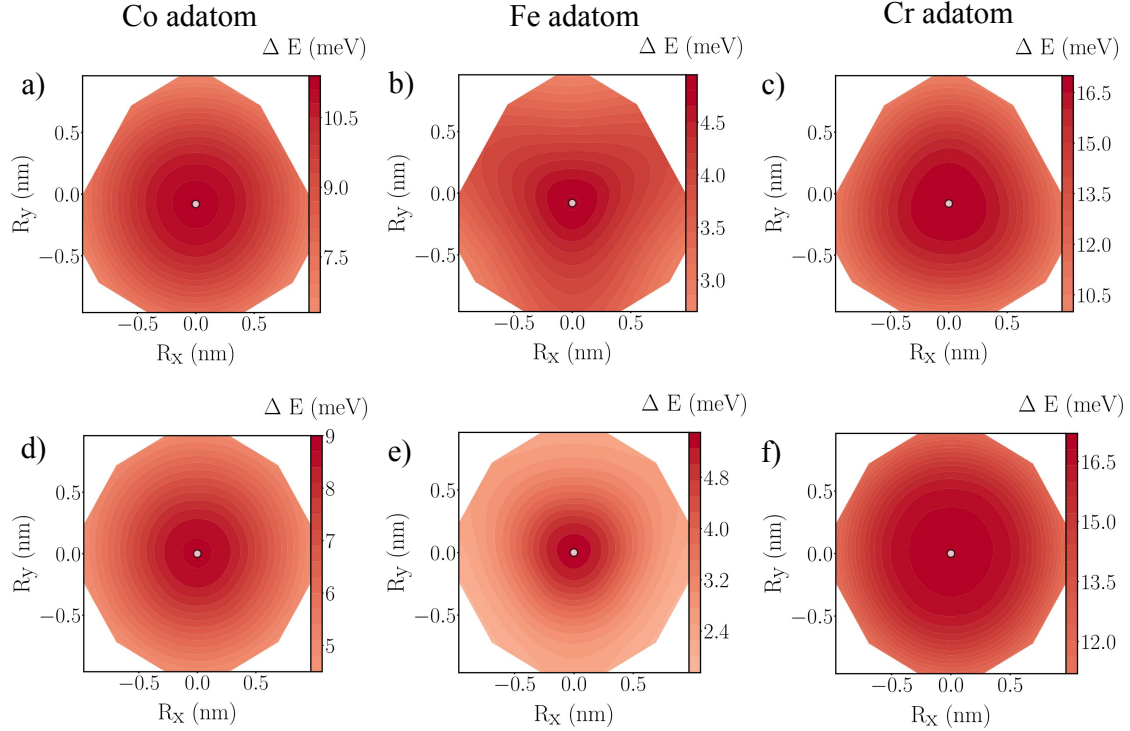


Figure 6.6: The energy profile of skyrmion interacting with adatom. The figures at the top and bottom panel present the interaction in the FCC and HCP stacking, respectively. Figure (a, d) showcases the interaction with Co, (b, e) with Fe, and (c, f) with Cr. The white dot in the figure represents the position of defect and the positive value on the total energy difference in the profile indicates a repulsive skyrmion-defect interaction

found to be stable [24].

The obtained energy profiles are shown in Fig. 6.6. As one can see, regardless of their stackings all studied adatoms show a repulsive behavior. The profiles for the skyrmion-defect interaction show a good agreement with the obtained results in previous studies [67]. However, the strength of the repulsive behavior in our investigations are smaller due to a different method and profile of the studied skyrmion. The repulsive profile shown by the skyrmion-defect interaction indicates that it costs more energy to have a skyrmion inside the impurity cluster compared to the energy required at the reference point (outside the cluster region/clean system). It is important to notice that each element gives a different repulsion strength on the interaction with a magnetic skyrmion. One can also see that there is a slightly different total energy difference between the FCC and HCP stackings. This is due to a different position of adatom in each stacking which leads to a different impurity-substrate exchange interaction as well as a different reduction induced on the exchange interaction among the Fe-substrate as presented in table 6.1. The position of the adatom in both stacking configurations also impacts the magnetic configuration of the impurity when interacting with the skyrmion (see Fig. 6.7). In both stacking the adatom wants to align collinearly with the substrate so it follows the local direction of the spin moment of Fe atoms. In the HCP stacking, due to its location on top of the Fe atom, the adatom can easily align with the direction of the spin moment

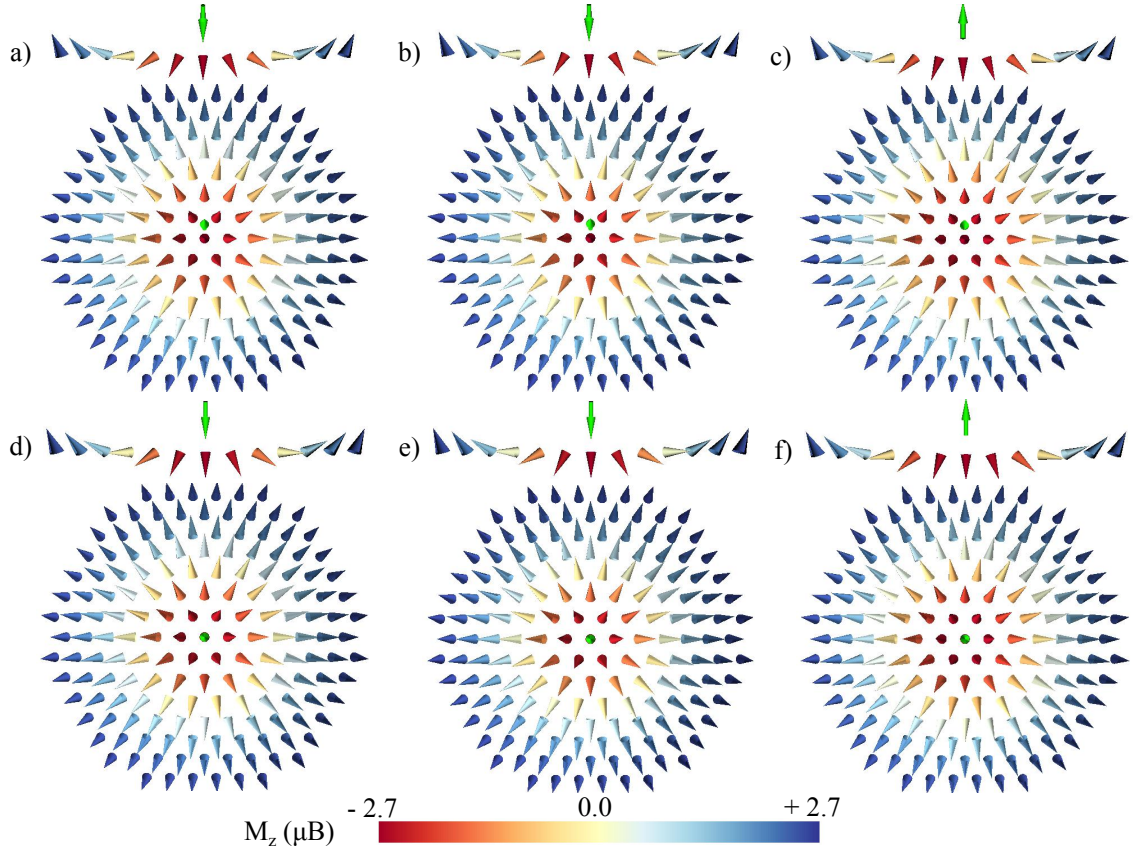


Figure 6.7: Spin structure of skyrmion interacting with (a,d) Co, (b,e) Fe and (c,f) and Cr adatom. The top panel showcases the system in the FCC stacking, while the bottom panel is for the configuration in in the HCP stacking. The green arrow represents the direction of the impurity magnetic moment. The colorbar represent the magnitude of the magnetization in z-direction for each Fe atom.

of the underneath Fe atom. However, in the FCC stacking since the Fe defect has 3 Fe atoms in the substrate as its first nearest neighbors, its magnetization will try to align with the direction of the spin moments of these three Fe atoms. The variation of the energy profiles of each element can be also studied further by looking on how the present foreign adatom affects the interaction among the spin moments of Fe atoms in the substrate. This will be explained in more detail for different elements in the following paragraphs.

In all cases we obtained that the impurity locally lowers the exchange interaction among Fe atoms which make the presence of a skyrmion become more favorable (see Fig. 6.5). On the other hand, the defects also provide an additional exchange interaction which favors a collinear order inside the cluster. However, the magnitude of this interaction is smaller than the exchange coupling among the nearest neighboring Fe atoms, since, as previously mentioned the adatoms are located faraway from the Fe layer with their interaction being mediated via the Pd layer. The competition between the variation on the exchange and the DM interaction which are responsible for the collinear and non-collinear order among the spin moments will determine the magnitude of the total energy difference between the inside and outside the cluster region. The increase in the exchange energy has a tendency to give a positive total energy difference resulting in a repulsive behavior.

For the interaction of the Co and Cr adatoms with a single magnetic skyrmion in both FCC and HCP stackings, we found that the DM interaction energy at the region close to the impurity is lower than the one at the reference point while the exchange interaction energy inside the cluster increases. However, we found that the change in exchange energy is larger than the variation of the DM contribution. Thus, the main energy contribution is provided from the exchange energy, resulting in the observed repulsive profile. The main difference between the skyrmion-defect interaction for the Co and Cr case can be seen from the repulsion strength of their energy profiles which is related to the differences in the magnitude of the impurity-substrate exchange interactions.

Among the studied impurities, the Fe defect induces the largest reduction on the exchange interaction among the Fe-substrate, increasing the tendency towards non-collinearity. On the other hand, the energy contribution from the exchange interaction between the Fe impurity and the Fe-substrate tends to increase the total energy inside the cluster region. Thus, for the Fe adatom, the energy contribution from the impurity-substrate interaction compensates the reduction from the Fe-substrate exchange interaction, resulting in a slightly higher total energy interaction inside the cluster than the one at the reference point and yields a low repulsive strength as can be observed on the energy profile (see Fig. 6.6(b)).

## 6.2.2 Dimer

This section discusses the interaction of a single magnetic skyrmion with a dimer located on top of the Pd layer. We have analyzed the following configurations both on the FCC and HCP staking shown in Fig. 6.8: (a, d) dimer-1 with the defects in a nearest neighbor dimer configuration, (b, e) dimer-2 in which one impurity is moved to the second nearest neighbor, and (c, f) dimer-3 with the defects in a third neighbor dimer configuration. The dimer-1 was analyzed by considering the following chemical configurations, Co-Co, Fe-Fe, Cr-Cr, and Co-Cr. Meanwhile, in dimer-2 and dimer-3 configurations we only studied a pair of atoms with the same elements.

In general, it is found that the magnetic moments are lower than the ones obtained for the adatoms with the largest decrease is found for the Cr dimer around 2.5% from the value in adatom case. We found that Co has the lowest spin moment,  $2.12 \mu_B$ , followed by Fe,  $3.31 \mu_B$ , and lastly Cr,  $3.64 \mu_B$ . The decrease in the spin moments is due to the increase in coordination number of the impurity by the additional neighboring impurity atom [15, 29]. The larger coordination number impact on the higher hybridization between to impurities that leads to a smaller spin moment.

Since there are two impurities located on the top of the Pd layer it is also useful to study the exchange interaction between them as well as the impact on the exchange interaction among the Fe atoms. Among the investigated systems, the dimer-1 configuration shows the largest impurity-impurity exchange interaction, as can be seen in table 6.2. We have found that the Cr atoms tend to couple antiferromagnetically with each other while the Co and Fe dimer present a ferromagnetic coupling. In the dimer-1 configuration, there is a strong hybridization between the defects since they are nearest neighbors. However, by increasing the distance between them the hybridization is weakened, which drastically reduces the magnitude

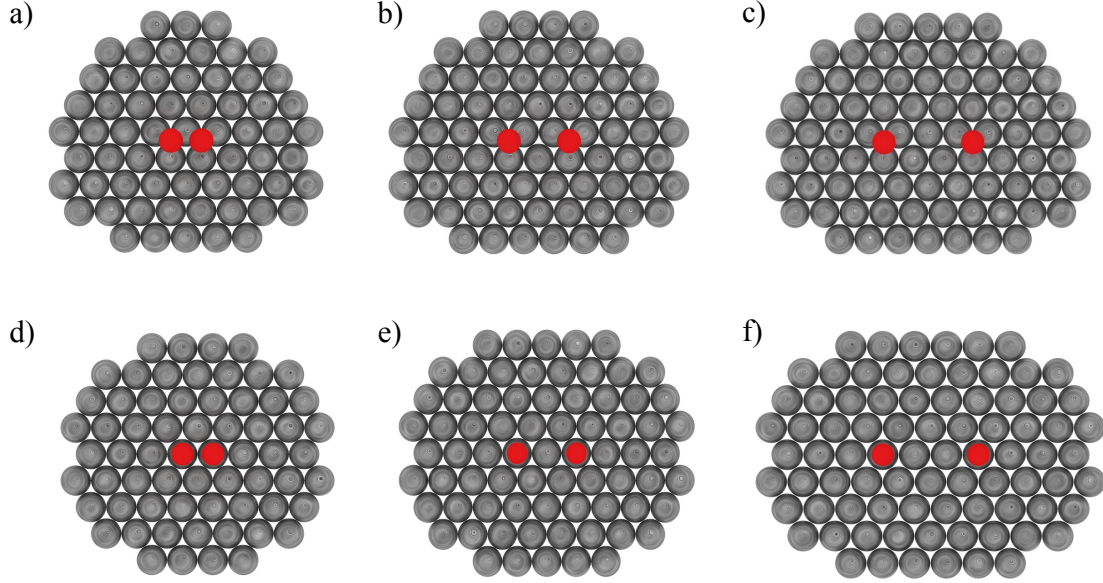


Figure 6.8: The variation of dimer system configuration based on the spatial distance between the impurities. The red sphere indicates the impurity atoms and the grey one shows the Fe atoms in the substrate. The top and below panel present the configuration in FCC and HCP stacking, respectively. Figure (a,d) represents the dimer-1, (b,e) for the dimer-2 and (c,f) for dimer-3 configurations.

of the direct exchange interaction between the impurities. The change of the distance between the impurities does not only affect the interaction among them, but also impacts their interaction with the Fe substrate and the variation induced by them on the Fe-Fe exchange interactions. In table 6.2, one can see that by increasing the separation between the impurities from nearest neighbour to next nearest neighbour, the impurity-substrate exchange interaction increases while the reduction on the Fe-Fe exchange interaction become smaller. We also can notice that in dimer-3 configuration where two impurities are faraway from each other, the magnitude of the impurity-substrate exchange interaction and the reduction induced on the Fe-Fe exchange interaction are close with the ones obtained in the adatom case. This means that the increase of the separation between the impurities makes the direct interaction between them less pronounced and each of them tend to affect their nearest neighboring Fe atoms independently.

After analyzing the magnetic properties and the exchange interaction between the defects in the studied dimer configurations as well as their impact on the Fe atoms exchange interaction, we proceed to investigate the interaction on these defects with a single magnetic skyrmion.

### Co dimer

As in the case of the Co-adatom, for an applied external magnetic field of  $H = 10$  T, it is found that all the investigated Co-dimer configurations tend to repel the single magnetic skyrmion (see Fig. 6.9). The interaction of the two Co impurities with the Fe substrate raises the impurity-substrate exchange energy by increasing the collinearity among the spin moments. This leads to a higher energy inside the cluster than the one at the reference point and leads to repulsion. We also found that

Table 6.2: The exchange interaction coupling between impurities of dimer  $J_{\text{imp-imp}}$ , the average exchange interaction between impurity dimer with the Fe atoms  $\langle J_{\text{Imp-Fe}} \rangle_{\text{INN}}$ , and the average of exchange interaction coupling between the central Fe atom and its first-nearest neighbors  $\langle J_{\text{Fe-Fe}} \rangle_{\text{INN}}$  are given in meV.

Cluster	Stacking	Element	$J_{\text{Imp-Imp}}$	$\langle J_{\text{Imp-Fe}} \rangle_{\text{INN}}$	$\langle J_{\text{Fe-Fe}} \rangle_{\text{INN}}$
Dimer-1	FCC	Cr	-41.80	-14.20	14.70
		Fe	36.80	7.40	15.02
		Co	40.40	7.60	15.32
	HCP	Cr	-43.30	-14.2	14.50
		Fe	33.50	10.30	13.80
		Co	35.00	9.00	14.80
Dimer-2	FCC	Cr	-0.36	-12.20	15.70
		Fe	0.20	8.40	15.20
		Co	0.14	8.50	16.20
	HCP	Cr	-1.30	-12.02	15.13
		Fe	1.12	7.50	14.00
		Co	0.46	8.30	15.30
Dimer-3	FCC	Cr	0.17	-12.02	16.68
		Fe	-0.25	8.30	16.01
		Co	0.19	8.48	16.80
	HCP	Cr	-0.05	-11.60	15.40
		Fe	-0.03	7.30	14.06
		Co	0.21	8.00	15.30

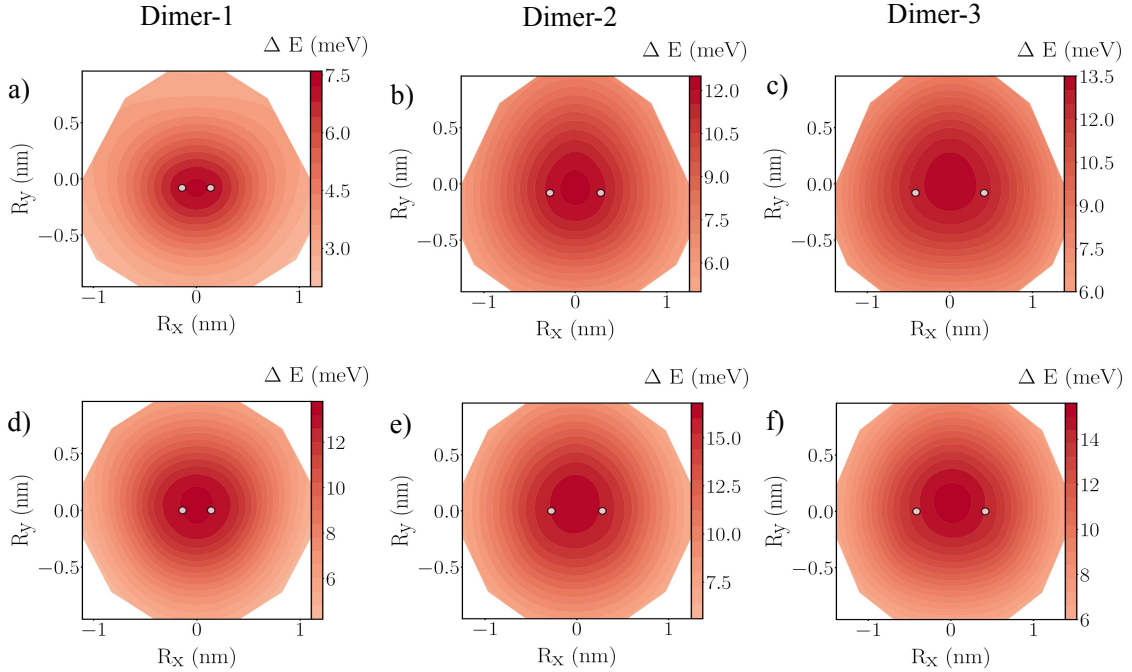


Figure 6.9: The energy profile of skyrmion interacting with Co dimer. The figures at the top and bottom panel present the interaction in the FCC and HCP stacking, respectively. In all dimer configurations for both stackings, the Co defects have a tendency to repel a magnetic skyrmion. The strength of repulsion is changed once the separation between the impurities is increased.

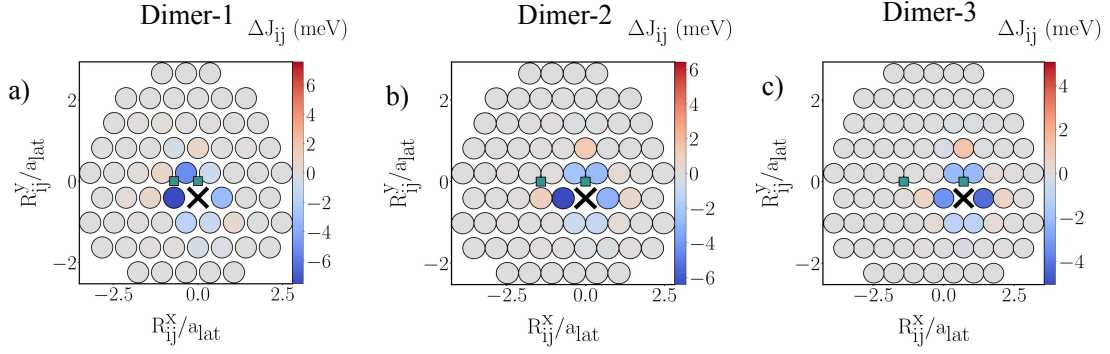


Figure 6.10: The variation of the exchange interaction between one Fe atom in the substrate (cross sign) with its first nearest neighbor atoms induced by the present of Co (green square) in (a) dimer-1, (b) dimer-2, and (c) dimer-3 configurations in FCC stacking. The increase on the spatial distance between impurities generate a change on the Fe-Fe exchange interaction. The larger separations of Co impurities in dimer-2 and dimer-3 configurations tend to make the Fe-Fe exchange is less reduced when compared to the dimer-1.

for both stackings in the dimer-1 configuration, Co atoms have the lowest strength of repulsion as can be seen in Fig. 6.9. As previously discussed, the increase on the separation between the impurities decreases the impact on the Fe-Fe exchange interaction (see Fig. 6.10). On the other hand, the ferromagnetic coupling between each Co atom and the substrate favors a collinear configuration inside the cluster region. Therefore, once a skyrmion interacts with the Co impurities in dimer-2 and dimer-3 configurations, the repulsion is stronger than in the dimer-1 case. We also found that the increase of the distance between impurities lower the reduction of the Fe-Fe exchange interaction in the region between the impurities. Although the impurity-substrate exchange interaction in this region is small, the overall exchange energy interaction arising in this region has the highest value leading to the most repulsive area. A similar behavior is also found in the HCP stacking, where the Co impurities in all dimer systems disfavors the presence of a magnetic skyrmion as shown in Fig. 6.9(d)-(f).

## Fe dimer

In the FCC stacking, among the investigated chemical elements, the Fe-dimers show the lowest exchange interaction between the impurity and the Fe-substrate, as can be seen in table 6.2. Despite of both Fe and Co couple ferromagnetically with the Fe substrate, for the dimer-1 configuration the Fe dimer shows a different behavior when interacting with a single magnetic skyrmion with some attractive areas on the energy profile (see Fig. 6.11(a)). One can also see that for the Fe atom which is located at the center of the cluster between the Fe impurities, there is a slightly repulsive behavior. The behavior observed on the energy landscape for the dimer-1 configuration is related to the variation induced by the dimer on the exchange interaction of the Fe substrate as well as the strength of the impurity-substrate exchange interaction. In general, we found that the Fe dimer lowers the exchange interaction among the nearest neighbor Fe atoms in the substrate which favors the the non-collinearity among the spin moments. Among the impurity elements, the

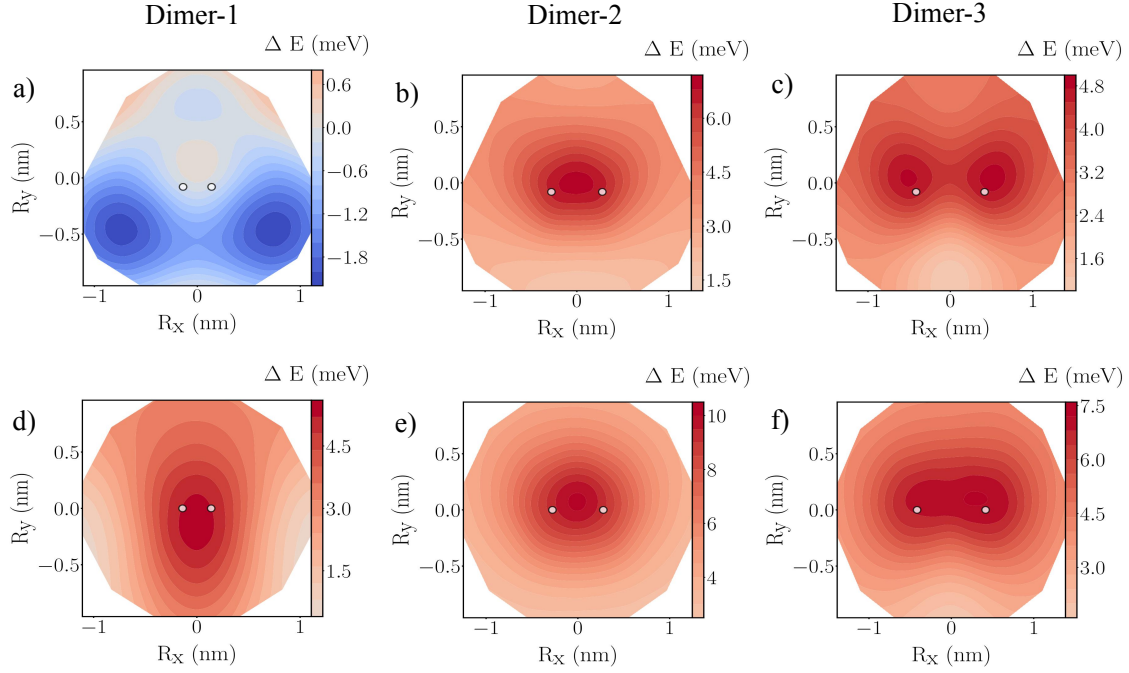


Figure 6.11: The energy profile of skyrmion interacting with Fe dimer. The figures at the top and bottom panel present the interaction in the FCC and HCP stacking, respectively. In dimer-1 configuration for the FCC stacking (a) the Fe impurities have a tendency to attract a magnetic skyrmion, while they become repulsive for the HCP stacking (d). By increasing the separation between two impurities, the interaction behavior in dimer-2 (b,e) and dimer-3 (c,f) configurations turn to be repulsive for both stackings.

Fe dimer also shows the lowest impurity-substrate exchange coupling which results in a low exchange energy, leading to attraction behavior. However, for the Fe atom at the center of cluster its impurity-substrate exchange interaction with the two Fe impurities increases the overall exchange energy and yields a repulsive behavior at this point. We found that the difference between the total energy at this point with the one at the reference point is relatively small, thus, the strength of the repulsion is very low. On the contrary, for the HCP stacking a repulsive behavior is found. This is because the reduction induced by the Fe dimer on the exchange interaction among the nearest neighboring Fe atoms close to the impurities is much lower than in the FCC stacking case. Therefore, the total energy inside the cluster is higher than outside region which then leads to a repulsive behavior.

By increasing the separation between the impurities, the interaction profile becomes repulsive in the FCC stacking. In the dimer-2 configuration, the change in the nearest neighbor exchange coupling of the Fe atoms, that lie between the impurities, is found to be smaller than in the dimer-1 case, that is the system tends more towards ferromagnetism. This makes the contribution of the exchange energy from the ferromagnetic interaction of Fe atoms in the central cluster get enhanced. As a result, a high repulsive behavior is concentrated there. As we increase the distance between the Fe impurities up to the third nearest neighbor shell, the reduction induced by the Fe dimer is lower than in the dimer-2 case. In Fig. 6.12 one can see in more detail the comparison of the variation induced by the Fe dimer when

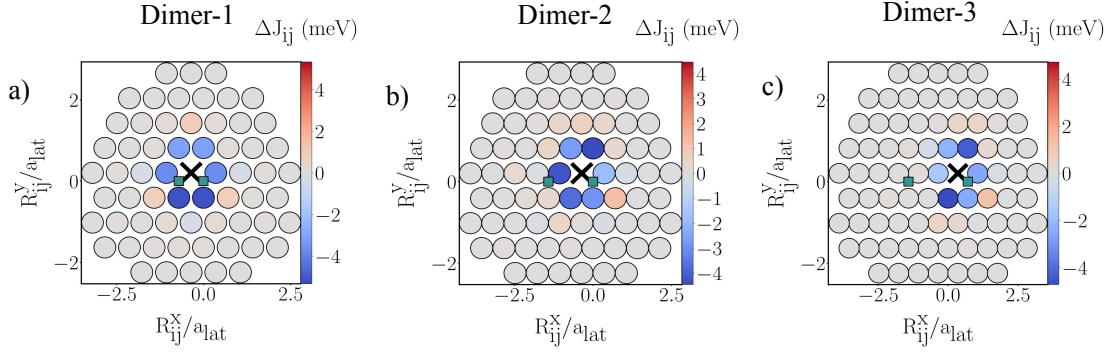


Figure 6.12: The variation of the exchange interaction between one Fe atom in the substrate (cross sign) with its first nearest neighbor atoms induced by the present of Fe impurities (green square) in (a) dimer-1, (b) dimer-2, and (c) dimer-3 configurations in FCC stacking. The change in the spatial distance between impurities leads to a different variation induced by the Fe dimer on the exchange interaction among the Fe atoms which are close to the impurities.

the spatial distance between impurities is increased. For the dimer-3 configuration where the two impurity atoms are located quite far from each other, they behave more as uncoupled impurities and give a more localized change in the Fe atoms close to the impurities, which is reminiscent of the change produced by a single adatom. As a result the energy profile, shows two energy maxima located at the impurity sites. The same trend is also shown in the HCP stacking, i.e., when the distance of impurities is increased the energy profile behaves more and more as a superposition of the individual profiles produced by an adatom.

### Cr dimer

For the dimer-1 configuration, in contrast with the previously studied cases where a collinear configuration was preferred, the Cr impurities exhibit a tendency towards a non-collinear order. This is a result of a competition between the exchange interaction between the impurities which prefers them to tend be antiparallel to each other and exchange interaction between the defects and the Fe-substrate, which prefers them to couple antiferromagnetically to the Fe substrate. For the Cr dimer-1 configuration, the magnitude of the impurity-substrate exchange interaction is relatively weaker than the exchange interaction among the impurities. Thus, on the ground state both Cr atoms couple antiferromagnetically to the substrate but their magnetic moments are tilted  $\sim 15^\circ$  from the direction of the magnetization of the Fe-substrate with both of the Cr spin moments is found pointing towards each other. By using this non-collinear ordering as the initial magnetic configuration for the Cr impurities, we calculated the total energy for the interaction with a single magnetic skyrmion inside the impurity region and at the reference point. We found that the total energy inside the cluster region is lower than the one obtained at the reference point, yielding an attractive energy profile as shown in Fig. 6.13(a).

The Cr dimer also lowers the exchange interaction among the Fe substrate favoring the skyrmion to be located inside the impurity cluster. On the other hand, the Cr dimer provides a strong exchange interaction to the substrate which has a tendency towards repulsion. However, due to the non-collinearity of the magnetization

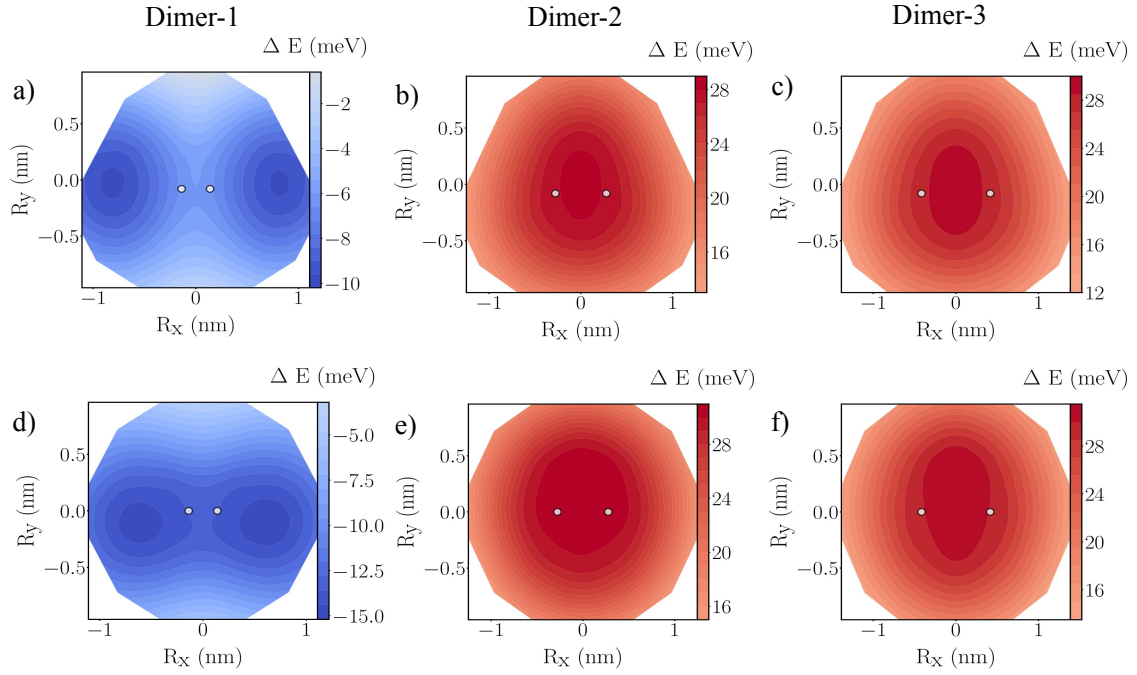


Figure 6.13: The energy profile of skyrmion interacting with Cr dimer. The figures at the top and bottom panel present the interaction in the FCC and HCP stackings, respectively. Figure (a, d) showcases the interaction for dimer-1, (b, e) dimer-2, and dimer-3 configuration. In dimer-1 configuration the Cr impurities has a tendency to attract a magnetic skyrmion. By increasing the separation between two impurities, the interaction behavior turn to be repulsive.

of the Cr dimer, the impurity-substrate exchange energy decreases. This condition lowers exchange energy contribution leading to an attractive interaction behavior. The same trend is also found in the HCP stacking resulting in the same attractive behaviour as shown in Fig. 6.13(d).

Interestingly, the most attractive region is not located at the center of the cluster but it is located at two symmetric points located at the sides of each of the atoms (see Fig. 6.13(a)). We can analyze these two attractive areas by looking at the magnetic structure of the Cr impurities when interacting with the skyrmion. As shown in Fig. 6.14(a), the Cr impurities have the largest deviation angle with respect to the ground state at these points. As previously discussed the non-collinear magnetic structure is found for the Cr impurities configuration due to competition between the Cr-Cr interaction and the substrate. Once the skyrmion is placed at these points and interacts with Cr atoms the energy is minimized, resulting in the most attractive potential. As the core of skyrmion moves towards the center of the cluster, the magnetic configuration of the impurities changes the direction of their magnetization. From Fig. 6.14(a-b), one can see that both moments of the impurities change their orientation until one of them is in-plane as shown in Fig. 6.14(c). As the skyrmion core is located exactly at the center of cluster, the moment of Cr impurities becomes more symmetric at which they are facing toward to each other with the same deviation angle as shown in Fig. 6.14(d). With such configuration, the interaction between the Cr impurities and a magnetic skyrmion then results in the highest energy at the central point of the cluster compared to the other region.

Remarkably, by increasing the distance between the Cr impurities, the skyrmion-defect interaction behavior changes to be repulsive for both stackings (see Fig. 6.13). In the dimer-2 and dimer-3 configurations, we found that each Cr impurity at the ground state are oriented antiferromagnetically to the substrate. The increase of the separation between the Cr atoms reduces their impact on the exchange interaction among the Fe-substrate with the reduction of the exchange interaction for the nearest neighbour Fe atoms being smaller than in the dimer-1 system. This results in a preference towards a collinear configuration which leads to a repulsion. The larger distance between the impurities in the dimer-3 configuration also makes the reduction on the exchange interaction among the Fe atoms that lie between them become less pronounced compared to the dimer-2 case. As a result, the strength of repulsion on the region between impurities in dimer-3 is higher than in dimer-2 as seen in Fig. 6.14(f). From the interaction between the Cr dimer with a single magnetic skyrmion, one can see that the exchange frustration leads to an interesting behaviour. The non-collinearity induced by the frustration of the Cr atoms in the dimer-1 configuration leads to a transition from a repulsive behavior in adatom case into the attractive one. Once the separation between the impurities is increased, the exchange frustration between the Cr atoms is severely diminished, resulting in a repulsive behavior.

### **Mixed dimer (Co-Cr)**

In the dimer system with mixed elements, we use a combination of Co and Cr impurities to ascertain if these two atoms known to be repulsive can give rise to an attractive interaction. We only investigated the dimer-1 configuration for this case where both defects are considered as nearest neighbours. From the obtained results, we found that Co and Cr atoms couple anti-ferromagnetically with an effective renor-

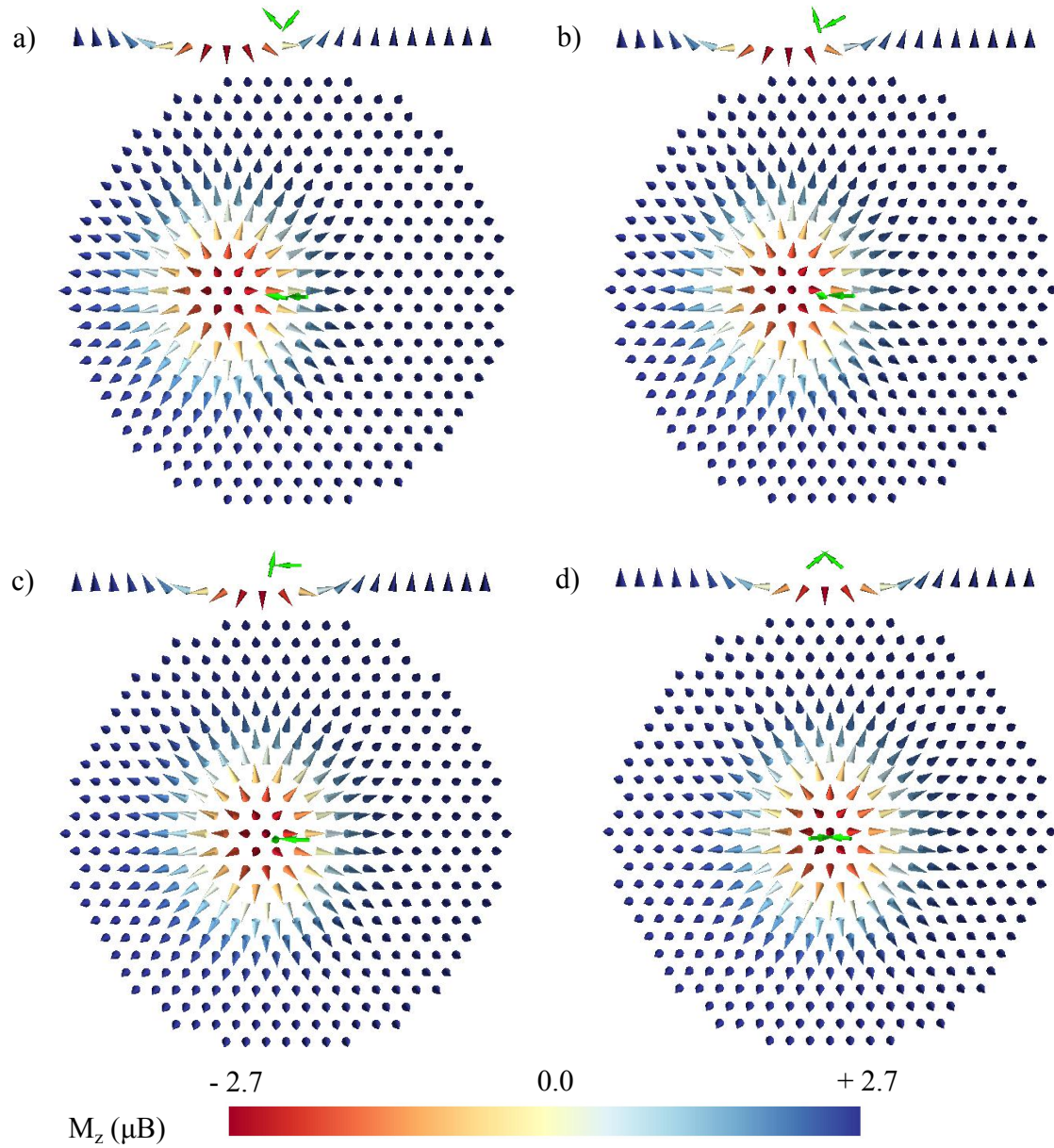


Figure 6.14: The skyrmion profile for the interaction with Cr dimer-1. The green arrow represents the direction of the impurity magnetic moment. Figures (a-d) shows the change of Cr dimer magnetization when the core of skyrmion is moved from the lowest energy point to the center of cluster. The colorbar represents the magnitude of the magnetization in the z-direction for each Fe atom.

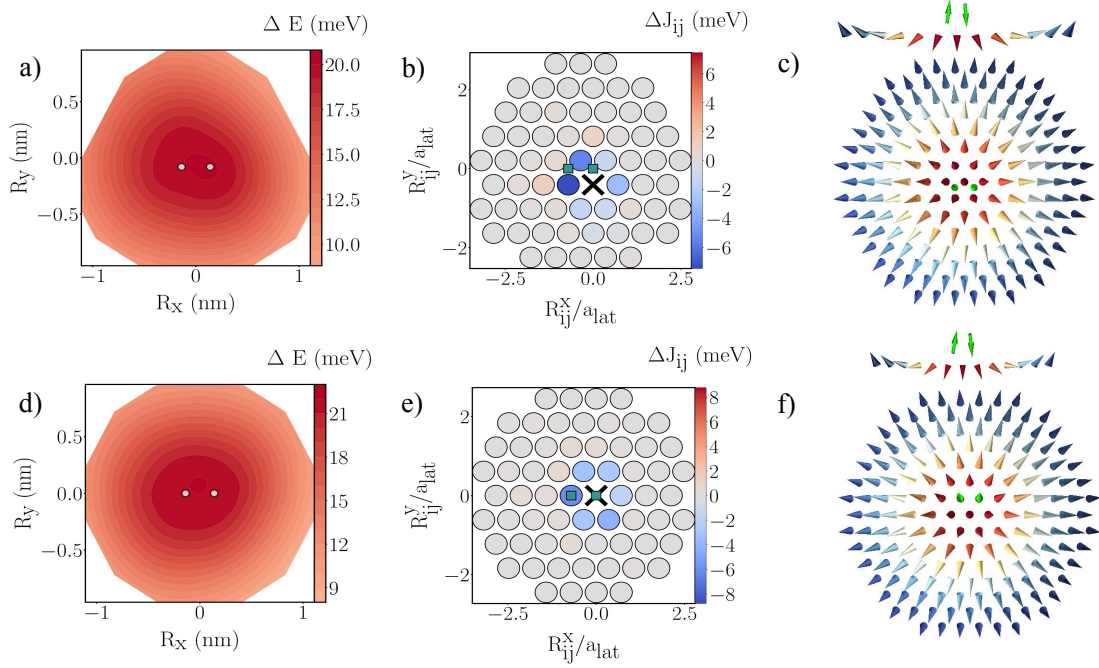


Figure 6.15: The top and bottom panel show the figures in FCC and HCP stacking, respectively. (a, c) The energy profile of skyrmion-defect interaction for the mixed-dimer case where the left white point indicates the Cr impurity and the right one is the Co impurity. A non-symmetric profile is produced on the energy landscape due to a different interaction behavior of each element impurities. (b, d) The variation of the nearest neighboring Fe-Fe exchange interaction induced by the Co-Cr dimer in the FCC stacking is more pronounced than in the HCP stacking case. (c, f) The skyrmion profile at the center of cluster interacting with the mixed Co-Cr dimer, where both impurities prefer a collinear configuration with the local spin moments.

malized exchange interaction of  $J = -27$  meV in the FCC stacking and  $J = -23$  meV in the HCP stacking. As expected from their adatom behaviors, the Co atom is ferromagnetically coupled to the substrate whilst Cr couples antiferromagnetically. The average of the renormalized exchange interaction between the Co impurity with their nearest neighboring Fe atoms in the substrate are  $J = 8.6$  meV and  $J = 9.4$  meV in FCC and HCP stacking respectively. Meanwhile, the Cr impurity has a larger average of the exchange interaction with a magnitude of  $J = -10.14$  meV for the FCC and  $J = -10.15$  meV for the HCP stacking.

Similar to the previous cases, there is a local reduction on the exchange interaction on the Fe substrate as can be seen in Fig. 6.15(b) and (e) for the FCC and HCP stacking, respectively. It can be seen that for the HCP stacking the reduction on the exchange couplings is less pronounced than for the FCC case. In the obtained energy profile for the skyrmion-defect interaction presented in Fig. 6.15 (a) and (d), we can see that the Co-Cr dimer repels the skyrmion which is similar to the behavior observed for each element in the adatom case. However, due to the different strength of exchange coupling exhibited by each impurity with the Fe-substrate as well as the reduction induced on the exchange interaction on the Fe substrate, the energy profile is not symmetric. We found that the exchange interaction among the Fe atoms close to the Cr impurity is reduced by 5.0 meV, while for those which are

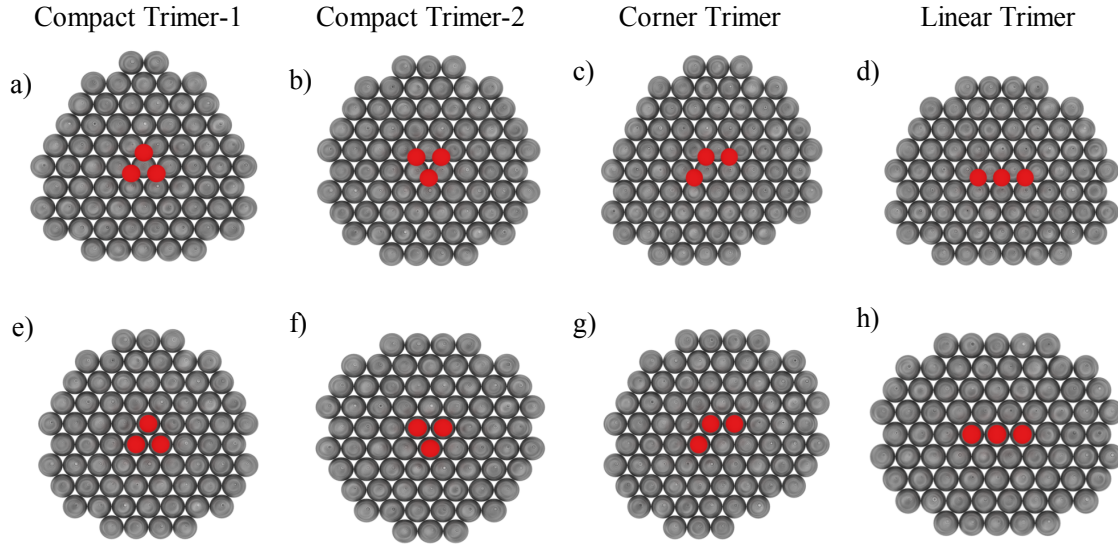


Figure 6.16: The top view of impurity position atop the Fe substrate in each trimer cluster configuration for FCC (a-d) and HCP stacking (d-f). The red spheres denote the impurity and the gray ones indicate the Fe atoms.

close to the Co atom the reduction is 4.6 meV. On the other hand, we also found that the Cr impurity has a larger spin moment and larger exchange interaction with the Fe substrate compared to the Co impurity. This then leads to a higher and wider area of repulsion shown on the left region of the energy landscape where the Cr impurity is located. In the HCP the repulsion is found to be stronger than in the FCC stacking, due to a lower reduction in the exchange interactions among the Fe atoms induced by the dimer.

### 6.2.3 Trimer

We now focus on the effect that trimers have over the skyrmion energy landscape. We considered three different geometrical structures as can be seen in Fig. 6.16, a compact trimer with two types of configurations namely type-1 Fig. 6.16(a, e) and type-2 Fig. 6.16(b, f), a corner trimer Fig. 6.16(c, g), and linear trimer Fig. 6.16(d, h). Similarly to the adatom and dimer case, the trimers were composed of Cr, Co, and Fe on two different stackings.

#### Compact trimer-1

The compact trimer-1 configuration is formed by moving an adatom close to the dimer such that they form an equilateral triangle (see Fig. 6.16(a, e)). Since there are now three atoms, the coordination number of one impurity in the trimer configuration increases due to the additional two neighboring atoms and gives rise to a smaller magnitude of its spin moment compared to the adatom and dimer case. Fig. 6.17 presents a comparison of the total DOS of the Co impurity in adatom, dimer, and trimer configurations. As one can see, in the DOS of the Co trimer for both stackings (see the green line) a lower peak (broader bandwidth) is shown on their spin-up and down states. The decrease on the peak is due to the increase of coordination number which give rise a more hybridization on the Co atom in trimer

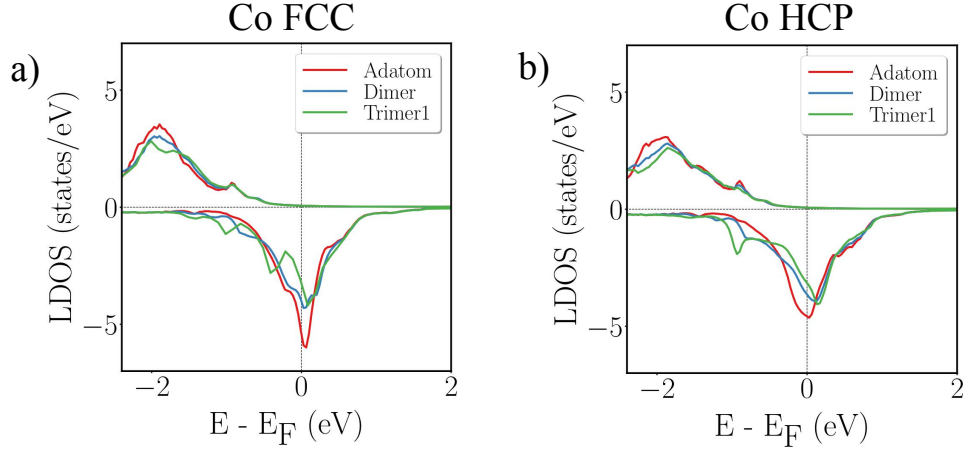


Figure 6.17: The comparison of total DOS of Co impurity in the adatom, dimer, and trimer configuration in the (a) FCC and (b) HCP stacking. The increase of coordination number in the trimer configuration leads to a broader bandwidth on the spin states which give rise to a smaller integrated DOS and resulting in a smaller spin moment.

configuration. As a result, the area of the integrated DOS for the trimer case will have a smaller value than the other configurations, leading to the lowest spin moment. The same trend is also shown in the DOS of the Fe and Cr trimer. It was found that for both stackings the Co and Fe atoms have spin moments of  $2.08 \mu_B$  and  $3.21 \mu_B$ , respectively. Meanwhile, for the Cr impurity, we found that one atom at the top-corner of the triangle has the magnitude  $3.41 \mu_B$  and the other two have a lower value  $3.38 \mu_B$ . The different spin moment of the Cr trimer is due to a different coupling orientation where one moment is coupled antiferromagnetically with the other two moments.

The difference in impurity-substrate interactions and the variation of the Fe-Fe exchange interaction induced by each impurity element leads to a different energy profile as shown in Fig. 6.18. As one can see, the Co impurities in the compact trimer-1 configuration show the same behavior as in the adatom and dimer cases, repelling the magnetic skyrmion. In the FCC stacking, with the three Co atoms sitting on top of the substrate, the reduction induced on the Fe-Fe exchange interaction is larger than in the adatom and dimer cases (see table 6.3). However, with a larger number of defects, the impurity-substrate exchange interaction in this system is also increased, increasing the tendency to have a collinear order of the spin moments which results in a repulsive behavior when interacting with a single magnetic skyrmion. As expected, the repulsive strength on the energy profile is different for the FCC and HCP stacking due to a different exchange interaction energy induced by the Co trimer in each of these cases. As presented in table 6.3, in both stackings the reduction induced by the Co trimer is the same, however, in the HCP stacking there is a contribution from the ferromagnetic interaction between each of the Co impurities and their second nearest neighboring atoms in the Fe substrate, which increases the overall exchange energy and gives rise to a higher repulsion strength.

In both stackings, the Fe trimer locally reduces the ferromagnetic behavior of the Fe substrate, increasing the tendency towards non-collinearity. In contrast with the Co system, the stacking type makes a large difference in the energy profile for the Fe

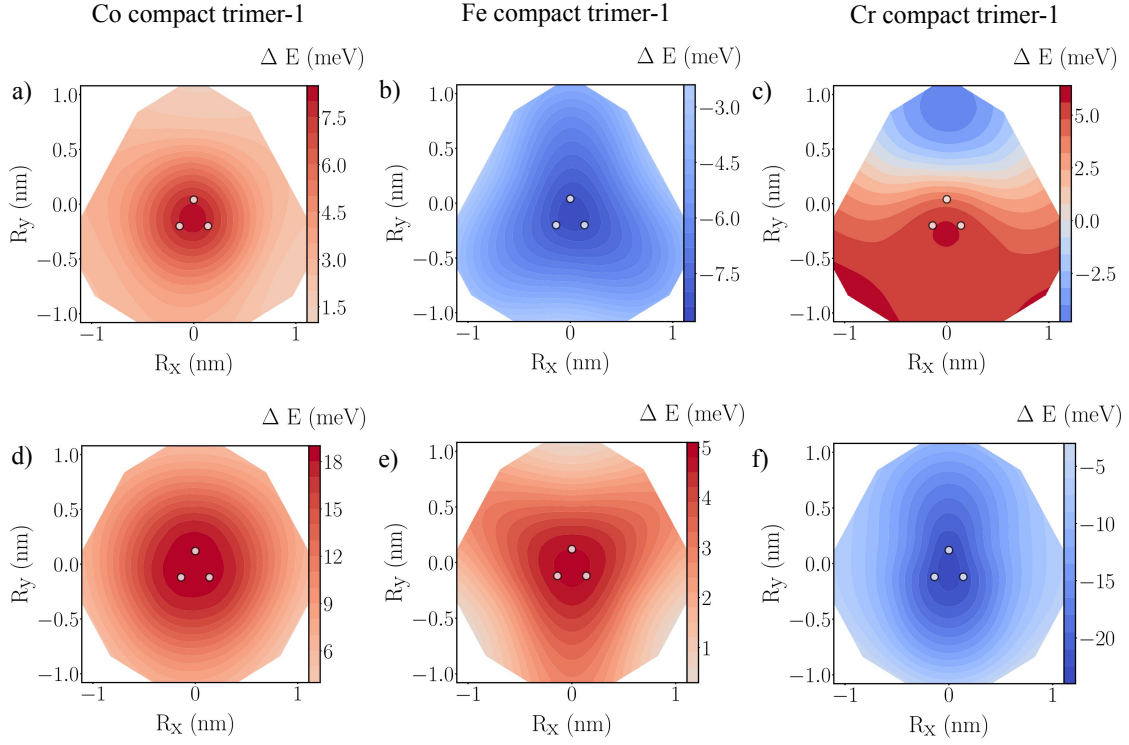


Figure 6.18: The energy profile of skyrmion interacting with impurities in compact trimer-1 configuration. The figures at the top and bottom panel present the interaction in the FCC and HCP stacking, respectively. The Co (a, d) trimer prefer to have a repulsive interaction with a single magnetic skyrmion. Meanwhile, for the Fe trimer the interaction behavior depends on the stacking site which can be either attractive (b) for the FCC or repulsive (d) for the HCP stacking. The Cr trimer show an anisotropic interaction profile in the FCC stacking (c), and become attractive due to a larger deviation on its magnetization in the HCP satcking (f).

Table 6.3: The average of the exchange interaction between impurity with its first nearest neighbor Fe atoms in the substrate  $\langle J_{\text{Imp-Fe}} \rangle_{1\text{NN}}$ , the average value of exchange interaction coupling between the central Fe atom and the first-nearest neighbors  $\langle J_{\text{Fe-Fe}} \rangle_{1\text{NN}}$ , and the modulus DM vectors,  $\langle |D_{\text{Fe-Fe}}| \rangle_{1\text{NN}}$ , and the magnetic anisotropy energy constant of the defect  $K^{\text{imp}}$ .

Stacking	Element	$\langle J_{\text{Imp-Fe}} \rangle_{1\text{NN}}$	$\langle J_{\text{Fe-Fe}} \rangle_{1\text{NN}}$	$\langle  D_{\text{Fe-Fe}}  \rangle_{1\text{NN}}$	$K^{\text{imp}}$
Compact Trimer-1 (FCC)	Cr	3.4	13.6	1.06	0.5
	Fe	6.2	14.4	1.20	-0.3
	Co	7.0	14.5	1.13	0.6
Compact Trimer-1 (HCP)	Cr	0.3	13.5	1.00	-0.15
	Fe	8.0	13.5	1.23	0.12
	Co	6.8	14.5	1.18	1.0

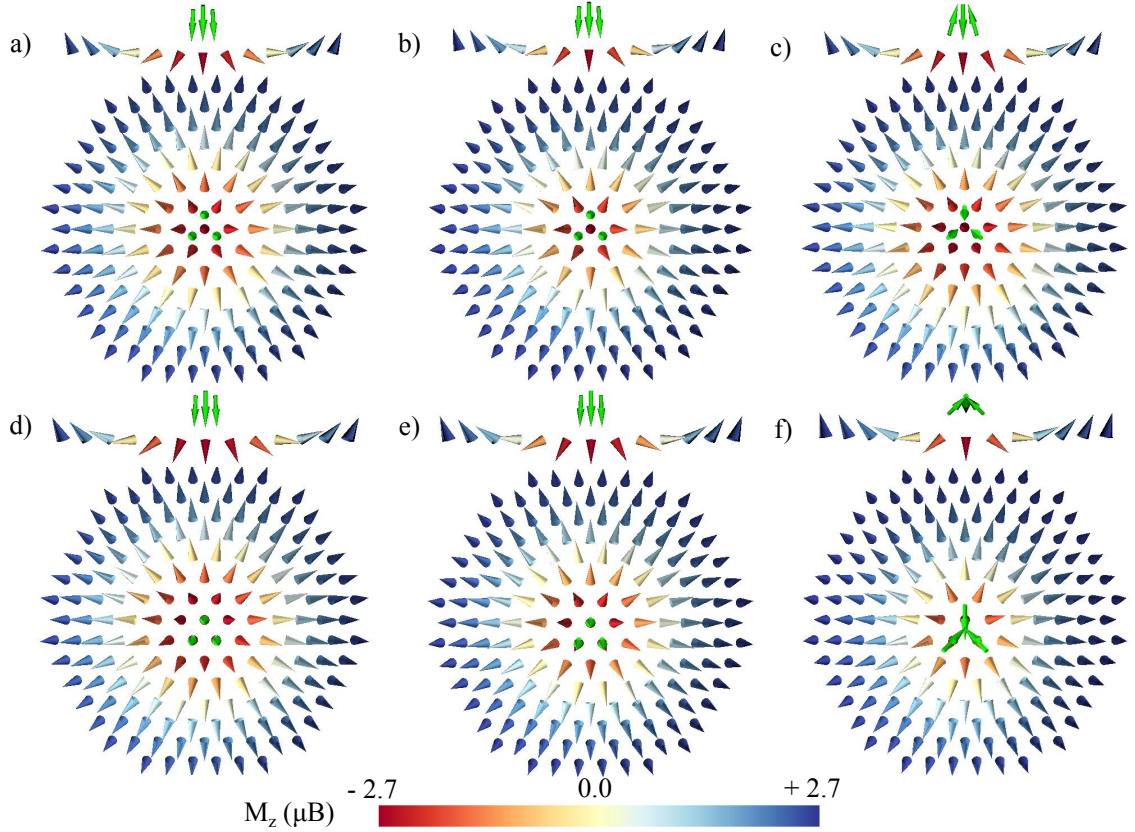


Figure 6.19: The skyrmion profile for the interaction with defects in compact trimer-1 configuration. The green arrow represents the direction of the impurity magnetic moment. The figures on the left (a,d), middle (b,e), and right (c,f) columns represent the Co, Fe, and Cr impurity, respectively. The top panel figure showcases the system in FCC stacking, while the bottom panel figures are in the HCP stacking. Notice that the Co and Fe trimer prefer a collinear configuration with the local spin moment when interacting with a skyrmion. Meanwhile, the Cr trimer shows a non-collinearity on its magnetization direction with a large deviation in the HCP stacking case.

trimers, the FCC stacking shows an attractive potential, whilst the HCP stacking showcases a repulsive behaviour. This behaviour can be tracked to the differences on the change of the local exchange interactions, which are strongly reduced in the FCC stacking. This condition results in a preference towards non-collinearity, and thus attract a magnetic skyrmion. On the other hand, in the HCP case such reduction is not enough to counteract the impurity-substrate interaction, thus a small repulsive potential is found on the skyrmion-defect energy interaction.

For the Cr trimer, we can see an anisotropic shape on the energy profile in the FCC stacking (see Fig. 6.18(c)) due to a variation of the exchange energy inside the cluster. On the lower region of the cluster which shows a repulsive behavior, we found that the exchange interaction between one Fe atom and the nearest neighboring is lowered by  $\sim 0.2$  meV. Meanwhile, the reduction on the Fe-Fe exchange interactions occurring at the Fe atoms on the upper region is  $\sim 3$  meV. This higher reduction leads to a larger decrease on the exchange energy and thus the presence of skyrmion is favored on the upper area. On the other hand, at the Fe atom that lies between the

two side-corner Cr impurities on the lower region, the strongest repulsive behavior can be seen (see Fig. 6.18(c)) due to its exchange interaction with the two Cr atoms which increases the collinear order of the spin moments.

The difference on the energy profile for the FCC and HCP stackings can be understood if one looks at the magnetic configuration obtained when they interact with a skyrmion. We found that when the core of the skyrmion is located at the reference point, the magnetic configuration of the Cr trimer in the FCC stacking remains in the collinear state. However, in the HCP stacking a non-collinear configuration is found with the Cr spin moments deviating by a collective tilting angle with respect to the substrate. This tilting angle is induced by the competition of the exchange interaction between the Cr atom at the top-angle corner and the Fe substrate with the antiferromagnetic coupling with its two companions [70]. This competition is not well pronounced in the FCC stacking as the interaction of each Cr atom with its three nearest neighboring Fe atoms in the substrate is large enough to make them to stay in the collinear configuration. When the core of skyrmion is moved to the center of the cluster, the magnetic configuration of the Cr trimer changes as shown in Fig. 6.19(f). A larger deviation of the magnetization can be seen in the HCP stacking which leads to a large decrease in the exchange interaction energy. Thus, it is possible to see a pattern appearing, systems in which there is a strong exchange frustration can lead to attractive potentials, even if the single atoms provide a repulsive potential. Which means, that by engineering these defects one can create complex energy landscapes, without the need of using distinct chemical species.

## Compact trimer-2

The compact trimer-2 configuration has the same shape as the compact trimer-1 but it is rotated by  $180^\circ$ , due to the  $C_{3v}$  symmetry of the lattice this rotation results in these two configurations not being equivalent as can be seen in Fig. 6.16(b) and (f). As done for the compact trimer-1, we also have investigated the magnetic configuration at the ground state for different elements. In both stackings, we found that the Co and Fe trimer prefer an FM configuration with respect to the Fe substrate. For the Co trimer we obtained that the magnetic moment of the Co trimer is  $2.1 \mu_B$  for the FCC and  $2.07 \mu_B$  for the HCP stacking. The Fe trimer has a larger spin moment than the Co trimer with a magnitude of  $3.22 \mu_B$  and  $3.20 \mu_B$  for the FCC and HCP stackings, respectively. For the Cr system, the ground state magnetic configuration is similar to the one obtained for the trimer-1 configuration for both stackings where one Cr atom is ferromagnetically aligned to the Fe substrate (the one at the bottom corner of triangle) whereas the two remaining atoms are antiferromagnetically coupled to the substrate. The spin moment of the Cr atom sitting at the bottom corner is  $3.4 \mu_B$  and  $3.35 \mu_B$  for the FCC and HCP stackings respectively, while its companions have the same spin moment of  $3.15 \mu_B$  for the FCC and  $3.33 \mu_B$  for HCP stacking. The Heisenberg exchange parameters for the impurity-substrate interaction, the averaged exchange coupling and modulus of DM vectors for the interaction among the nearest neighboring Fe atoms in the substrate, as well as the magnetic anisotropy constant for each defect are presented in table 6.4.

In general the compact trimer-2 atop the host system reduces locally the exchange interaction among the Fe substrate as shown in table. 6.4. Although all the trimers have the same magnetic configuration as in the compact timer-1 system, they do not show the same energy profile when interacting with a single magnetic

Table 6.4: The average value of exchange interaction between trimer impurity with the Fe atoms  $\langle J_{\text{Imp-Fe}} \rangle_{\text{1NN}}$ , the average value of exchange interaction coupling,  $\langle J_{\text{Fe-Fe}} \rangle_{\text{1NN}}$ , and the modulus DM vectors,  $\langle |D_{\text{Fe-Fe}}| \rangle_{\text{1NN}}$ , between the one Fe atom in the substrate with its first-nearest neighbor atoms, and the magnetic anisotropy energy constant of the defect  $K^{\text{imp}}$ . All the quantities presented in the table are in unit of meV.

Stacking	Element	$\langle J_{\text{Imp-Fe}} \rangle_{\text{1NN}}$	$\langle J_{\text{Fe-Fe}} \rangle_{\text{1NN}}$	$\langle  D_{\text{Fe-Fe}}  \rangle_{\text{1NN}}$	$K^{\text{imp}}$
Compact Trimer-2 (FCC)	Cr	5.9	14.5	1.16	-0.02
	Fe	3.0	13.4	1.15	0.97
	Co	4.2	14.2	1.17	-0.41
Compact Trimer-2 (HCP)	Cr	4.5	13.0	1.03	0.2
	Fe	8.0	12.0	1.21	0.24
	Co	5.2	13.0	1.21	0.1

skyrmion. The Co trimer for this case still shows a tendency to repel the skyrmion in the both stackings, with the highest repulsive area concentrated at the Fe atom in the middle of the cluster. At this Fe atom, the variation induced on the Fe-Fe exchange interaction competes with the contribution from the impurity-substrate interaction resulting in the highest exchange energy. Thus, a strong repulsive potential is found at this point. One can also notice that the shape of the energy profile in the FCC stacking is different than in the compact trimer-1 case. This is due to a different local environment, where the impurity-substrate exchange coupling and the variation on the exchange interaction among the Fe atoms close to the central cluster is smaller than in the compact trimer-1 configuration, which leads to a change on the energy landscape. On the other hand, in the HCP stacking the Co compact trimer-2 gives a symmetric shape of the energy profile as what was observed in compact trimer-1 with the most repulsive area found at the Fe atoms in the central of cluster.

The Fe defects in the compact trimer-2 configuration for both stackings also show the same interaction profile as in the compact trimer-1 case. In the FCC stacking it shows an attractive behavior and a repulsive interaction on the HCP case. Similar to the case of the compact trimer-1 system, the Fe trimer in the FCC stacking produces a greater reduction of the exchange coupling among the Fe atoms in the substrate compared to the HCP stacking. As a result, the interaction among the Fe moments inside the cluster region become less ferromagnetic in the FCC stacking which then leads the skyrmion to be the more favorable state close to the Fe impurities. In comparison with the energy landscape in the compact trimer-1, the most attractive region is not found at middle of the three impurities, instead it is located slightly above and between the two Fe impurities (see Fig. 6.20)(b)). The exchange interaction between the Fe atom, which lies between these two Fe impurities, with its nearest neighbors is strongly reduced by the presence of the trimer. On the other hand, the impurity-substrate interaction of this Fe atom with the substrate is relatively small. Therefore, the exchange energy at this point is highly reduced compared to the other regions resulting in the highest attractive potential.

In the compact timer-2 configurations the Cr trimer shows an attractive behavior in both the FCC and HCP stackings. With the presence of a single skyrmion at

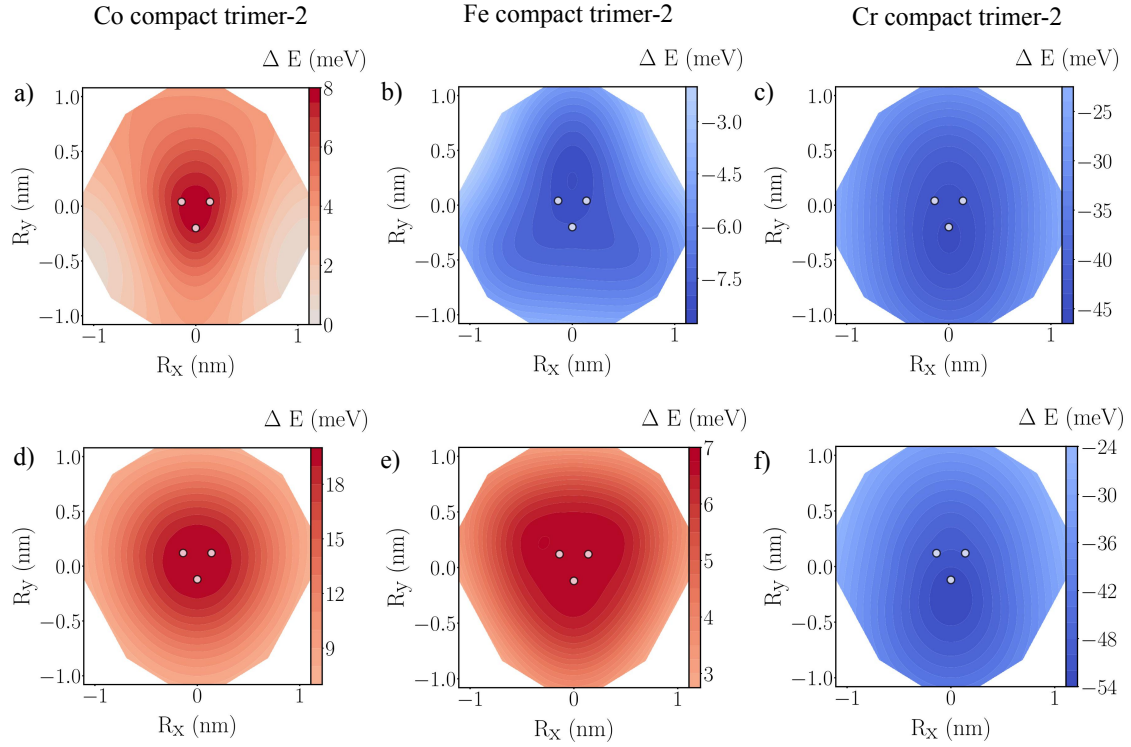


Figure 6.20: The energy profile of skyrmion interacting with impurities in compact trimer-2 configuration. The figures at the top and bottom panel present the interaction in the FCC and HCP stacking, respectively. Each figure showcases the interaction with different impurity elements namely (a, d) Co, (b, e) Fe, and (c, f) Cr atoms. The positive value on the total energy difference in the profile indicates a repulsive skyrmion-defect interaction. A variation in the interaction profile can be seen for the Fe trimer case which is changed from the attractive in the FCC into the repulsive one in the HCP stacking. In the compact trimer-2 configurations, the Co and Cr trimer prefer the repulsion and attraction for their interaction with magnetic skyrmion, respectively.

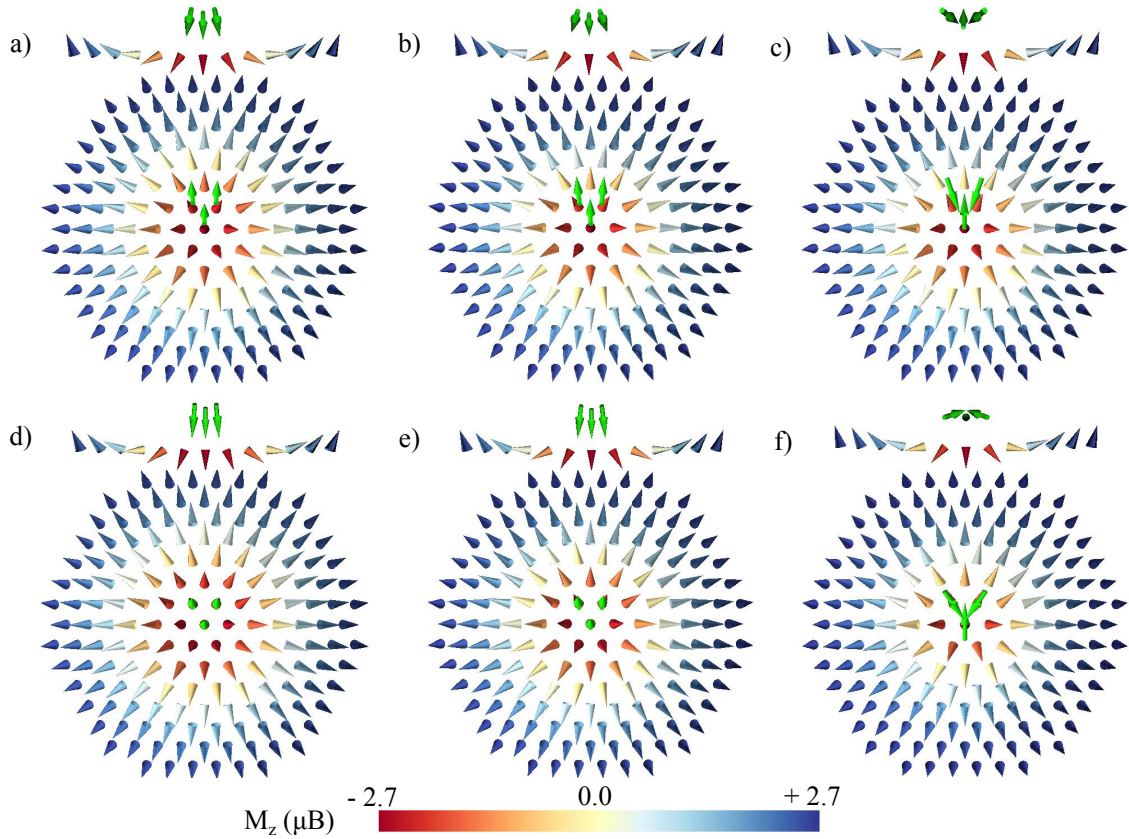


Figure 6.21: The skyrmion profile for the interaction with defects in compact trimer-2 configuration. The green arrow represents the direction of the impurity magnetic moment. The figures in the left (a,d), middle (b,e), and right (c,f) columns represent the Co, Fe, and Cr impurity, respectively. The top panel figure showcases the system in FCC stacking, while the bottom panel figures are in the HCP stacking. For the interaction with skyrmion at the center of cluster, both the Co and Fe trimer prefer a collinear configuration with the local spin moments. Meanwhile some deviation can be seen in the magnetization of the Cr impurities which leads to the lower exchange energy and result in an attractive behavior.

the reference point, the magnetic configuration of the Cr trimer impurities in both stackings are found to be no longer in a collinear state. The three Cr impurities are deviated in respect to the direction of the magnetization of the Fe substrate, similar to the case of compact trimer-1 for the HCP stacking (see 6.2.3). The two spin moments of the Cr trimer which have the same magnetization also experience a deviation where both of them are pointing towards each other. The deviation of the magnetization of the Cr impurities then reduces the exchange energy between the impurities and their nearest neighboring Fe atoms. When the core of skyrmion is located at the Fe atom close to the impurity, the non-collinear order of the Cr atoms is exacerbated, that is, they have a larger tilting angle (see Fig. 6.21(c, f)) which lowers the exchange energy contribution, hence favoring the presence of the skyrmion in the impurity cluster.

### Corner trimer

The “corner trimer” configuration is formed by moving one of the adatoms in the compact trimer in such a way the three adatoms form an isosceles triangle with one angle of  $120^\circ$  and two angles of  $30^\circ$  (see Fig. 6.16). In this trimer system, the magnetic configuration of the Co and Fe atoms is coupled ferromagnetic with the substrate for both stackings. For the Co trimer, the central adatom, i.e the one sitting at the angle of  $120^\circ$ , has a spin moment of  $2.07 \mu_B$  and the remaining two have the same spin moment of  $2.11 \mu_B$ . Meanwhile, the Fe trimer has a spin moment of  $3.2 \mu_B$  for the central adatom and  $3.3 \mu_B$  for the neighboring impurity atoms. The values of the spin magnetic moments do not change much in the HCP stacking. The different spin moment of the central Co or Fe atom compared to the other two impurities is related to a different nearest neighbor coordination number. The central adatom has a higher coordination number since it interacts with the two nearest neighboring impurities while each of the other two impurities only see the central adatom as its nearest neighbor. Therefore, the increased number of nearest neighbor atoms results in a decrease of its local spin moment.

On the other hand, the Cr trimer in this system shows a different magnetic ordering for each stacking configuration. In the FCC stacking, the central Cr adatom is aligned ferromagnetically to the substrate with a spin moment of  $3.4 \mu_B$ . The moment of the other two adatoms are antiferromagnetic oriented to the Fe substrate and each of them carries the same spin moment of  $3.5 \mu_B$ . However, in the HCP stacking we found that the three of Cr adatoms are found in a ferromagnetic alignment with respect to each other and antiferromagnetically to the substrate. They have a spin moment of  $3.5 \mu_B$  for the central adatom and  $3.6 \mu_B$  for its neighboring atoms.

The unequal distance between the two impurities in the corner trimer leads to a different value of the exchange coupling constant among them. As expected, for all impurity elements the exchange interaction between the central impurity atom with its neighboring atoms is much larger than the interaction among its two companions, due to the larger distance between them. In table 6.5, we present the Heisenberg exchange parameters for the impurity-substrate interaction, the averaged exchange coupling and the modulus of DM vectors between the Fe atom which is close to the central impurity with its nearest neighbor atoms, as well as the magnetic anisotropy constant for each defect.

With these obtained parameters, we follow the same procedure as done in the previous systems to establish the energy profile for the interaction between the skyrmion

Table 6.5: The average value of exchange interaction between impurity with the Fe atoms  $\langle J_{\text{Imp-Fe}} \rangle_{\text{INN}}$ , the average value of exchange interaction coupling,  $\langle J_{\text{Fe-Fe}} \rangle_{\text{INN}}$ , and the modulus DM vectors,  $\langle |D_{\text{Fe-Fe}}| \rangle_{\text{INN}}$ , between the one Fe atom in the substrate with its first-nearest neighbor atoms, and the magnetic anisotropy energy constant of the defect  $K^{\text{imp}}$ . All the quantities presented in the table are in unit of meV.

Stacking	Element	$\langle J_{\text{Imp-Fe}} \rangle_{\text{INN}}$	$\langle J_{\text{Fe-Fe}} \rangle_{\text{INN}}$	$\langle  D_{\text{Fe-Fe}}  \rangle_{\text{INN}}$	$K^{\text{imp}}$
Corner Trimer (FCC)	Cr	6.60	12.91	1.2	0.62
	Fe	2.85	12.06	1.2	0.004
	Co	3.90	12.34	1.2	0.2
Corner Trimer (HCP)	Cr	7.4	13.35	1.1	0.002
	Fe	6.03	12.20	1.2	0.14
	Co	3.7	12.86	1.2	0.9

and the defects. As shown in Fig. 6.22, the interaction profile for the Co trimer in both stackings do not show any changes from the compact trimer configuration with a repulsive behavior. As previously discussed, the strong magnetic nature of the Co impurity atoms increasing the exchange interaction leads to a repulsive potential.

The interaction of the Fe trimer with the magnetic skyrmion in the HCP stacking shows a similar repulsive behavior as in the compact trimer configuration, however in the FCC stacking, the Fe trimer shows a different behavior on its profile. As can be seen in Fig. 6.22, there are regions which have an attractive behavior with the energy minima can be found faraway from the impurities. However, this reduction is counterbalanced by the ferromagnetic exchange interaction between the Fe trimer and its nearest neighboring atoms in the Fe substrate which tends to strengthen the collinear ordering. As a result, the interaction of the impurity with the skyrmion at the region close to the Fe impurities does not present the lowest energy which means that the most attractive region is not found there. At the two points with the energy minima, we found that the magnetization of the Fe trimer become close to be in-plane oriented.

The energy profile for Cr impurities shows an anisotropic shape for the FCC and HCP stackings. The magnetic configuration of the Cr trimer on the FCC stacking shows the same ordering than the compact trimer-1 where the central impurity atom couples ferromagnetically to the substrate while the other two atoms couple antiferromagnetically to the substrate. The different orientation of the Cr moments induces a variation on the exchange energy inside the cluster region. On the upper area, we can see a small pinning area where the skyrmion can be trapped by the Cr impurities. Meanwhile, on the lower region a repulsive behavior can be observed. On the area with the attractive behavior, we found a higher reduction on the exchange interaction among the Fe substrate induced by the Cr trimer. We also observed that once the skyrmion is imposed in the attractive region, the orientation of the Cr moments shifts to an in-plane orientation. The opposite situation is found on the lower region in which the smaller reduction on the exchange interaction of the Fe substrate in addition with the impurity-substrate exchange interaction of the two outer Cr impurities, which are aligned in the same direction, favors the collinearity leading to the repulsive behavior as observed in Fig. 6.22(c). A similar profile is also be observed in the HCP case, however, the repulsive region is less pronounced than in the FCC case. In the HCP stacking, the Cr spin moments are tilted due to a

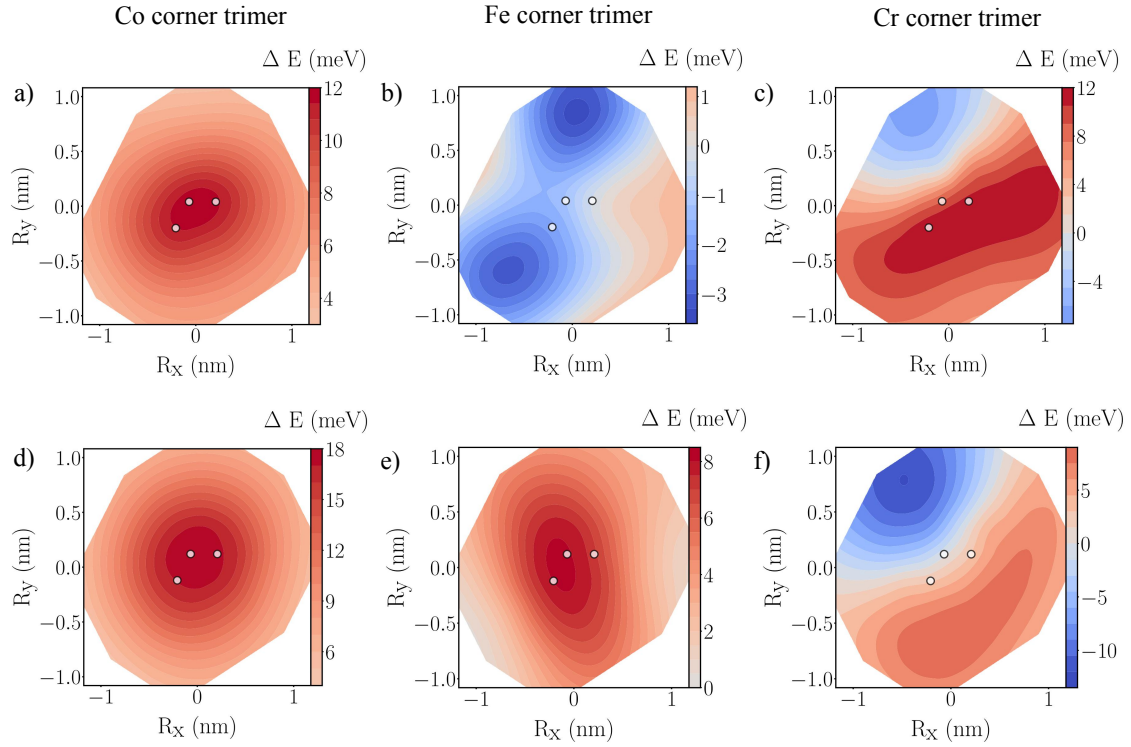


Figure 6.22: The energy profile of skyrmion interacting with impurities in corner trimer configuration. The figures at the top and bottom panel present the interaction in the FCC and HCP stacking, respectively. The Co defects in corner trimer configuration prefer a repulsion for its interaction with magnetic skyrmion in both stackings (a, d). Fe trimer in this case showcases some attractive and repulsive interaction on the energy profile for the FCC (b) and become totally repulsive in the HCP stacking case (e). Meanwhile, the Cr trimer shows an anisotropic profile for both stackings (d, f) due to the a different alignment of its spin moments.

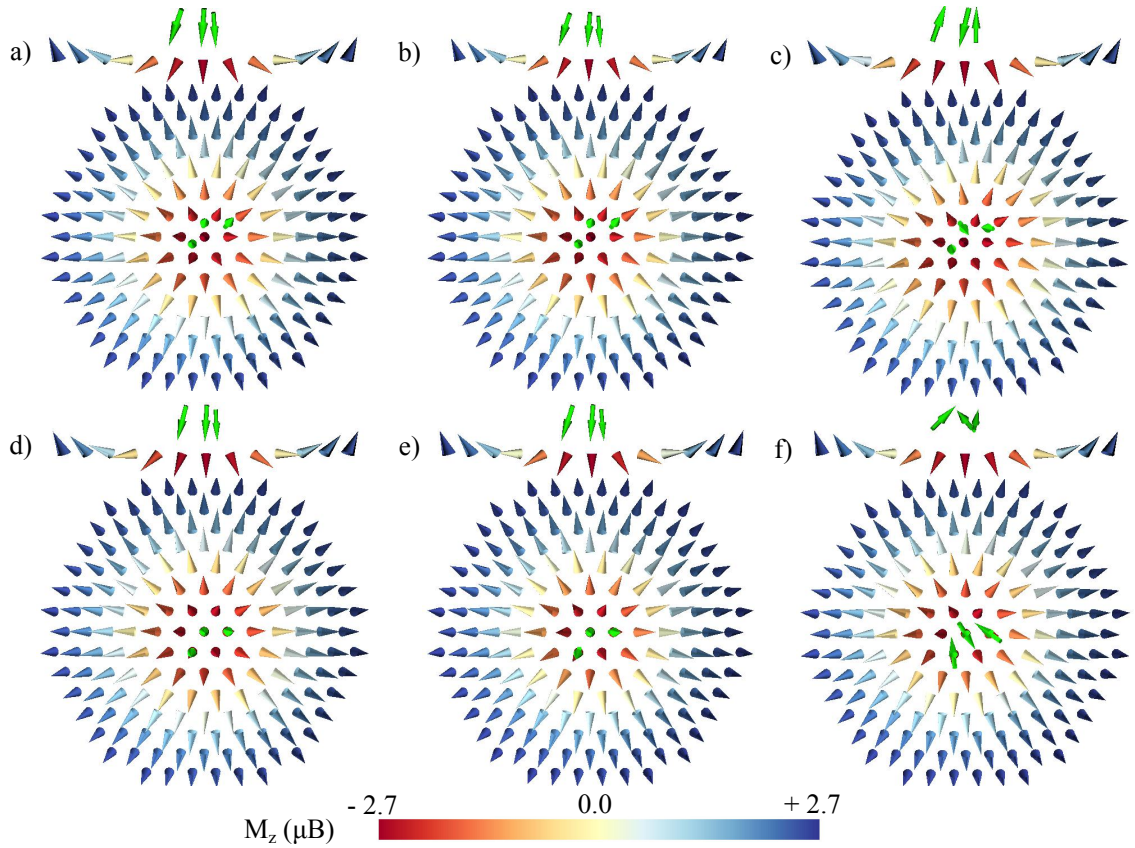


Figure 6.23: The skyrmion profile for the interaction with defects in corner trimer configuration. The green arrow represents the direction of the impurity magnetic moment. The figures in the left (a,d), middle (b,e), and right (c,f) columns represent the Co, Fe, and Cr impurity, respectively. The top panel figure showcases the system in FCC stacking, while the bottom panel figures are in the HCP stacking. One can notice on the figures that both Co and Fe trimer still shows a preference to be in collinear alignment in respect to the magnetization of the local spin moments. Meanwhile, the anti-ferromagnetic alignment preferred by the Cr moment.

competition between the exchange interaction from the impurity-impurity interaction with the one from the impurity-substrate interaction. Thus, the non-collinearity of the Cr moments leads to a lower exchange energy, resulting in a lower repulsive strength as shown in Fig. 6.22(f).

### Linear trimer

In the linear trimer configuration the three adatoms are placed in a straight line one next to the other as shown in Fig. 6.16 (d) and (f). In this configuration, the Co and Fe trimer have a ferromagnetic coupling with respect to the substrate. The central impurity atom has also a smaller spin moment compared to the other two atoms similarly with what was found on the corner trimer case. The central adatom has a larger coordination number as it has two nearest neighboring impurity atoms and the hybridization between the central atom with its neighbors results in a smaller magnetic moment. In the FCC stacking, the central Co atom carries a spin moment of  $2.08 \mu_B$  and the two remaining atoms have a spin moment of  $2.10 \mu_B$  while the Fe trimer has a spin moment of  $3.2 \mu_B$  for the central one and  $3.3 \mu_B$  for its two neighboring adatoms. In the HCP stacking, the spin moment of Co and Fe trimer experience a small reduction of about  $0.01 \mu_B$ . For the Cr case, the central adatom has a spin moment of  $3.5 \mu_B$  and the other two have a spin moment of  $3.6 \mu_B$  in both stackings. It is important to notice, that in contrast with the previous cases, the Cr atoms tend to prefer a ferromagnetic ordering among themselves, whilst orienting antiferromagnetically to the substrate.

As expected, for the Co trimer, the energy profile shows a repulsive behavior as seen in Fig. 6.24. The strength of the repulsion is similar to the ones in the other trimer configurations. Compared to the adatom and dimer case, the deeper and wider shape of the repulsion region at the center is due to the larger number of magnetic impurities which strengthen the collinear ordering of the Fe spin moments in the substrate.

The energy profile for the Fe trimer showcases the same behavior as in the previous cases, where the FCC stacking displays an attractive potential while the HCP stacking showcases a repulsive one. As one can see in table 6.6, in comparison to the Co trimer for the FCC stacking case, the Fe trimer causes a larger reduction on the exchange interaction among the substrate Fe atoms which are close to the impurities. This reduction increases the tendency towards non-collinearity among the spin moments. On the other hand, the contribution from impurity exchange interaction for this case is considerably small, thus, it can not counterbalance the reduction induced on the exchange interaction among the Fe-substrate. As a result, the exchange energy decreases leads to a lower total energy inside the cluster, producing the attractive behavior on the energy profile. Here, one can also notice that the largest attractive interaction of the energy landscape is not concentrated at the center of the cluster but its minima is located at symmetric positions perpendicularly to the longitude of the line (see Fig. 6.24(b)). For the Fe atoms at the center of cluster, there is a contribution of the ferromagnetic impurity-substrate exchange interactions which can increase the exchange energy. Thus, the interaction with the skyrmion at the center of cluster does not present the lowest exchange energy. However, once the skyrmion is placed at one of the regions with the most attractive behavior, the magnetic configuration of Fe defects tends to orient in-plane. The interaction between Fe defect and a skyrmion giving rise to a lower contribution

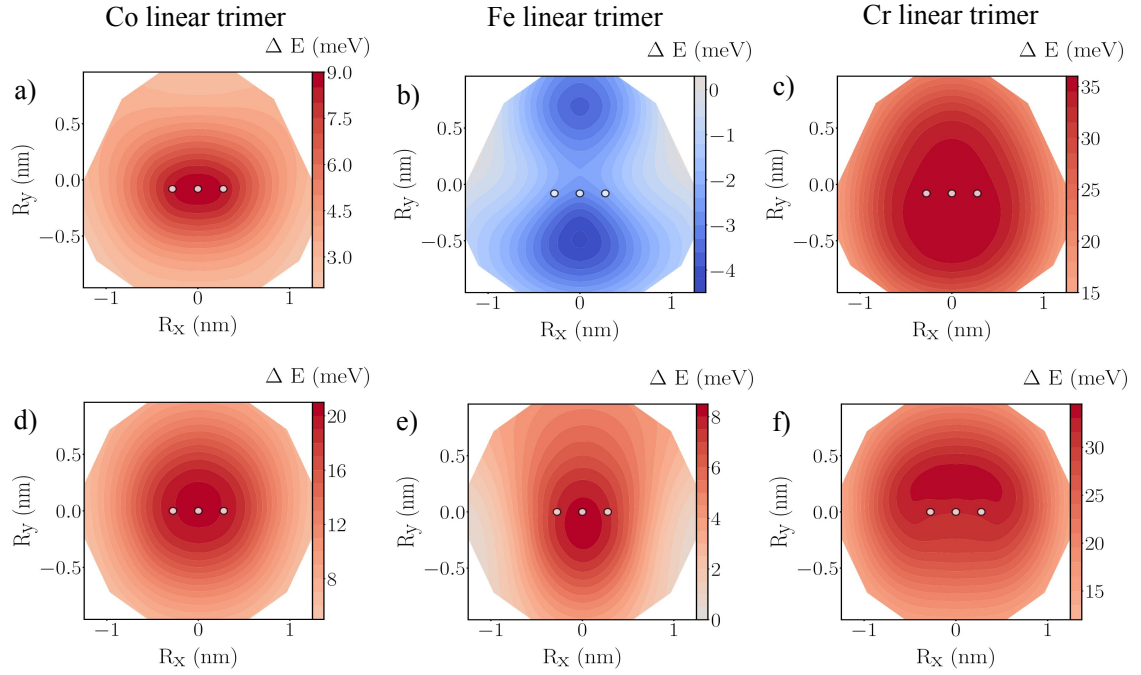


Figure 6.24: The energy profile of skyrmion interacting with impurities in linear trimer configuration. The figures at the top and bottom panel present the interaction in the FCC and HCP stacking, respectively. In their interaction with a single magnetic skyrmion, the Co (a, d) and Cr (c, f) impurities in linear trimer configuration show a preference to repel the skyrmion. Meanwhile the Fe impurities can be either attractive (b) or repulsive (e) depends on the stacking configuration.

Table 6.6: The average value of exchange interaction between impurity with the Fe atoms  $\langle J_{\text{Imp-Fe}} \rangle_{\text{1NN}}$ , the average value of exchange interaction coupling,  $\langle J_{\text{Fe-Fe}} \rangle_{\text{1NN}}$ , and the modulus DM vectors,  $\langle |D_{\text{Fe-Fe}}| \rangle_{\text{1NN}}$ , between the one Fe atom in the substrate with its first-nearest neighbor atoms, and the magnetic anisotropy energy constant of the defect  $K^{\text{imp}}$ . All the quantities presented in the table are in unit of meV.

Stacking	Element	$\langle J_{\text{Imp-Fe}} \rangle_{\text{1NN}}$	$\langle J_{\text{Fe-Fe}} \rangle_{\text{1NN}}$	$\langle  D_{\text{Fe-Fe}}  \rangle_{\text{1NN}}$	$K^{\text{imp}}$
Linear Trimer (FCC)	Cr	19.3	13.6	1.28	0.55
	Fe	6.0	13.6	1.45	-0.01
	Co	6.4	14.3	1.40	0.54
Linear Trimer (HCP)	Cr	20.1	13.7	1.11	-0.07
	Fe	11.8	13.2	1.25	0.27
	Co	9.4	14.2	1.32	1.07

from the impurity-substrate exchange interaction and leads to the lowest total energy. The behavior of the skyrmion-defect interaction for the Fe line changes in the HCP stacking because the larger impurity-substrate exchange coupling (see table 6.6) increases its contribution to the exchange energy which can compensate the reduction given by the variation of the Fe-Fe exchange interaction among the substrate Fe atoms. As a result, in the HCP stacking the total energy inside the cluster region is higher than in the reference point leading to a repulsive interaction with the magnetic skyrmion.

The Cr trimer in the linear configuration shows a repulsive behaviour for both stackings. In the FCC stacking, the Cr moments do not show a high frustration as was found in Cr dimer. The impurity-substrate exchange interaction in this case is strong enough to compete with the anti-ferromagnetic impurity-impurity exchange interaction and keep the magnetization in a collinear configuration. In comparison with the FCC stacking, the exchange coupling between the central Cr adatom with its neighboring impurity atoms in the HCP stacking ( $J = -28.7$  meV) is lower by 17% than the value in the FCC stacking. In the HCP stacking we found that once the skyrmion is placed at the reference point, the magnetization of the Cr impurities are no longer in collinear alignment. There is a deviation on the central Cr adatom due to the competition between its impurity-impurity exchange coupling with the exchange coupling from its interaction with the substrate that prevails to keep a collinear alignment, and leads to a tilting on the spin moments. As shown in the top view of Fig. 6.25(f) this deviation is more pronounced when the Cr interacts with the skyrmion at the center of cluster compared to the one in the FCC stacking (see Fig. 6.25(c)). The deviation from the collinear order of the central Cr adatom results in a lowering of the exchange energy resulting in the HCP stacking showcasing a lower repulsion than the FCC stacking.

## 6.2.4 Line cluster

Lastly, a line configuration with four atoms was also studied for both FCC and HCP stackings, as shown in Fig. 6.26. Consistently with the previous results, both Fe and Co defects are found to have a ferromagnetic ground state. In both stackings, the two Co adatoms in the middle have the same spin moment of  $2.06 \mu_B$  while the remaining two on the side positions have a slightly higher magnitude of  $2.1 \mu_B$ . For

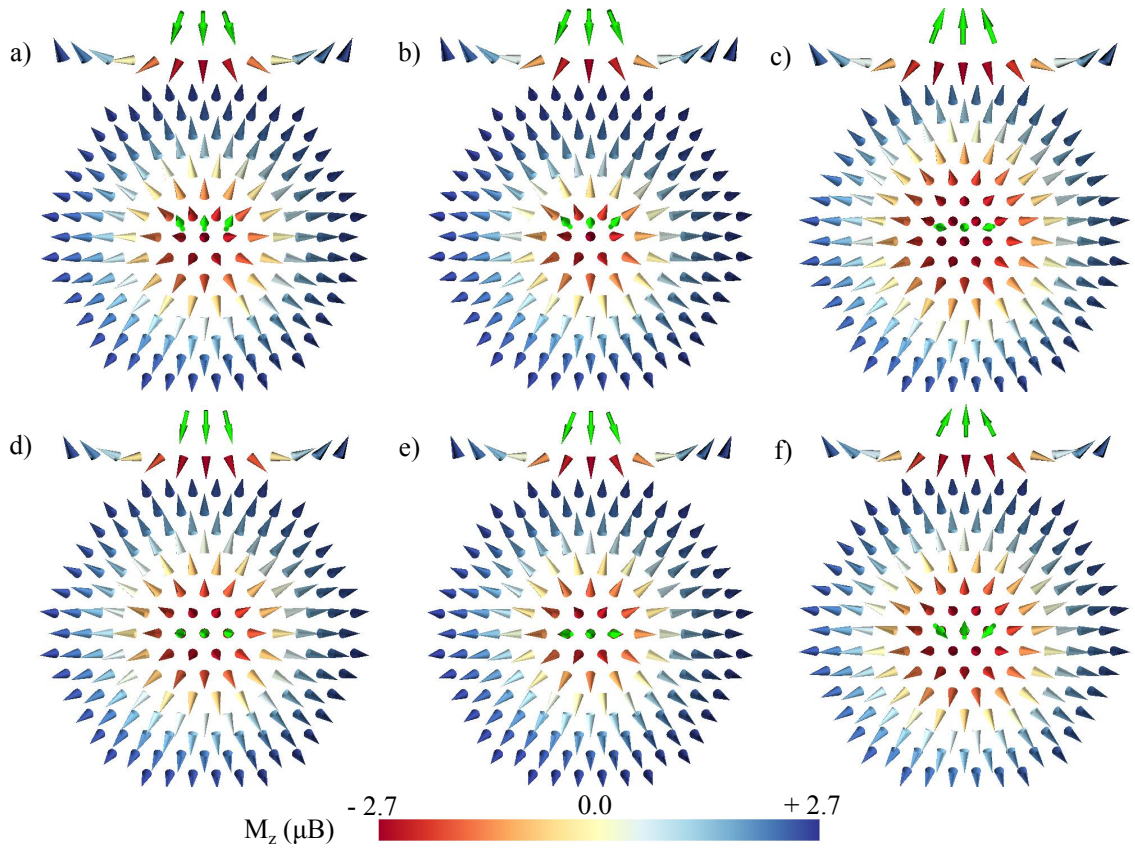


Figure 6.25: The skyrmion profile for the interaction with the linear trimer. The green arrow represents the direction of the impurity magnetic moment. The top panel figure showcases the system in FCC stacking, while the bottom panel figures are in the HCP stacking. Once the skyrmion is imposed close to the impurities, the magnetization of Co (a, d) and Fe (b, e) tend to align ferromagnetically with the direction of the local spin moment of the Fe substrate. Meanwhile, the Cr impurities (c, f) prefer the anti-ferromagnetic alignment. Due to a different impurity-impurity exchange coupling, the Cr trimer shows a larger deviation on its magnetization for the HCP stacking case (f).

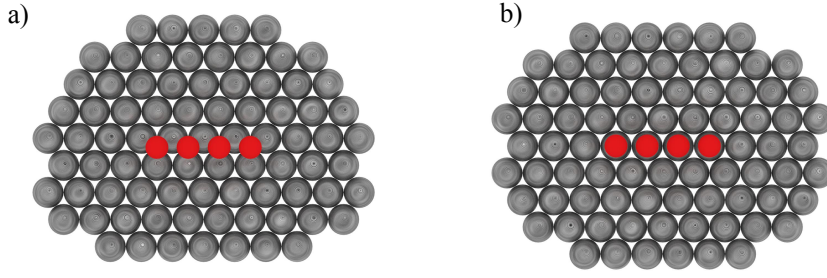


Figure 6.26: The top view of impurity position atop the Fe substrate in the cluster of line configuration for (a) FCC and (b) HCP stacking. The red spheres denote the impurity and the gray ones indicate the Fe atoms.

the Fe adatoms, the two atoms in the middle carry a spin moment of  $3.2 \mu_B$  and the remaining two atoms have a spin moment of  $3.3 \mu_B$ .

For the line configuration, each of the Cr atoms prefer an anti-ferromagnetic coupling between each other. At the same time, they also tend to couple anti-ferromagnetically with respect to the Fe substrate which results in frustration of the Cr spin moments leading to a non-collinear configuration. In the case of the FCC stacking, we found that at the ground state, each Cr moments couple antiferromagnetically to the substrate with only a small deviation from the collinear case being present on their spin moments. The impurity-substrate magnetic exchange interaction in this case strongly competes with the exchange interaction from the impurity-impurity interaction resulting in an stabilization close to the collinear alignment. However in the HCP stacking, the tilting angle is more pronounced than in the FCC stacking. We found that the averaged of the magnitude of the impurity-impurity exchange coupling in the HCP case is 16% higher than the magnitude found in the FCC stacking ( $J = 19.7$  meV). Therefore, the competition between the anti-ferromagnetic impurity-impurity exchange interaction with the impurity-substrate exchange interaction of the Cr impurities in the HCP stacking leading to a deviation of their spin moments.

In comparison to the linear trimer, there is no significant change on the energy profile behavior for the Co and Fe impurities in this line configuration as can be seen comparing Fig. 6.27(a,d) and Fig. 6.27(b,e), respectively. For both stackings, the Co line shows the same repulsive behavior as in the previous systems. A deeper and broader repulsive region at the center of cluster can be seen on its energy profile for both stacking due to the additional number of impurities interacting with the skyrmion. Meanwhile, the Fe line shows an attractive behavior when interacting with the skyrmion in the FCC stacking. In this configuration, there are two energy minima located perpendicular to the line defect in a situation reminiscent of the line trimer case, however, it is almost double than in the trimer case. With a larger number of impurities present atop the substrate, the reduction induced on the Fe-Fe exchange interaction is more pronounced. At the point with the minimum energy in the trimer case, we found that the in-plane magnetization of the Fe impurities gives rise to a lower impurity-substrate exchange energy which yields the lowest energy. However, in the line case, we found a larger reduction on the Fe-Fe exchange

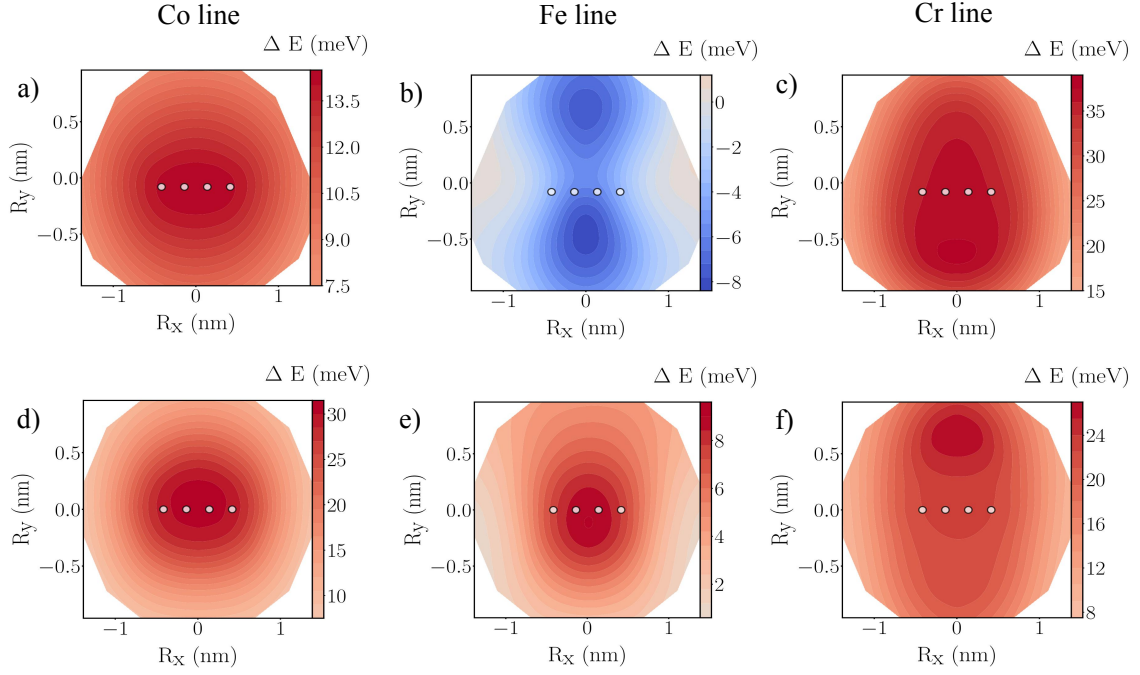


Figure 6.27: The energy profile of skyrmion interacting with impurities in line configuration. The figures at the top and bottom panel present the interaction in the FCC and HCP stacking, respectively. In their interaction with a single magnetic skyrmion, the Co (a, d) and Cr (c, f) impurities in line configuration show the same preference as in the linear trimer case to repel the skyrmion. Meanwhile the Fe impurities also gives a stronger attractive behaviour (b) for the FCC stacking and tend to repel the skyrmion in the HCP satcking (e).

interaction of the Fe atoms around the local minima point. In this case, we found a reduction of  $\sim 1.6$  meV induced by the Fe impurities which is much larger than in the trimer case ( $\sim 0.1$  meV).

Lastly for the Cr case, one can see that due to the small deviation angle on its spin moments, the FCC stacking basically shows the same interaction behavior as the linear trimer case. The presence of four Cr atoms with a large spin moment tends to advance the exchange energy contribution by increasing the collinearity on the Fe-Fe interaction of the atoms in the substrate. In the HCP stacking, the Cr line is also found to repel the skyrmion. However due to a deviation on the spin moments of the impurities, the exchange energy in the HCP stacking is smaller than in the FCC stacking, which then impact on the lower strength of repulsion observed on the energy profile. It shows the same behavior as in the linear trimer case, but the magnitude of repulsion changes.

As can be seen both the nature and geometry of the different impurities is of great importance to determine their interactions with magnetic skyrmions. It is of special importance to pay attention to the sources of magnetic frustration as they can make defects, which were previously repulsive, attractive. However, as seen in the case of the Cr line, one needs to look beyond geometrical considerations, as the changes in the details of the magnetic interactions can make a situation which, *a priori*, seems primed for frustration, instead result in a collinear arrangement.

# Chapter 7

## Conclusions

In this thesis, first principle calculations combined with atomistic spin dynamics simulations have been used to study the skyrmion-defect interaction for FCC Pd/Fe/Ir(111) a material well known for its capacity to host magnetic skyrmions. The investigated defects consist of  $3d$  transition metal atoms (Cr, Fe, and Co), which are placed on top of the Pd layer, for each cluster two different configurations were considered, where the atoms were placed in FCC and HCP sites. The impact of the dimensionality and geometry of the defects was studied by considering several cluster configurations such as an adatom, dimers, trimers, and line defects.

As in previous studies, when an adatom of the studied elements is deposited on the Pd layer a tendency to repel skyrmions is observed. From our analysis, it is found that the observed behavior on the skyrmion-defect interaction is related to the variation of the exchange energy, stemming from the interaction of the impurity with the Fe-substrate and the change on the exchange energy in the substrate due to the influence of the impurity. In general, it is found that these two contributions can considerably change for different clusters and stackings leading to different interactions between the skyrmions and the impurities.

This is most noticeable in the case of the Cr dimer when the composing atoms are nearest neighbors. In this configuration we observed a transition from a repulsive behavior in the adatom case into an attractive one. Such change is a result from the frustration of the exchange interaction among the Cr atoms and the substrate leading to a non-collinear alignment of their spin moments. This competition between the Cr-Cr interaction and the substrate results in the overall exchange interaction being lowered, thus resulting in an attractive interaction. This system also allows us to study another geometrical aspect, namely how the distance between impurities can change the overall interaction profile. It is found that as the distance between the Cr atoms increases leading to a decoupling of the impurities which in turns returns the system to the repulsive behavior obtained for the adatom case.

The influence of the geometry is evidenced once more when one studies the trimer case. Where one can see that both the location of the atoms with respect to each other as well as the type of stacking site can have profound effects on the interaction profile. This is clearly evidenced in the Fe and Cr clusters, where one can observe a remarkably different energy landscape for the FCC and HCP stackings. In the case of Fe the interaction changes from attractive in FCC to repulsive in the HCP configuration. The change is even more dramatic in the Cr case, which in the HCP stacking shows a clear attractive potential, whilst in the FCC stacking a

highly anisotropic profile is found, exhibiting both attractive and repulsive regions. Once more this showcases the importance of the interaction between the impurity electronic states and the ones of the substrate, as clearly evidence by the change in the impurity substrate interaction for each stacking.

By changing the relative positions between the impurities one can also greatly affect the profile. This is evident when one looks at more open trimer configurations, such as the Cr line, where the exchange frustration disappears and the interaction turns repulsive irrespective of the stacking, in contrast with what is observed in the compact trimer cases.

These results showcase that the skyrmion-defect interaction is not merely determined by the chemical nature of the defect, thus paving a new way to generate energy landscapes. Where one could, with a single chemical element, generate pinning and repulsive regions by just changing the geometry of the impurity cluster. This is of special importance, since strong attractive potentials are found for common transition metals such as Cr, thus eliminating the need of more uncommon elements such as Tc to produce this kind of interaction. Another aspect worth highlighting is the role of magnetic frustration in the energy landscape. By considering impurity clusters that by themselves prefer a non-collinear arrangement the tendency towards non-collinearity, and thus magnetic skyrmions, can be greatly enhanced. Thus bringing a new dimension to the realm of systems that can be explored to tailor the properties of magnetic skyrmions.

# Appendix A

## Appendix

### A.1 LLG Equation

In this derivation we will show the proof that one can express the Landau-Lifshitz-Gilbert (LLG) equation in the form of Landau-Liftshitz equation by remorlaizing the gyromagnetic ratio,  $\gamma$ , and the phenomenological damping  $\lambda$ . The expression of LLG equation is given by:

$$\frac{\partial \vec{M}}{\partial t} = -\gamma \vec{M} \times \vec{B}_{\text{eff}} + \frac{\alpha}{M_s} \vec{M} \times \frac{\partial \vec{M}}{\partial t}. \quad (\text{A.1.1})$$

By taking a cross product with  $\vec{M}$  from the left on equation A.1.1, one can have:

$$\begin{aligned} \vec{M} \times \frac{\partial \vec{M}}{\partial t} &= -\gamma \vec{M} \times (\vec{M} \times B_{\text{eff}}) + \frac{\alpha}{M_s} \vec{M} \times (\vec{M} \times \frac{\partial \vec{M}}{\partial t}) \\ &= -\gamma \vec{M} \times (\vec{M} \times B_{\text{eff}}) + \frac{\alpha}{M_s} \left[ \vec{M} \underbrace{(\vec{M} \cdot \frac{\partial \vec{M}}{\partial t})}_0 - \frac{\partial \vec{M}}{\partial t} (\vec{M} \cdot \vec{M}) \right] \\ &= -\gamma \vec{M} \times (\vec{M} \times B_{\text{eff}}) - \alpha M_s \frac{\partial \vec{M}}{\partial t} \end{aligned} \quad (\text{A.1.2})$$

Plug the expression in Eq. A.1.2 into equation Eq. A.1.1, one can have:

$$\begin{aligned} \frac{\partial \vec{M}}{\partial t} &= -\gamma \vec{M} \times B_{\text{eff}} + \frac{\alpha}{M_s} \left[ -\gamma \vec{M} \times (\vec{M} \times B_{\text{eff}}) - \alpha M_s \frac{\partial \vec{M}}{\partial t} \right] \\ \frac{\partial \vec{M}}{\partial t} &= -\gamma \vec{M} \times B_{\text{eff}} - \gamma \frac{\alpha}{M_s} \vec{M} \times (\vec{M} \times B_{\text{eff}}) - \alpha^2 \frac{\partial \vec{M}}{\partial t} \\ (1 + \alpha^2) \frac{\partial \vec{M}}{\partial t} &= -\gamma \vec{M} \times B_{\text{eff}} - \gamma \frac{\alpha}{M_s} \vec{M} \times (\vec{M} \times B_{\text{eff}}) \\ \frac{\partial \vec{M}}{\partial t} &= -\frac{\gamma}{(1 + \alpha^2)} \vec{M} \times B_{\text{eff}} - \frac{\gamma \alpha}{M(1 + \alpha^2)} \vec{M} \times (\vec{M} \times B_{\text{eff}}) \\ \frac{\partial \vec{M}}{\partial t} &= -\gamma_L \vec{M} \times B_{\text{eff}} - \gamma_L \frac{\alpha}{M_s} \vec{M} \times (\vec{M} \times B_{\text{eff}}) \end{aligned} \quad (\text{A.1.3})$$

with  $\gamma_L = \frac{\gamma}{(1 + \alpha^2)}$ .

## A.2 t-matrix

In this section we would like to derive the expression of  $t$ -matrix in terms of the phase-shift. From the discussion in the chapter 3, we have found that the regular solution of the radial Schrödinger equation is given as follows:

$$R_\ell(r; E) = j_\ell(\sqrt{E}r) - i\sqrt{E}h_\ell(\sqrt{E}r)t_\ell(E) \quad (\text{A.2.1})$$

We can derive the expression of this  $t$ -matrix by looking at the characteristic of the wave function at position  $r > r_{max}$ . The exact radial wave function outside the range of potential (at  $r > r_{max}$ ) ( $V_r = 0$ ) can be written in terms of two linearly independent solutions

$$R_\ell(r; E) = P_\ell j_\ell(\sqrt{E}r) + Q_\ell n_\ell(\sqrt{E}r) \quad (\text{A.2.2})$$

For the large  $r$ , the asymptotic behavior of Bessel Functions follow these forms

$$j_\ell(x) \xrightarrow{x \rightarrow \infty} \frac{1}{x} \sin\left(x - \frac{\ell\pi}{2}\right) \quad (\text{A.2.3})$$

$$n_\ell(x) \xrightarrow{x \rightarrow \infty} -\frac{1}{x} \cos\left(x - \frac{\ell\pi}{2}\right) \quad (\text{A.2.4})$$

By introducing these two relations,

$$C_\ell = \sqrt{(P_\ell)^2 + (Q_\ell)^2} \quad (\text{A.2.5})$$

$$\tan \delta(\sqrt{E}) = -\frac{Q_\ell}{P_\ell} \quad (\text{A.2.6})$$

The radial wave function

$$\begin{aligned} R_\ell(r; E) &= \frac{P_\ell}{\sqrt{E}r} \sin\left(\sqrt{E}r - \frac{\ell\pi}{2}\right) - \frac{Q_\ell}{\sqrt{E}r} \cos\left(\sqrt{E}r - \frac{\ell\pi}{2}\right) \\ &= \frac{C_\ell}{\sqrt{E}r} \left[ \sin\left(\sqrt{E}r - \frac{\ell\pi}{2}\right) \cos \delta_\ell(E) + \cos\left(\sqrt{E}r - \frac{\ell\pi}{2}\right) \sin \delta_\ell(E) \right] \\ &= \frac{C_\ell}{\sqrt{E}r} \left[ \sin\left(\sqrt{E}r - \frac{\ell\pi}{2} + \delta_\ell(E)\right) \right] \end{aligned} \quad (\text{A.2.7})$$

where  $\delta_\ell$  is the phase shift of the wave function due to the scattering of the single potential. We can also represent this radial wave function in terms of Bessel function:

$$R_\ell(r; E) = \left[ j_\ell \cos \delta - n_\ell \sin \delta \right] \quad (\text{A.2.8})$$

Using the relation with Hankel function of the first kind, we can also have:

$$\begin{aligned} h_\ell^{(1)} &= j_\ell + in_\ell, \\ R_\ell(r; E) &= \left[ j_\ell + i \exp(i\delta) h_\ell^{(1)} \sin \delta \right] \\ R_\ell(r; E) &= \left[ j_\ell - i k t_\ell h_\ell^{(1)} \right] \end{aligned} \quad (\text{A.2.9})$$

with t-matrix defined as:

$$t_\ell(E) = -\frac{1}{k} e^{i\delta_\ell(E)} \sin \delta_\ell(E) \quad (\text{A.2.10})$$

### A.3 Exchange interaction parameters

This section will briefly derive the expression of the change of energy related to the pairwise exchange interaction constant. To get this change of energy we consider the rotation of two atoms ( $i$  and  $j$ ) by an angle  $\pm\theta/2$ .

$$\delta E_i = -2 \sum_{n \neq i, n \neq j} J_{in} \left[ \cos \left( \frac{\theta}{2} \right) - 1 \right] - 2J_{ij} \left[ \cos \left( \frac{\theta}{2} \right) - 1 \right] \quad (\text{A.3.1})$$

$$\delta E_j = -2 \sum_{m \neq i, m \neq j} J_{jm} \left[ \cos \left( \frac{\theta}{2} \right) - 1 \right] - 2J_{ij} \left[ \cos \left( \frac{\theta}{2} \right) - 1 \right]. \quad (\text{A.3.2})$$

To obtain the pairwise exchange interaction constant,  $J_{ij}$ , between two magnetic moments at site  $i$  and  $j$ , one also needs to subtract the variation of the interaction energy of each atom ( $i$  and  $j$ ) with the environment. Hence, the change of energy related to the  $J_{ij}$  parameters is given by:

$$\begin{aligned} \delta E'_{ij} &= \delta E_{ij} - \delta E_i - \delta E_j \\ &= -2J_{ij} [\cos \theta - 1] - 2J_{ij} \left[ \cos \left( \frac{\theta}{2} \right) - 1 \right] - 2J_{ij} \left[ \cos \left( \frac{\theta}{2} \right) - 1 \right]. \end{aligned} \quad (\text{A.3.3})$$

As one is considering that the rotation angle  $\theta$  is infinitesimally small, one can then expand up to second order to obtain:

$$\begin{aligned} \delta E'_{ij} &\approx J_{ij} \left( \theta^2 - \frac{1}{4}\theta^2 - \frac{1}{4}\theta^2 \right) \\ &\approx \frac{1}{2} J_{ij} \theta^2. \end{aligned} \quad (\text{A.3.4})$$

# Bibliography

- [1] N. S. A. Chandrasekaran, D. Damjanovic and N. Marzari. Defect ordering and defect-domain wall interactions in pbtio3: A first-principles study. *arXiv:1312.4701*, page 9, 2018.
- [2] V. P. Antropov, M. I. Katsnelson, B. N. Harmon, M. van Schilfgaarde, and D. Kusnezov. Spin dynamics in magnets: Equation of motion and finite temperature effects. *Phys. Rev. B*, 54:1019–1035, 1996.
- [3] O. A. AR Mackintosh and M. Springford. *Electrons at the Fermi surface*. Cambridge University Press, Cambridge, 1980.
- [4] M. N. Baibich, J. M. Broto, A. Fert, F. N. V. Dau, F. Petroff, P. Etienne, G. Creuzet, A. Friederich, and J. Chazelas. Giant magnetoresistance of (001)fe/(001)cr magnetic superlattices. *Phys. Rev. Lett.*, 61:2472–2475, 1988.
- [5] D. S. G. Bauer. *Development of a relativistic full-potential first-principles multiple scattering Green function method applied to complex magnetic textures of nano structures at surfaces*. PhD thesis, RWTH Aachen University, 2013.
- [6] J. Beeby. The density of electrons in a perfect or imperfect lattice. *Proc. R. Soc. Lond. A*, 302(1468):113–136, 1967.
- [7] L. Berger. Exchange interaction between ferromagnetic domain wall and electric current in very thin metallic films. *J. Appl. Phys*, 55(6):1954–1956, 1984.
- [8] G. Binasch, P. Grünberg, F. Saurenbach, and W. Zinn. A numerical study of the gas-liquid, two-phase flow maldistribution in the anode of a high pressure pem water electrolysis cell. *Phys. Rev. B*, 39:4828–4830, 1989.
- [9] S. Blügel. Electronic structure of matter: Reduced dimensions. *Lecture Manuscripts of the Spring School of the Institue of Solid State Research*, 38:A5, 2007.
- [10] S. Blügel. Density functional theory in practice. 2008.
- [11] S. Blügel. Non-collinear magnetism in density functional theory. In S. Blügel, Y. Mokrousov, T. Schäpers, and Y. A. (Eds.), editors, *Topological Matter-Topological Inulator, Skyrmions, and Majoranas*, chapter C9, pages C9.1–C9.18. Forschungszentrum Jülich GmbH, Jülich, 2017.
- [12] A. Bogdanov, U. Röbner, and A. Shestakov. Skyrmions in nematic liquid crystals. *Physical Review E*, 67(1):016602, 2003.

- [13] A. N. Bogdanov and D. Yablonskii. Thermodynamically stable “vortices” in magnetically ordered crystals. the mixed state of magnets. *Zh. Eksp. Teor. Fiz.*, 95(1):178, 1989.
- [14] N. Bogdanov. Thermodynamically stable” vortices” in magnetically ordered crystals. the mixed state of magnets. *Zh. Eksp. Teor. Fiz.*, 95:178, 1989.
- [15] S. Bornemann, O. Šipr, S. Mankovsky, S. Polesya, J. Staunton, W. Wurth, H. Ebert, and J. Minár. Trends in the magnetic properties of fe, co, and ni clusters and monolayers on ir (111), pt (111), and au (111). *Physical Review B*, 86(10):104436, 2012.
- [16] H. Brooks. Ferromagnetic anisotropy and the itinerant electron model. *Phys. Rev.*, page 58:909–918, 1940.
- [17] W. F. Brown Jr. Thermal fluctuations of a single-domain particle. *Physical Review*, 130(5):1677, 1963.
- [18] G. Chen. Magnetic skyrmions in thin films. In *Topology in Magnetism*, pages 117–150. Springer, 2018.
- [19] W. K. X. Chen, D. Zhu, S. Li, Y. Huang, Y. Zhang, and W. Zhao. Magnetic skyrmions for future potential memory and logic applications: Alternative information carriers. In *2018 Design, Automation & Test in Europe Conference & Exhibition (DATE)*, pages 119–124. IEEE, 2018.
- [20] H. C. Choi and S.-Z. Lin. Density functional theory study of skyrmion pinning by atomic defects in mnsi. *Phys. Rev. B*, page 93.115112, 2016.
- [21] A. Crépieux and C. Lacroix. Dzyaloshinsky–moriya interactions induced by symmetry breaking at a surface. *Phys. Rev. Lett.*, 82(3):341 – 349, 1998.
- [22] T. B. L. D. Stosic and M. V. Pinning of magnetic skyrmions in a monolayer co film on pt(111): Theoretical characterization and exemplified utilization. *Phys. Rev. B*, pages 96, 214403, 2017.
- [23] S. Doi, M. Ogura, and H. Akai. Development of a first-principles code based on the screened kkr method for large super-cells. In *Journal of Physics: Conference Series*, volume 454, page 012019. IOP Publishing, 2013.
- [24] B. Dupé, M. Hoffmann, C. Paillard, and S. Heinze. Tailoring magnetic skyrmions in ultra-thin transition metal films. *Nature communications*, 5:4030, 2014.
- [25] T. Dupree. Electron scattering in a crystal lattice. *Annals of Physics*, 15(1):63–78, 1961.
- [26] I. Dzyaloshinsky. A thermodynamic theory of “weak” ferromagnetism of antiferromagnetics. *J. Phys. Chem. Solid*, 4(4):241–255, 1958.
- [27] Ebert and S. Mankovsky. Anisotropic exchange coupling in diluted magnetic semiconductors: Ab initio spin-density functional theory. *Phys. Rev.*, 79:045209, 2009.

- [28] H. Ebert, S. Bornemann, J. Braun, D. Ködderitzsch, S. Lowitzer, S. Mankovsky, J. Minár, M. Offenberger, S. Polesya, and V. Popescu. 7 scientific highlight of the month:” recent developments in kkr theory”.
- [29] H. Ebert et al. Magnetism of free and supported clusters: a comparative study. *Central European Journal of Physics*, 7(2):257–263, 2009.
- [30] H. Ebert, D. Koedderitzsch, and J. Minar. Calculating condensed matter properties using the kkr-green’s function method—recent developments and applications. *Reports on Progress in Physics*, 74(9):096501, 2011.
- [31] E. N. Economou. *Green’s functions in quantum physics*, volume 3. Springer, 1983.
- [32] C. H. et al. Pinning and movement of individual nanoscale magnetic skyrmions via defects. *New J. Phys.*, page 18 055009, 2016.
- [33] O. E. et al. *Atomistic Spin Dynamics: Foundations and Applications*. Oxford University Press, 2017.
- [34] T. J. et al. Pinning of magnetic domain walls to structural defects in thin layers within a heisenberg-type model. *Phys. Rev. B*, pages 75, 094422, 2007.
- [35] R. Evans, W. Fan, P. Churemart, T. A. Ostler, M. Ellis, and R. Chantrell. Atomistic spin model simulations of magnetic nanomaterials. *Journal of Physics: Condensed Matter*, 26(10):103202, 2014.
- [36] K. Everschor-Sitte. Emergent electrodynamics in magnetic systems with a focus on magnetic skyrmions. In S. Blügel, Y. Mokrousov, T. Schäpers, and Y. A. (Eds.), editors, *Topological Matter- Topological Insulator, Skyrmions, and Majoranas*, chapter C9, pages C9.1–C9.18. Forschungszentrum Jülich GmbH, Jülich, 2017.
- [37] A. Fert, V. Cros, and J. Sampaio. Skyrmions on the track. *Nat Nano*, page 8(3):152–156, 2013.
- [38] A. Fert and P. M. Levy. Role of anisotropic exchange interactions in determining the properties of spin-glasses. *Phys. Rev. Lett.*, 44:1538–1541, 1980.
- [39] A. Fert, N. Reyren, and V. Cros. Advances in the physics of magnetic skyrmions and perspective for technology. *arXiv preprint arXiv:1712.07236*, 2017.
- [40] J. L. García-Palacios and F. J. Lázaro. Langevin-dynamics study of the dynamical properties of small magnetic particles. *Phys. Rev. B*, 58(22):14937, 1998.
- [41] T. Garel and S. Doniach. Phase transitions with spontaneous modulation-the dipolar ising ferromagnet. *Physical Review B*, 26(1):325, 1982.
- [42] T. Gilbert. A phenomenological theory of damping in ferromagnetic materials. *IEEE Trans. Magn.*, 40(6):3443–3449, 2004.

- [43] O. Gunnarsson, M. Jonson, and B. Lundqvist. Descriptions of exchange and correlation effects in inhomogeneous electron systems. *Physical Review B*, 20(8):3136, 1979.
- [44] S. Heinze, K. Von Bergmann, M. Menzel, J. Brede, A. Kubetzka, R. Wiesendanger, G. Bihlmayer, and S. Blügel. Spontaneous atomic-scale magnetic skyrmion lattice in two dimensions. *Nature Physics*, 7(9):713, 2011.
- [45] P. Hohenberg and W. Kohn. Inhomogeneous electron gas. *Physical review*, 136(3B):B864, 1964.
- [46] M. Hölzer. *Lattice Dynamics from First Principles*. PhD thesis, Martin-Luther-Universität Halle-Wittenberg, 2015.
- [47] A. Hubert and N. Bogdanov. Thermodynamically stable magnetic vortex states in magnetic crystals. *Journal of Magnetism and Magnetic Materials*, 3(138):255–269, 1994.
- [48] J. Iwasaki, M. Mochizuki, and N. Nagaosa. Universal current-velocity relation of skyrmion motion in chiral magnets. *Nat. Commun.*, 4:2442, 2013.
- [49] W. Jiang, X. Zhang, G. Yu, W. Zhang, X. Wang, M. B. Jungfleisch, J. Pearson, X. Cheng, O. Heinonen, and K.L.Wang. Direct observation of the skyrmion hall effect. *Nature Physics*, 13(2):162, 2017.
- [50] R. O. Jones and O. Gunnarsson. The density functional formalism, its applications and prospects. *Reviews of Modern Physics*, 61(3):689, 1989.
- [51] F. Jonietz, S. Mühlbauer, C. Pfleiderer, A. Neubauer, W. Münzer, A. Bauer, T. Adams, R. Georgii, P. Böni, R. A. Duine, et al. Spin transfer torques in mnsi at ultralow current densities. *Science*, 330(6011):1648–1651, 2010.
- [52] V. Joshi. Spintronics: A contemporary review of emerging electronics devices. *Engineering science and technology, an international journal*, 19(3):1503–1513, 2016.
- [53] I. Kézsmárki, S. Bordács, P. Milde, E. Neuber, L. Eng, J. White, H. M. Rønnow, C. Dewhurst, M. Mochizuki, K. Yanai, et al. Néel-type skyrmion lattice with confined orientation in the polar magnetic semiconductor  $\text{GaV}_4\text{S}_8$ . *Nature materials*, 14(11):1116, 2015.
- [54] R. Kikuchi. On the minimum of magnetization reversal time. *J. Appl. Phys*, 27:1352, 1956.
- [55] N. Kiselev, B. Zimmermann, and J. Chico. Atomistic and micromagnetic models of magnetism. In S. Blügel, Y. Mokrousov, T. Schäpers, and Y. A. (Eds.), editors, *Topological Matter- Topological Insulator, Skyrmions, and Majoranas*, chapter C9, pages C9.1–C9.18. Forschungszentrum Jülich GmbH, Jülich, 2017.
- [56] I. Klebanov. Nuclear matter in the skyrmion model. *Nuclear Physics B*, 262(1):133–143, 1985.

- [57] W. Kohn. W. kohn and lj sham, phys. rev. 140, a1133 (1965). *Phys. Rev.*, 140:A1133, 1965.
- [58] W. Kohn and N. Rostoker. Solution of the schrödinger equation in periodic lattices with an application to metallic lithium. *Phys. Rev.*, 94:1111–1120, 1954.
- [59] W. Kohn and L. Sham. Self-consistent equations including exchange and correlation effects. *Physical review*, 140(4A):A1133, 1965.
- [60] J. Korringa. On the calculation of the energy of a bloch wave in a metal. *Physica*, 13:392–400, 1947.
- [61] A. Kovács and R. Dunin-Borkowski. Lorentz microscopy and electron holography of skyrmion. In S. Blügel, Y. Mokrousov, T. Schäpers, and Y. A. (Eds.), editors, *Topological Matter- Topological Insulator, Skyrmions, and Majoranas*, chapter C9, pages C9.1–C9.18. Forschungszentrum Jülich GmbH, Jülich, 2017.
- [62] R. Kubo and N. Hashitsume. Brownian motion of spins. *Progress of Theoretical Physics Supplement*, 46:210–220, 1970.
- [63] L. D. Landau and E. Lifshitz. On the theory of the dispersion of magnetic permeability in ferromagnetic bodies. *Phys. Z. Sowjet.*, 8:153, 1935.
- [64] J. Leliaert, B. V. de Wiele, A. Vansteenkiste, and L. Lau. Influence of material defects on current-driven vortex domain wall mobility. *Phys. Rev. B*, 89:064419, 2014.
- [65] A. Liechtenstein, M. Katsnelson, V. Antropov, and V. Gubanov. Elocal spin density functional approach to the theory of exchange interactions in ferromagnetic metals and alloys. *J. Magn. Magn. Mater*, 67(1):65–74, 1987.
- [66] A. Liechtenstein, M. Katsnelson, and V. Gubanov. Exchange interactions and spin-wave stiffness in ferromagnetic metals. *J. Phys. F: Met. Phys*, 147:L125, 1984.
- [67] I. Lima Fernandes, J. Bouaziz, S. Blügel, and S. Lounis. Universality of defect-skyrmion interaction profiles. *Nature Communications*, 9(1):4395, 2018.
- [68] S. Lin and P. Grundy. ande. a. giess, appi. *Phys. Lett*, 23:485, 1973.
- [69] P. Lloyd and P. Smith. Multiple scattering theory in condensed materials. *Adv. Phys.*, 21(89):69–14, 1972.
- [70] S. Lounis, P. Mavropoulos, P. Dederichs, and S. Blügel. Noncollinear korrington-rostoker green function method: Application to 3d nanostructures on ni (001). *Physical Review B*, 72(22):224437, 2005.
- [71] J. Mallinso. On damped gyromagnetic precession. *IEEE Trans. Magn.*, page 2003, 1987.
- [72] R. M. Martin. *Electronic structure: basic theory and practical methods*. Cambridge university press, 2004.

- [73] P. Mavropoulos and N. Papanikolaou. in computational nanoscience: Do it your-self!, nic series, vol. 31, edited by j. grotendorst, s. blügel, and d. marx (john von neumann institute for computing, jülich, 2006). *Chem. Inform.*, 131-158:392 – 400, 2006.
- [74] C. Moreau-Luchaire, C. Moutafis, N. Reyren, J. Sampaio, N. Van Horne, C. Vaz, K. Bouzehouane, K. Garcia, C. Deranlot, P. Warnicke, et al. Skyrmions at room temperature: From magnetic thin films to magnetic multilayers. *arXiv preprint arXiv:1502.07853*, 2015.
- [75] T. Moriya. Anisotropic superexchange interaction and weak ferromagnetism. *Phys. Rev.*, 120:91, 1960.
- [76] S. Mühlbauer, B. Binz, F. Jonietz, C. Pfleiderer, A. Rosch, A. Neubauer, R. Georgii, and P. Böni. Skyrmion lattice in a chiral magnet. *Science*, 323(5916):915–919, 2009.
- [77] N. Nagaosa and Y. Tokura. Topological properties and dynamics of magnetic skyrmions. *Nat. Nanotechnol.*, 8:899–911, 2013.
- [78] B. Nonas, K. Wildberger, R. Zeller, and P. Dederichs. Energetics of 3 d impurities on the (001) surface of iron. *Physical review letters*, 80(20):4574, 1998.
- [79] N. Papanikolaou, R. Zeller, and P. Dederichs. Conceptual improvements of the kkr method. *Journal of Physics: Condensed Matter*, 14(11):2799, 2002.
- [80] S. S. Parkin, M. Hayashi, and L. Thomas. Magnetic domain-wall racetrack memory. *Eur. Phys. J. B*, 320:190–194, 2008.
- [81] S. Polesya, S. Mankovsky, O. Sipr, W. Meindl, C. Strunk, and H. Ebert. Finite-temperature magnetism of fe x pd 1- x and co x pt 1- x alloys. *Physical Review B*, 82(21):214409, 2010.
- [82] N. Romming, C. Hanneken, M. Menzel, J. E. Bickel, B. Wolter, K. von Bergmann, A. Kubetzka, and R. Wiesendanger. Writing and deleting single magnetic skyrmions. *Science*, 341(6146):636–639, 2013.
- [83] A. Rosch. Skyrmions: moving with the current. *Nature nanotechnology*, 8(3):160, 2013.
- [84] U. K. Röbller, A. A. Leonov, and A. N. Bogdanov. Chiral skyrmionic matter in non-centrosymmetric magnets. In *Journal of Physics: Conference Series*, volume 303, page 012105. IOP Publishing, 2011.
- [85] K. Schwarz. Dft calculations of solids with lapw and wien2k. *Journal of Solid State Chemistry*, 176(2):319–328, 2003.
- [86] B. Schweflinghaus. *First-principles investigation of inelastic magnetic excitations in nanostructures deposited on surfaces*. PhD thesis, RWTH Aachen University, 2015.
- [87] S. Seki and M. Mochizuki. *Skyrmions in magnetic materials*. Springer, 2016.

- [88] S. Seki, X. Yu, S. Ishiwata, and Y. Tokura. Observation of skyrmions in a multiferroic material. *Science*, 336(6078):198–201, 2012.
- [89] E. Simon, K. Palotás, L. Rózsa, L. Udvardi, and L. Szunyogh. Formation of magnetic skyrmions with tunable properties in pde bilayer deposited on ir (111). *Physical Review B*, 90(9):094410, 2014.
- [90] B. Skubic, J. Hellsvik, L. Nordström, and O. Eriksson. A method for atomistic spin dynamics simulations: implementation and examples. *Journal of physics: condensed matter*, 20(31):315203, 2008.
- [91] T. Skyrme. A unified field theory of mesons and baryons. *Nuclear Phys.*, 31:556–569, 1962.
- [92] J. C. Slonczewski. Current-driven excitation of magnetic multilayers. *Journal of Magnetism and Magnetic Materials*, 159(1-2):L1–L7, 1996.
- [93] S.Lounis. Theory of magnetic transition metal nanoclusters on surfaces. *Chem. Inform.*, 40:392 – 400, 2009.
- [94] S. Sondhi, A. Karlhede, S. Kivelson, and E. Rezayi. Skyrmions and the crossover from the integer to fractional quantum hall effect at small zeeman energies. *Physical Review B*, 47(24):16419, 1993.
- [95] M. Stone. Magnus force on skyrmions in ferromagnets and quantum hall systems. *Physical Review B*, 53(24):16573, 1996.
- [96] L. Udvardi, L. Szunyogh, K. Palotás, and P. Weinberger. First-principles relativistic study of spin waves in thin magnetic films. *Phys. Rev. B*, 68:104436, 2003.
- [97] U. von Barth and L. Hedin. A local exchange-correlation potential for the spin polarized case. i. *Journal of Physics C: Solid State Physics*, 5(13):1629, 1972.
- [98] S. A. Wolf, D. D. Awschalom, R. A. Buhrman, J. M. Daughton, S. von Molnár, M. L. Roukes, A. Y. Chtchelkanova, and D. M. Treger. Universal current-velocity relation of skyrmion motion in chiral magnets. *Science*, 294:1488–95, 2001.
- [99] D. Wortmann. *An embedding green function approach for electron transport through interfaces*. PhD thesis, Bibliothek der RWTH Aachen, 2003.
- [100] X. Yu, N. Kanazawa, Y. Onose, K. Kimoto, W. Zhang, S. Ishiwata, Y. Matsui, and Y. Tokura. Near room-temperature formation of a skyrmion crystal in thin-films of the helimagnet fege. *Nature materials*, 10(2):106, 2011.
- [101] X. Yu, N. Kanazawa, W. Zhang, T. Nagai, K. K. T. Hara, Y. Matsui, Y. Onose, and Y. Tokura. Skyrmion flow near room temperature in an ultralow current density. *Nat. Commun.*, page 3(988), 2012.
- [102] J. Zabloudil. *The full-potential screened KKR method*. PhD thesis, TU Wien, 2000.

- [103] J. Zabloudil, R. Hammerling, L. Szunyogh, and P. Weinberger. *Electron Scattering in Solid Matter: a theoretical and computational treatise*, volume 147. Springer Science & Business Media, 2006.
- [104] J. Zang, M. Mostovoy, J. H. Han, and N. Nagaosa. Dynamics of skyrmion crystals in metallic thin films. *Physical review letters*, 107(13):136804, 2011.
- [105] R. Zeller. Multiple-scattering solution of schrodinger's equation for potentials of general shape. *J.Phys. C: Solid State Physics*, 20(16):2347–2360, 1987.
- [106] X. Zhang, Y. Zhou, and M. Ezawa. Magnetic bilayer-skyrmions without skyrmion hall effect. *Nature communications*, 7:10293, 2016.
- [107] B. Zimmermann. *Calculation of the Dzyaloshinskii-Moriya Interaction in ultrathin magnetic Films: Cr/W (110)*. PhD thesis, Master's thesis, RWTH Aachen, 2010.